NTNU – Trondheim
Norwegian University of
Science and Technology

Numerical Study of Seabed Boundary Layer Flow around Monopile and Gravity-based Wind Turbine Foundations

Eirik Trygsland

Marine Technology
Submission date: June 2015
Supervisor: Dag Myrhaug, IMT
Co-supervisor: Muk Chen Ong, MARINTEK

Norwegian University of Science and Technology
Department of Marine Technology

NTNU Trondheim
Norwegian University of Science and Technology
Department of Marine Technology – Group of Marine Structures

MASTER THESIS IN MARINE TECHNOLOGY

SPRING 2015

FOR

STUD. TECHN. EIRIK TRYGSLAND

NUMERICAL STUDY OF SEABED BOUNDARY LAYER FLOW AROUND MONOPILE AND GRAVITY-BASED WIND TURBINE FOUNDATIONS

Wind turbine foundations (e.g. monopile and gravity-based foundations) on the seabed are often subject to high Reynolds number seabed boundary layer flows ($Re > 10^6$). These high Reynolds number flow conditions are hard and expensive to achieve in an experimental setup, which requires appropriate experimental facilities, minimizing human and instrument errors during measuring hydrodynamic quantities etc. Therefore an attractive alternative is to use Computational Fluid Dynamics (CFD) to provide the essential hydrodynamic coefficients for engineering design. Turbulence modelling will be employed in this study. Predictions of hydrodynamic quantities and flow pattern around the structures will be compared with published experimental data and numerical results. The effects of different foundation geometries in destroying the formation of horseshoe vortices (which is the main cause of scour problems) will be investigated and discussed.

The student shall:

1. Give a background of CFD and flow around bluff bodies
2. Describe the computational tools
3. Give a background description of turbulence modelling
4. Perform numerical simulations to study the seabed boundary layer flow around monopile and gravity-based wind turbine foundations
5. Present and discuss the results

The work scope may prove to be larger than initially anticipated. Subject to approval from the supervisor, topics may be deleted from the list above or reduced in extent.

In the thesis the candidate shall present his personal contribution to the resolution of problem within the scope of the thesis work.

Theories and conclusions should be based on mathematical derivations and/or logic reasoning identifying the various steps in the deduction.

The candidate should utilize the existing possibilities for obtaining relevant literature.

The thesis should be organized in a rational manner to give a clear exposition of results, assessments, and conclusions. The text should be brief and to the point, with a clear language. Telegraphic language should be avoided.

The thesis shall contain the following elements: A text defining the scope, preface, list of contents, summary, main body of thesis, conclusions with recommendations for further work, list of symbols and acronyms, reference and (optional) appendices. All figures, tables and equations shall be numerated.

The supervisor may require that the candidate, in an early stage of the work, present a written plan for the completion of the work. The plan should include a budget for the use of computer and laboratory resources that will be charged to the department. Overruns shall be reported to the supervisor.

The original contribution of the candidate and material taken from other sources shall be clearly defined. Work from other sources shall be properly referenced using an acknowledged referencing system.

The thesis shall be submitted in three copies:

- Signed by the candidate
- The text defining the scope included
- In bound volume(s)
- Drawings and/or computer prints which cannot be bound should be organized in a separate folder.

Advisors: Dr. Muk Chen Ong, Marintek
Professor Dag Myrhaug

Deadline: 10.06.2015

Dag Myrhaug
Supervisor

Preface

This thesis completes my master's degree in Marine Technology at the Norwegian University of Science and Technology (NTNU). I want to thank my supervisors Prof. Dag Myrhaug and Dr. Muk Chen Ong for their help with my work. Especially Dr. Ong has provided a lot of guidance and help throughout the semester. I also want to thank T. S. Sim and Mia Abrahamsen Prsic for insightful discussions on the topic of computational fluid dynamics.

This work has been supported by NOWITECH (Norwegian Research Centre for Offshore Wind Technology) which is co-funded by the Research Council of Norway, industrial companies and participating research organizations (http://www.nowitech.no).

A last thanks goes to my friends in office A1.007.

Trondheim, June 10, 2015

Eirik Trygsland

.....

Eirik Trygsland

Abstract

Computational fluid dynamics (CFD) has been used to study the boundary layer flow around three different bottom-fixed offshore wind turbine foundation designs. Two of the designs are gravity-based foundations, where one has a hexagonal bottom slab and one a circular bottom slab (bottom part). The third design is a monopile. Three-dimensional analyses have been performed with Spalart-Allmaras Delayed Detached Eddy Simulation using a Reynolds number 4×10^6 based on the free stream velocity and the diameter of the monopile, D. The boundary layer size is D in all the analyses. Time averaged results for velocities, pressure and bed shear stress were obtained. The dependence of the results on the mesh resolution was investigated and comparisons with published data were made. The results were found to be reasonably accurate.

A distinct horseshoe vortex was found in front (upstream side) of the monopile foundation. Vortex shedding was present in the wake of all the foundations. Two smaller horseshoe vorticies were found in front of the hexagonal gravity-based foundation, were one was on the top of the bottom slab and one was near the seabed in front of the bottom slab. Three horseshoe vortices in total were found in front of the circular gravity-based foundation, due to the presence of two horseshoe vortices near the seabed in front of the bottom slab.

A large region of downflow exists in front of the monopile, reaching all the way down to the seabed. This causes a backflow in front of the foundation near the seabed due to conservation of mass. The gravity-based foundations were found to have two main regions of downflow, one in front of the cylindrical shaft (upper part) on top of the bottom slab and a smaller region in front of the bottom slab near the seabed. The gravity-based designs are found to limit the downflow near the seabed.

Pressure distributions around the foundations were studied. A positive vertical pressure gradient was found in front of the monopile foundation. It was also found in front of the cylindrical shaft and in front of the bottom slab near the seabed on the gravity-based foundations. A larger volume of increased pressure exists in front of the monopile foundation than in front of the gravity-based foundations due to its geometry.

The bed shear stress in the flow direction along the upstream symmetryline on the seabed was investigated. The horseshoe vortex size, measured as the distance from the separation point to the foundation surface along this line, was found to be $0.40D$ for the monopile foundation, $0.125D$ for the hexagonal and $0.22D$ for the circular gravity-based foundation. Bed shear stress distributions near the foundations were obtained. The magnitude of the bed shear stress, normalized by the far field bed shear stress, was used. A maximum value of 4.89 was found near the surface of the monopile foundation at $\phi = \pm 66.5$ degrees, where ϕ is the angle measured from the stagnation point in front of the foundation. Similarly, 2.86 at $\phi = \pm 60.1$ was found for the hexagonal gravity-based foundation. The larger values of the hexagonal foundation are concentrated around the corners at $\phi = \pm 60$ degrees, and the rest of the seabed has shear stresses close to the far field shear stress. The results of the circular foundations were found to be slightly asymmetric, with a maximum value of 2.59 at $\phi = 68.9$ degrees for the upper distribution (for positive ϕ) and 2.72 at $\phi = -85.4$ degrees for the lower (for negative ϕ).

Sammendrag

"Computational Fluid Dynamics" (CFD) har blitt brukt til å studere grensesjiktstrømningen rundt tre forskjellige design for bunnfaste fundamenter for vindturbiner til havs. To av designene er gravitasjonsfundamenter, hvor et har en sekskantet bunndel og et en sirkulær bunndel. Det tredje designet er en "monopile", en vertikal, sirkulær sylinder. Tredimensjonale analyser har blitt utført med "Spalart-Allmaras Delayed Detached Eddy Simulation" med et Reynolds tall 4×10^6 basert på fristrømningshastigheten og diameteren på den sirkulære sylinderen, D. Grensesjiktstykkelsen er D i alle analysene. Tidsgjennomsnitt for hastigheter, trykk og skjærspenninger på havbunnen ble beregnet. Konvergensstudier med hensyn på mesh og sammenligninger av resultat med publiserte data ble gjennomført. Nøyaktigheten til resultatene ble funnet til å være rimelig.

En tydelig hesteskovirvel ble funnet på fremsiden (oppstrømssiden) av monopile-fundamentet. Virvelavløsning fant sted på baksiden av alle fundamentene. To mindre hesteskovirvler ble funnet på fremsiden av det heksagonale gravitasjonsfundamentet, en på toppen av bunndelen og en nære havbunnen foran bunndelen. Tre hesteskovirvler totalt ble funnet foran det sirkulære gravitasjonsfundamentet, hvorav to var nær havbunnen foran bunndelen.

Et stort område av nedstrømning som når helt ned til havbunnen eksisterer foran monopile-fundamentet. Dette fører til en tilbakestrømning foran fundamentet nær havbunnen på grunn av massebevaringsprinsippet. To hovedregioner med nedstrømning ble funnet på forsiden av gravitasjonsfundamentene, en foran den øvre delen (sylinderformet del) på toppen av bunndelen og et mindre område foran bunndelen nær havbunnen. Gravitasjonsfundamentene er funnet til å begrense nedstrømning nær havbunnen.

Trykkfordelinger rundt fundamentene ble studert. En positiv vertikal trykkgradient ble funnet foran monopile-fundamentet. Det samme ble funnet på forsiden av den øvre delen og bunndelen nær havbunnen på gravitasjonsfundamentene. Et større volum av økt trykk eksisterer foran monopile-fundamentet enn foran gravitasjonsfundamentene på grunn av dets geometri.

Skjærspenninger på bunnen i strømningsretningen langs symmetrilinjen oppstrøms ble undersøkt. Størrelsen på hesteskovirvlene, målt som avstanden fra separasjonspunktet til fundamentoverflaten langs denne linjen, ble funnet å være $0.40D$ for monopile-fundamentet, $0.125D$ for det sekskantede og $0.22D$ for det sirkulære gravitasjonsfundamentet. Skjærspenningsfordelinger på bunnen i nærheten fundamentene ble funnet. Størrelsen på skjærspenningene på bunnen (ikke retnings-komponenter), normalisert med uforstyrret skjærspenning langt fra fundamentet, ble brukt. En maksverdi 4.89 ble funnet i nærheten av overflaten til monopile-fundamentet ved $\phi = \pm$ 66.5 grader, hvor ϕ er vinkelen målt fra stagnasjonspunkt foran fundamentet. Tilsvarende verdier på 2.86 ved $\phi = \pm$ 60.1 ble funnet for det heksagonale gravitasjonsfundamentet. De større verdiene for det heksagonale gravitasjonsfundamentet er konsentrert rundt hjørnene ved $\phi = \pm$ 60 grader, mens resten av verdiene er nære fristrømsskjærspenningen. Resultatene for det sirkulære gravitasjonsfundamentet var noe usymmetriske. Maksverdien på oversiden (for positive ϕ) ble funnet til å være 2.59 ved $\phi = 68.9$ grader og makverdien på undersiden 2.72 ved $\phi = -85.4$ grader (for negative ϕ).

Contents

Contents vi

List of Figures viii

List of Tables x

Abbreviations xi

Symbols xii

1 Introduction 1
- 1.1 Motivation . . . 1
  - 1.1.1 Offshore wind . . . 1
  - 1.1.2 Flow around offshore wind turbine foundations . . . 2
- 1.2 Foundations for offshore wind . . . 2
  - 1.2.1 Monopile foundations . . . 3
  - 1.2.2 Gravity-based foundations . . . 4
- 1.3 Previous work . . . 5
- 1.4 Outline . . . 6

2 Theory 8
- 2.1 Basic hydrodynamics . . . 8
  - 2.1.1 Reynolds number . . . 8
  - 2.1.2 Boundary layer . . . 9
  - 2.1.3 Separation and vortex shedding . . . 10
  - 2.1.4 Strouhal number . . . 11
  - 2.1.5 Force coefficients . . . 12
  - 2.1.6 Pressure coefficient . . . 13
- 2.2 Horseshoe vortex system . . . 14
- 2.3 Scour . . . 14

3 Computational fluid dynamics 16
- 3.1 OpenFOAM . . . 16
  - 3.1.1 Meshing and pre-processing . . . 17
  - 3.1.2 Solving . . . 17
  - 3.1.3 Post-processing . . . 18
- 3.2 Navier-Stokes equations . . . 18
- 3.3 Turbulence modeling . . . 18
  - 3.3.1 Turbulence . . . 18
  - 3.3.2 Direct Numerical Simulation (DNS) . . . 19
  - 3.3.3 Large Eddy Simulation (LES) . . . 20
  - 3.3.4 Reynolds-Averaged Navier Stokes (RANS) . . . 20
  - 3.3.5 Detached Eddy Simulation (DES) . . . 21

3.4 Spalart-Allmaras Delayed Detached Eddy Simulation (SADDES) 21
3.4.1 Spalart-Allmaras turbulence model 21
3.4.2 DDES 23
3.5 Turbulent velocity profiles and wallfunctions 24

4 Computational model 26
4.1 Geometry 26
4.1.1 Lillgrund wind farm 26
4.1.2 Geometry in the analyses 27
4.2 Conditions 30
4.2.1 Reynolds number 30
4.2.2 Boundary layer 30
4.2.3 Boundary conditions 31
4.3 Computational mesh 34
4.4 OpenFOAM and High Performance Computing setup 36
4.5 Effects not included in the model 36

5 Results and discussion 37
5.1 Convergence and quality of results 37
5.2 Vorticity 45
5.2.1 Vortical structures, Q-criterion 45
5.2.2 Vorticity strength and components 48
5.3 Velocities 50
5.3.1 Downflow and backflow 50
5.3.2 Velocity profiles 51
5.4 Pressure 54
5.4.1 Isolines and isosurfaces 54
5.4.2 Comparisons with published data 57
5.5 Bed shear stress 59
5.5.1 Normalization and time variation 59
5.5.2 Results and comparisons with published data 61

6 Conclusion 70
6.1 Further work 72

Bibliography 75

A OpenFOAM case files 76
A.1 0-folder 76
A.2 system-folder 84

B MATLAB Codes 90

List of Figures

1.1 Levelized electricy costs . . . 2
1.2 Monopile foundation . . . 4
1.3 Gravity based foundation . . . 5

2.1 Flow regimes . . . 9
2.2 Scetch of a boundary layer . . . 10
2.3 Separation . . . 10
2.4 Vortex shedding . . . 11
2.5 Cross flow and drag forces . . . 11
2.6 Strouhal number . . . 12
2.7 Horseshoe vortex system . . . 14
2.8 Sketch of a scour hole around a vertical pile . . . 15

3.1 Velocity measurements in a turbulent jet . . . 19
3.2 Comparison of CFD methods . . . 21
3.3 Sublayers in a turbulent boundary layer . . . 25

4.1 Section of the Lillgrund wind farm foundation . . . 27
4.2 Bottom slab of the Lillgrund wind farm foundation . . . 27
4.3 Geometry of the hexagonal GBF . . . 28
4.4 Geometry of the circular GBF . . . 29
4.5 Geometry of the monopile foundation . . . 29
4.6 3D view of the foundation geometries . . . 30
4.7 Computational domain. Sketch by the author. . . . 31
4.8 Blocks in the computational mesh . . . 34
4.9 Mesh shown in the symmetry plane . . . 35
4.10 Computational mesh for the monopile foundation . . . 35
4.11 Close up of the mesh on the surface of the foundations . . . 35

5.1 Time series of drag force and cross flow force coefficients . . . 38
5.2 Courant number distribution . . . 39
5.3 Convergence plot, monopile . . . 39
5.4 Normalized power density spectrum, monopile . . . 40
5.5 Time series of the drag force coefficient for the Monopile2 analysis . . . 41
5.6 Convergence plot, hexagonal GBF . . . 42
5.7 Normalized power density spectrum, hexagonal GBF . . . 42
5.8 Convergence plot, circular GBF . . . 43
5.9 Time-averaged pressure coefficient in the xy plane for the monopile foundation . 44
5.10 Time-averaged pressure coefficient in the xy plane for the hexagonal GBF . . . 44
5.11 Time-averaged pressure coefficient in the xy plane for the circular GBF . . . 44
5.12 Normalized power density spectrum, circular GBF . . . 45
5.13 3D view of instantaneous vortical structures around the monopile foundation . . 46
5.14 2D view of instantaneous vortical structures around the monopile foundation . . 46

5.15 3D view of instantaneous vortical structures around the hexagonal GBF 47
5.16 2D view of instantaneous vortical structures around the hexagonal GBF 47
5.17 3D view of instantaneous vortical structures around the circular GBF 48
5.18 2D view of instantaneous vortical structures around the circular GBF 48
5.19 X-component of vorticity at $z/D = 0.025$ 49
5.20 Y-component of vorticity at $z/D = 0.025$ 49
5.21 Z-component of vorticity at $z/D = 0.025$ 49
5.22 Vertical velocity w in the y = 0 plane 50
5.23 Horizontal velocity u in the y = 0 plane 51
5.24 Profiles of velocity in the x-direction for the monopile foundation 52
5.25 Profiles of velocity in the x-direction for the hexagonal GBF 53
5.26 Profiles of velocity in the x-direction for the circular GBF 53
5.27 Pressure coefficient isolines in the xz plane at $y/D = 0$ for the hexagonal GBF . 54
5.28 Pressure coefficient isolines in the xz plane at $y/D = 0$ for the circular GBF . . . 55
5.29 Pressure coefficient isolines in the xz plane at $y/D = 0$ for the monopile foundation 55
5.30 Pressure coefficient isosurfaces for the hexagonal GBF 56
5.31 Pressure coefficient isosurfaces for the circular GBF 56
5.32 Pressure coefficient isosurfaces for the monopile foundation 57
5.33 Normalized pressure coefficient along $y/D = 0, z/D = 0$ 58
5.34 Normalized pressure coefficient along $x/D = -0.5, y/D = 0$ 58
5.35 Bed shear stresses along the line $y/D = 9$, $z/D = 0$ 59
5.36 Bed shear stresses along the symmetryline, y = 0, z = 0 60
5.37 Instantaneous time frames of the shear stress coefficient 61
5.38 Bed shear stress amplification factor along $y/D = 0$, $z/D = 0$ (Roulund et al., 2005) 62
5.39 Influence of the Reynolds number on separation distance (Roulund et al., 2005) . 63
5.40 Influence of the Reynolds number on maximum shear stress amplification (Roulund et al., 2005) 63
5.41 Shear stress amplification along the symmetryline, monopile foundation 64
5.42 Shear stress amplification along the symmetryline, hexagonal GBF 64
5.43 Shear stress amplification along the symmetryline, circular GBF 65
5.44 Bed shear stress distribution at Re = 200 (Roulund et al., 2005) 66
5.45 Bed shear stress distribution at Re = 2000 (Roulund et al., 2005) 66
5.46 Bed shear stress distribution at Re = 20000 (Roulund et al., 2005) 66
5.47 Bed shear stress distribution at Re = 200000 (Roulund et al., 2005) 67
5.48 Bed shear stress amplification, monopile, present study 67
5.49 Bed shear stress amplification, hexagonal GBF, present study 68
5.50 Bed shear stress amplification, circular GBF, present study 68
5.51 Shear stress distributions on the seabed and the foundation surfaces, present study 69

List of Tables

1.1 Distribution of foundation types 3

5.1 Mesh convergence study, monopile foundation 40
5.2 Mesh convergence study, hexagonal GBF 42
5.3 Mesh convergence study, circular GBF 43
5.4 Comparison of shear stress amplification, separation distance and horseshoe vortex size between the different foundations 65

Abbreviations

2D	Two-dimensional
3D	Three-dimensional
CFD	**C**omputational **F**luid **D**ynamics
DDES	**D**elayed **D**etached **E**ddy **S**imulation
DES	**D**etached **E**ddy **S**imulation
DNS	**D**irect **N**umerical **S**imulation
GBF	**G**ravity-**B**ased **F**oundation
HSV	**H**orse**S**hoe **V**ortex
LES	**L**arge **E**ddy **S**imulation
RANS	**R**eynolds-**A**veraged **N**avier-**S**tokes
RMS	**R**oot **M**ean **S**quare
SADDES	**S**palart-**A**llmaras **D**elayed **D**etached **E**ddy **S**imulation

Symbols

α	Shear stress amplification factor
δ	Boundary layer size
δ_{ij}	Kronecker delta
ϵ	Rate of viscous dissipation
κ	von Karmans constant
μ	Dynamic viscosity of fluid
μ_t	Turbulent dynamic viscosity of fluid
ν	Kinematic viscosity of fluid
ν_t	Turbulent voscosity
$\tilde{\nu}$	Working variable in the Spalart-Allmaras turbulence model
ρ	Fluid density
τ	Shear stress
ϕ	Angle measured from stagnation point
A_{proj}	Projected area
CFL	Courant number
C_p	Pressure coefficient
C_τ	Shear stress coefficient
C_x	Drag force coefficient
$\overline{C_x}$	Mean drag force coefficient
C_y	Cross flow force coefficient coefficient
$\overline{C_y}$	Mean cross flow force coefficient
$C_{y,rms}$	Root mean square of cross flow force coefficient
D	Size parameter
E	Log law constant
F_n	Froude number
F_x	Force in the x direction
F_y	Force in the y direction
f_v	Vortex shedding frequency
h_p	Normal distance between the wall and the first node away from the wall

k	Turbulent kinetic energy
k_s	Nikuradse's equivalent sand roughness
p	Pressure
p_∞	Initial pressure
q_b	Rate of sediment transport by bed load
Re	Reynolds number
St	Strouhal number
u^+	Dimensionless velocity
u_τ	Friction velocity
U	Fluid velocity
U_∞	Inflow velocity
u	Velocity in the x direction
v	Velocity in the y direction
w	Velocity in the z direction
y^+	Dimensionless distance from the wall
z_w	Wall roughness

Chapter 1

Introduction

1.1 Motivation

1.1.1 Offshore wind

Wind power is a significant source of energy in the world today, with a total capacity of 370 GW installed globally at the end of 2014 (Global Wind Energy Council, 2015). This is predominantly onshore, but recent years have seen considerable efforts in offshore wind power, so far mainly in Europe. 8 GW, 2.2 % of the global capacity, is now installed in European waters and about 18 % of this was installed in 2014 alone (European Wind Energy Association, 2015a). Wind power now accounts for 10.2 % of the electricity consumption in the European Union (European Wind Energy Association, 2015b), and is likely to play an important role in the European Union's 2030 framework for climate and energy policies which was agreed on in October 2014. It states that greenhouse gas emissions shall be reduced by 40 % compared to 1990 levels, at least 27 % of the power consumption shall be from renewable energy sources and that the energy efficiency shall be increased with at least 27 % by 2030 in the European Union (European Commission, 2015).

Offshore wind is a promising energy source for two main reasons, the stronger winds at sea and the fact that most people live near the coast. Yet, offshore wind power has so far been very expensive due to costs of installation, maintenance and infrastructure. Figure 1.1 shows the ranges of levelized energy costs (i.e. installation costs included) for several energy sources in Germany in 2013. Onshore wind, ranging from 0.045 €/kWh to 0.107 €/kWh, are in some cases competitive to coal power. Offshore wind, at 0.119 €/kWh to 0.194 €/kWh, is in no case competitive to coal and is in all cases more expensive than onshore wind. It is for the moment

dependent on subsidies.

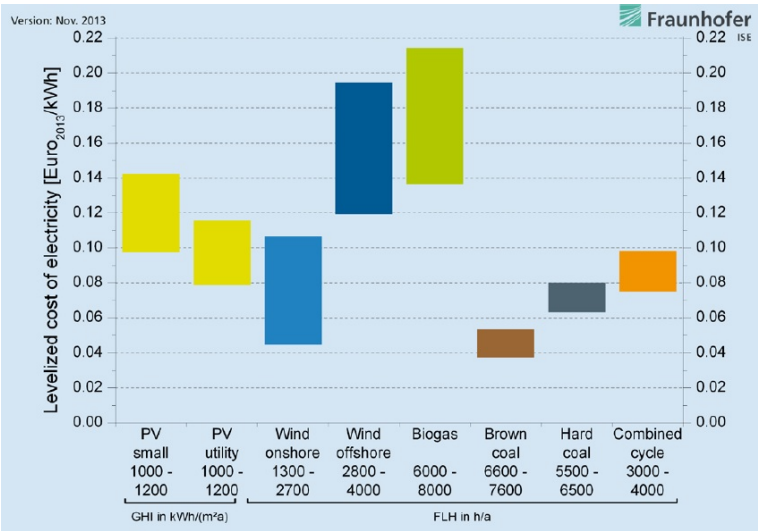

FIGURE 1.1: Levelized electricy costs in Germany in 2013 (PV = Photovoltaic) (Fraunhofer Institut for Solar Energy Systems ISE, 2013)

1.1.2 Flow around offshore wind turbine foundations

Most offshore wind turbines today are supported by a bottom-fixed foundation. A problem with these foundations is scour, local erosion of the seabed that occurs because of the flows around the foundations near the bottom due to currents or waves. This can weaken the stability of the structure needed to withstand the large overturning moment created by the wind on the turbine. Up to €150 000 per turbine, 6 % to 10 % of the total average project cost, can be spent on scour protection (DHI Group, 2012). This is done by seabed preparation and by covering the seabed near the foundation with rocks. The scour problem also causes a need for monitoring and sometimes repairs. An increased understanding of these flows could improve the design of wind turbine foundations with respect to scour and decrease the need for scour protection, monitoring and repairs, and thereby diminish one of the sources of costs for offshore wind power.

1.2 Foundations for offshore wind

There are 5 main types of bottom-fixed foundations used for offshore wind turbines, namely monopile, gravity based, jacket, tripod and tripile foundations. Table 1.1 shows the distribution of foundation types for the 2488 offshore wind turbines installed in European waters as of January 2015 (European Wind Energy Association, 2015a). The monopile foundation is the far most common type followed by gravity-based foundations.

Table 1.1: Distribution of foundation types in installed European offshore wind turbines as of January 2015 (European Wind Energy Association, 2015a)

Type	Percentage
Monopile	78.8
Gravity based foundation	10.4
Jacket	4.7
Tripod	4.1
Tripile	1.9

Section 1.2.1 and 1.2.2 give a brief introduction of monopile and gravity-based foundations (based on Offshore Energy Structures (Karimirad, 2014, Chapter 3)).

1.2.1 Monopile foundations

Monopiles are simple to design, produce and install. They are also well-known in the offshore industry where they are used on jacket platforms. Made from steel and concrete, they are driven into the seabed to give stability to the structure. A typical monopile foundation for offshore wind is 3 - 6 meters in diameter, and half the length is in the ground. Monopiles are problematic for water depths over 30 meters or so, because an increase in depth quickly increases the necessary diameter. The largest offshore wind farm in the world today measured in both number of turbines (175) and capacity (630 MW) is London Array 1, which uses monopile foundations for all its turbines (Lorc, Knowledge, 2011). Figure 1.2 shows an illustration of a typical monopile. The foundation, or pile, is shown in grey. The terms monopile, circular pile and circular cylinder will be used synonymously throughout the text.

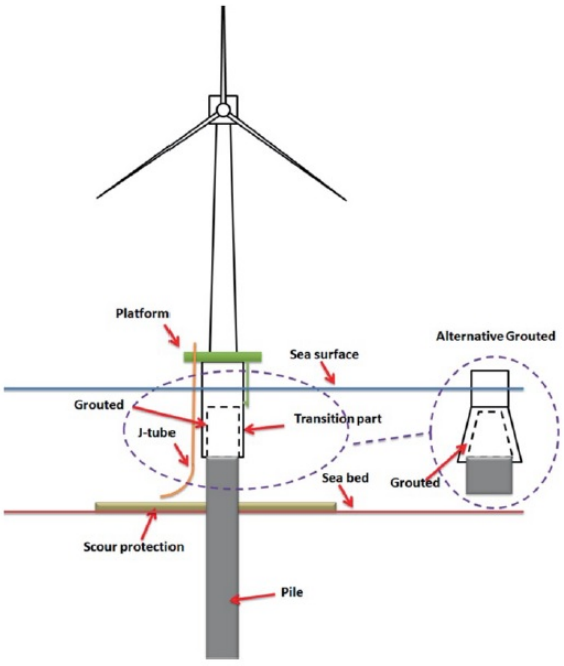

FIGURE 1.2: Monopile foundation (Karimirad, 2014)

1.2.2 Gravity-based foundations

Gravity-based foundations consist of a bottom part, called a bottom slab, with a vertical circular cylinder, called a cylindrical shaft, on top of it. Some form of ice protection in the region near the water surface is sometimes used (not in the illustration in Figure 1.3). The foundations are made from concrete and will typically float when they are not ballasted. They can in that case be towed to the wind farm locations and simply be placed on the seabed by ballasting them with rocks/gravel. The combined weight of the structure and the ballast provides the necessary stability and no drilling or hammering is needed, which makes the installation easy compared to the installation of monopiles. The seabed must however be prepared by replacing some of the seabed material with gravel and concrete and making it leveled. Gravity-based foundations for offshore wind power have about the same limits for water depths as monopiles, as the ballasting process and the weight of the structure becomes troublesome at large depths. The largest water depth at a wind farm with gravity-based foundations is 27.5 meters at Thornton Bank in Belgium. The largest offshore wind farm with gravity based foundations to date (in number of turbines and capacity) is Rødsand 2 in Denmark with 90 turbines and a total capacity of 207 MW (Lorc, Knowledge, 2011). Figure 1.3 shows a simple illustration of a gravity based foundation. The foundation is shown in grey. The term gravity-based foundation will be abbreviated as GBF throughout the text.

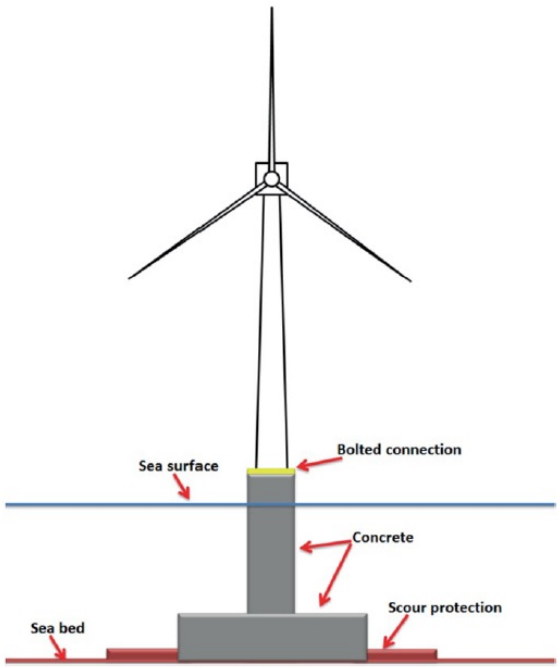

FIGURE 1.3: Gravity based foundation (Karimirad, 2014)

1.3 Previous work

Flows around piles have been studied extensively in the field of river hydraulics, as scour is a common cause of bridge failure. Piles or foundations in coastal and marine environments, with waves or waves in combination with currents have not been investigated as thoroughly (Sumer and Fredsøe, 2002, Chapter 1). As an example of the bridge failure problem, a 1991 survey of bridge failures since 1950 in the United States reportet that 60 % of the cases were due to scour or other types of hydraulic failure (Shirole and Holt, 1991). The present work is only concerned with currents (boundary layer flows). The following works are important contributions to the study of boundary layer flows around circular piles on a seabed:

Dargahi investigated experimentally the flow around a circular cylinder on a seabed at $8400 < Re < 46\ 000$, where the Reynolds number is based on the cylinder diameter and the mean flow velocity (Dargahi, 1989). Detailed measurements of velocities, pressure distributions and bed shear stresses were made at $Re = 39\ 000$. Flow visualization was achieved by using a hydrogen bubble flow visualization technique.

Roulund et al. investigated the flow and scour around a circular pile on a seabed under a wide range of conditions (Roulund et al., 2005). Flow with scour and flow on a rigid bed without scour was assessed both numerically and experimentally. The experimental data was obtained by Laser

Doppler Anemometry and hot-film bed shear stress measurements. The rigid-bed experiments were performed at $Re = 1.7 \times 10^5$ and $\delta/D = 1$, on a smooth bed and on a rough bed with roughness $k_s/D = 0.0187$. The scour experiements were performed at $Re = 4.6 \times 10^4$ and $\delta/D = 2$ with a roughness $k_s/D = 1.5$. The numerical investigations were performed with a k-ω turbulence model, at various conditions within the ranges $10^2 < Re < 2 \times 10^6$, $2 \times 10^{-2} < \delta/D < 10^2$ and $10^{-3} < k_s/D < 0.5$. The Reynolds numbers in the experimental cases were based on the mean flow velocity, and in the numerical cases on either the mean flow velocity or the free stream velocity. The Reynolds number, Re, and the boundary layer thickness, δ, were shown to have a large effect on the size of the horseshoe vortex in front of the pile and the bed shear stresses. The bed roughness was shown to be of secondary importance. This study is to the author's knowledge the only published study on flows around monopile foundations at $Re > 10^6$.

Flows around gravity-based foundations have not been studied extensively, at any Reynolds number. However, reports of experiences with the scour process around these foundations have accumulated over the years. O'Riordan and Clare surveyed published data on scour around gravity based foundations (O'Riordan and Clare, 1990) . They concluded that the most vulnerable locations on gravity-based foundations with respect to scour are:

(i) corners of the foundation
(ii) the leading skirt edge
(iii) around templates and pipelines outside the platform footprint

The scour process in it self is not a focus in the present study, but these experiences can be used to validate the bed shear stresses found in the numerical analyses.

1.4 Outline

Chapter 2 presents the relevant hydrodynamical theory for the thesis. This includes definitions of force and pressure coefficients, vortex shedding and the horseshoe vortex system that is found in flows around piles or foundations on a seabed.

Chapter 3 gives an introduction to Computational Fluid Dynamics and the software used in the work. Spalart-Almaras Delayed Detached Eddy Simulation and wall functions as used in the analyses are explained in detail. Turbulence modeling in general is described briefly.

Chapter 4 describes the computational model used in the present work, including the geometries of the foundations, the computational mesh, the boundary conditions and the numerical solving schemes.

Chapter 5 presents the results of the analyses. The convergence and quality of the results, the vortical structures of the flow, velocities and pressure distributions are shown in detail. Bed shear stresses around the foundations, which are a main focus in the study, are discussed in detail.

Chapter 6 gives a conclusion of the work and discusses possibilities for further work.

Chapter 2

Theory

2.1 Basic hydrodynamics

2.1.1 Reynolds number

The Reynolds number is a dimensionless parameter that expresses the ratio of inertial forces to viscous forces. It is defined as

$$Re = \frac{UD}{\nu} \tag{2.1}$$

Where U is a specified velocity, D a characteristic length of the geometry and ν the kinematic viscosity of the fluid. What quantities the Reynolds number is based on will be specified throughout the thesis. The Reynolds number is useful for determining if a flow is laminar or turbulent. At what Reynolds number the flow will be turbulent to a given degree differs from case to case. Figure 2.1 shows how the flow around a smooth, circular cylinder in a steady current changes as the Reynolds number increases. The flow is completely laminar up to $Re = 200$. At $Re > 4 \times 10^6$ the wake and boundary layer at both sides are completely turbulent. Various intermediate stages exists between these two extremes. The phenomenon of turbulence will be discussed more thoroughly in section 3.3. It is also seen that the flow separates on both sides of the cylinder at $Re > 5$, and that vortex shedding is present at $Re > 40$. Boundary layers, separation and vortex shedding will be discussed in section 2.1.2 and 2.1.3.

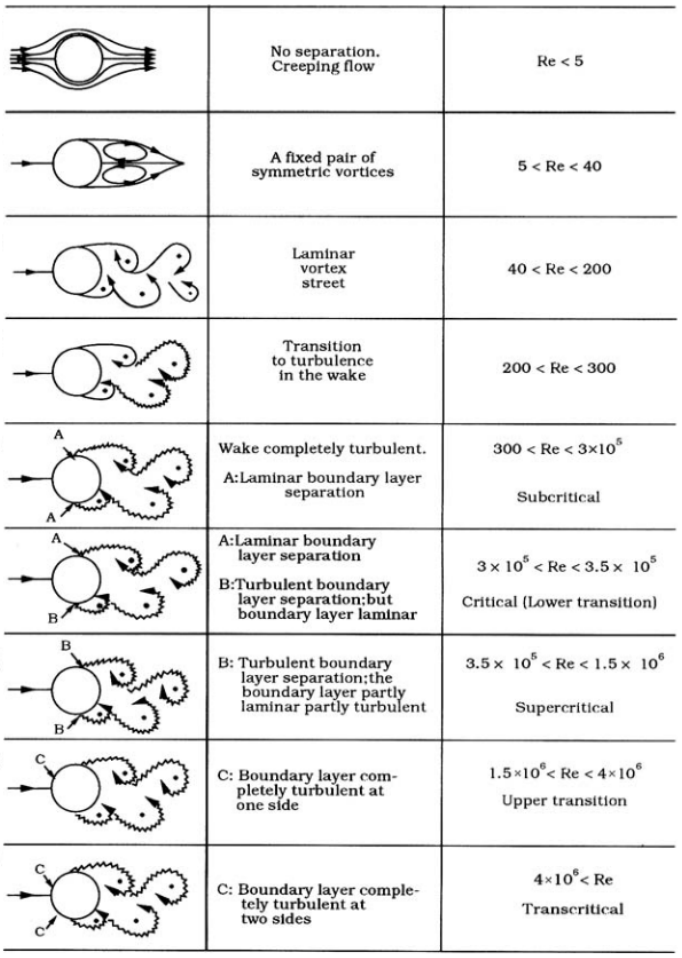

FIGURE 2.1: Flow regimes around a smooth, circular cylinder in a steady current at different Reynolds numbers. (Sumer and Fredsøe, 1997, Chapter 1)

2.1.2 Boundary layer

A boundary layer is a region in a flow close to a solid surface where the fluid velocity is slowed down due to the presence of the surface. This is due to viscosity and that the fluid velocity relative to the surface will be zero where the fluid and solid surface intersects. The latter condition is known as the no-slip condition. Figure 2.2 shows a typical appearance of a boundary layer. $u(y)$ is the velocity parallel to the wall which varies with the distance from the wall, y, and δ is the size of the boundary layer.

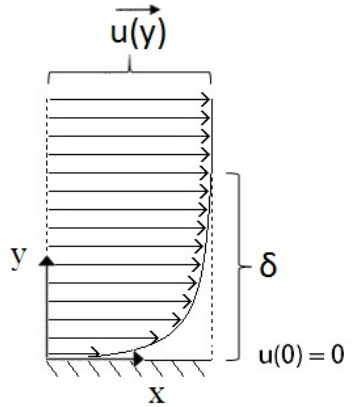

FIGURE 2.2: Scetch of a boundary layer

For a laminar boundary layer on a circular cylinder, we have the relationship

$$\frac{\delta}{D} = O\left(\frac{1}{\sqrt{Re}}\right) \tag{2.2}$$

(Sumer and Fredsøe, 1997, Chapter 1). Although this formula does not hold for turbulent flow or other geometries, it is generally true that δ decreases as Re increases.

2.1.3 Separation and vortex shedding

A geometry with a non-zero thickness in the cross-flow direction placed in a flow will lead to a contraction of the flow. In the case of a circular cylinder, as shown in figure 2.3, the velocity will increase on the top and bottom of the cylinder (except for very close to the surface). This causes the pressure to drop and then recover on the back side of the cylinder. Because of the no-slip condition on the surface, the pressure increase will lead to a back-flow and separation of the boundary layer from the surface. The location along the surface where backflow first occurs is called the separation point.

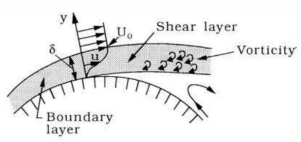

FIGURE 2.3: Separation on the upper side of a circular cylinder (Sumer and Fredsøe, 1997, Chapter 1)

Separation will lead to the formation of vortices on both sides of the cylinder because of the vorticity in the boundary layer. Under many conditions, e.g. for $Re > 40$ in the case of a smooth, circular cylinder, the vortices will be unstable and a phenomenon known as vortex

shedding will take place. Figure 2.4 illustrates this process. At a time instant a), vortex A is cut off by vortex B which will make it a free vortex traveling downstream and create a clockwise circulation around the cylinder. This creates the vortex C which will cut off vortex B at instant b) and create a counter-clockwise circulation. The process will continue in an alternating manner.

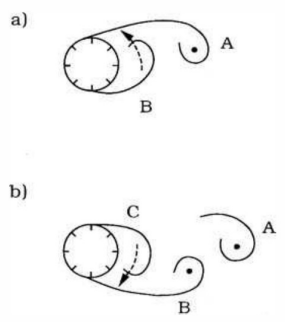

FIGURE 2.4: Vortex shedding from a circular cylinder (Sumer and Fredsøe, 1997, Chapter 1)

Vortex shedding will lead to non-constant forces on the geometry because of the alternating circulation, as shown in Figure 2.5. The cross flow force will vary harmonically about zero, while the force in the flow direction will vary harmonically with twice the frequency and a non-zero mean.

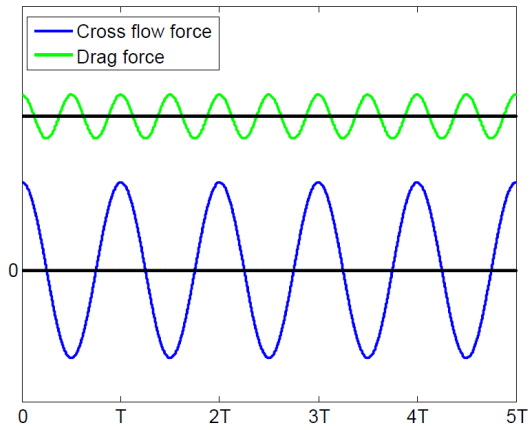

FIGURE 2.5: Example of cross flow and drag forces on a body caused by vortex shedding (Sketch by author)

2.1.4 Strouhal number

When the vortex shedding frequency of a circular cylinder in a steady current is non-dimensionalized by multiplying it by $\frac{D}{U_\infty}$, it is approximately 0.2 for a large range of Reynolds numbers. This non-dimensional frequency is known as the Strouhal number and is given by

$$St = \frac{f_v D}{U_\infty} \tag{2.3}$$

where f_v is the shedding frequency in Hertz. Figure 2.6 shows St as a function of Re for a smooth, circular cylinder in a steady current.

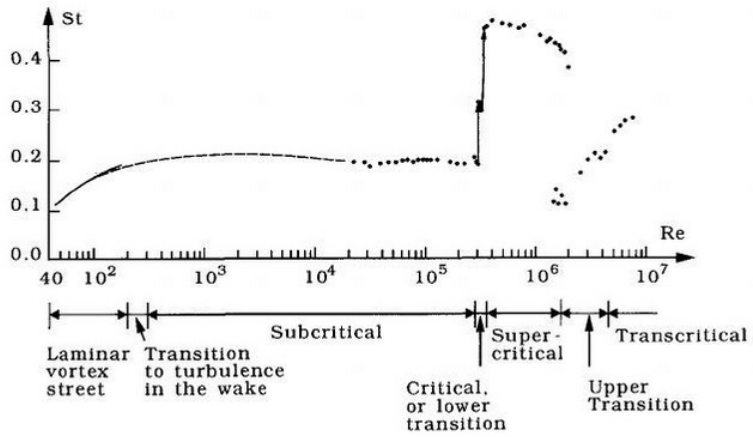

FIGURE 2.6: Strouhal number for a smooth, circular cylinder in a steady current as a function of Reynolds number (Sumer and Fredsøe, 1997, Chapter 1)

This relationship is different for different geometries, flow conditions or if roughness is added. The Strouhal number is commonly used as a measure of vortex shedding frequency in engineering practice.

2.1.5 Force coefficients

Forces on a body in a fluid are typically expressed as force coefficients:

$$C_x = \frac{F_x}{\frac{1}{2}\rho U_\infty^2 A_{proj}} \tag{2.4}$$

$$C_y = \frac{F_y}{\frac{1}{2}\rho U_\infty^2 A_{proj}} \tag{2.5}$$

F_x is the net force on the body in the x-direction, F_y the net force on the body in the y-direction, ρ the density of the fluid, U_∞ the free stream velocity and A_{proj} the projected area of the foundation. The terms *drag* or *in line* and *cross flow* will be used for forces in the x and y direction in this thesis, respectively. Force coefficient are often expressed by their mean value or their root mean square value. The mean and root mean square of a force coefficient C are defined as

$$\overline{C} = \frac{1}{N}\sum_{n=1}^{N} C_n \qquad C_{rms} = \sqrt{\frac{1}{N}\sum_{n=1}^{N} C_n^2} \tag{2.6}$$

where Cn is sampling point number n and N is the total number of sampling points. The shear stress on a seabed is often expressed as a ratio of the shear stress τ and the shear stress at a point on the seabed where the flow is undisturbed by the presence of the body, τ_∞. It is called the shear stress amplification factor or α in the present work:

$$\alpha = \frac{\tau}{\tau_\infty} \tag{2.7}$$

Bed shear stress can also be expressed as a force coefficient

$$C_\tau = \frac{\tau}{\frac{1}{2}\rho U_\infty^2} \tag{2.8}$$

where τ is given in Pascal. The one-dimensional definition of the shear stress on a wall from a fluid is

$$\tau = \mu \frac{du}{dz}\bigg|_{z=0} \tag{2.9}$$

where μ is the dynamic viscosity of the fluid, u the velocity of the fluid in the x-direction and z the normal distance from the wall. This shows that the shear stress on a wall is related to the gradient of the velocity. In a turbulent flow the shear stress can be calculated as

$$\tau = (\mu + \mu_t) \frac{d\overline{u}}{dz}\bigg|_{z=0} \tag{2.10}$$

where μ_t is the turbulent dynamic viscosity and $\overline{u}$ the averaged velocity over a time step in a turbulence model.

2.1.6 Pressure coefficient

The pressure coefficient is defined as

$$C_p = \frac{p - p_\infty}{\frac{1}{2}\rho U_\infty^2} \tag{2.11}$$

where p_∞ is the pressure in a reference point where the flow is undisturbed by the presence of the body.

2.2 Horseshoe vortex system

Figure 2.7 shows the horseshoe vortex system of a steady boundary layer flow around a monopile. The presence of a vertical circular pile on the seabed in a steady current will change the flow field. The most important new features are: 1) a horseshoe vortex in front of the pile; 2) vortices on the back side of the pile; 3) contraction of the flow; and 4) a downflow in front of the pile (Sumer and Fredsøe, 2002). The pressure gradient caused by the presence of the pile will lead to a separation of the boundary layer from the seabed in front of the pile. The separated boundary layer will roll up and form a horseshoe vortex. Vortex shedding may be present on the back side, depending on the flow regime. The downflow is caused by the vertical variation in pressure on the front side of the pile, due to the shape of the velocity profile. The pressure increase will be higher where the flow is decelerated the most, leading to the downflow.

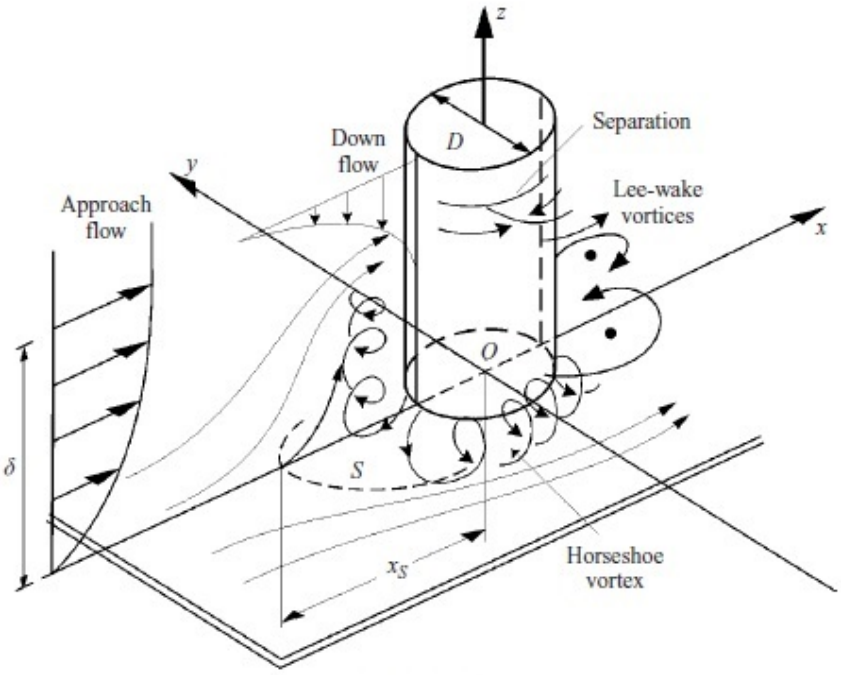

FIGURE 2.7: Vertical circular pile on a seabed in steady current with a horseshoe vortex system (Roulund et al., 2005)

2.3 Scour

The changes in the flow described in Section 2.2 will increase the sediment transport capacity close to the structure, mainly because of the increase in average bed shear stress and the increase of the degree of turbulence (Sumer and Fredsøe, 2002, Chapter 1). Sediment transport can roughly be divided into three main groups, namely bed load (on/in contact with the bed),

suspended load (not touching the bed) and dissolved load. The rate of sediment transport by bed load is connected to bed shear stress by

$$q_b \sim \tau^{3/2} \tag{2.12}$$

where τ must be larger than a threshold value for sediment transport to occur. The scour process will continue until the bed is eroded such that $\alpha = O(1)$, where alpha is given by Equation 2.7. The scour depth at this time is called the equilibrium scour depth. Figure 2.8 shows a typical scour hole around a circular, vertical pile (monopile).

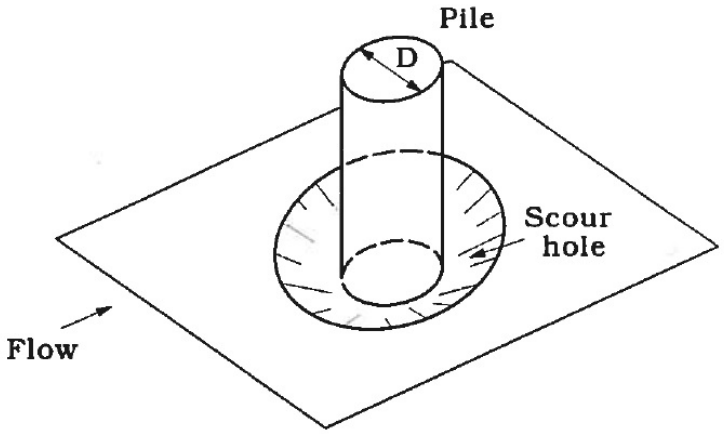

FIGURE 2.8: Sketch of a scour hole around a vertical pile (Sumer and Fredsøe, 2002, Chapter 3)

The scour process itself is not studied in the present work, its focus is the flow around foundations on a flat seabed before scour has taken place. However, properties of the flow that have importance for the scour process will be investigated.

Chapter 3

Computational fluid dynamics

Computational Fluid Dynamics, abbreviated as CFD, is a branch of numerical techniques used in combination with computers to solve problems in fluid dynamics. The vast majority of CFD problems are boundary value problems involving the Navier-Stokes equations. CFD is used in a wide range of fields, from aircraft design to meteorology. Many commercial codes (e.g. Ansys, STAR-CCM+) and non-commercial codes (e.g. OpenFOAM) exist today.

3.1 OpenFOAM

OpenFOAM, short for **Open F**ield **O**peration **A**nd **M**anipulation, is a free, open source software package designed to solve problems in continuum mechanics. This includes CFD, but also problems in e.g. electromagnetics and solid mechanics. OpenFOAM runs in a Linux environment, is written in C++ and arranged in text files that can be edited by the user. The not-for-profit organization The OpenFOAM Foundation manages the development and distribution of OpenFOAM (OpenFOAM Foundation, 2015). OpenFOAM 2.2.0 was used in the present study.

To run an analysis the user has to create a folder with three subfolders: **0** contains files that define the boundary conditions for the quantities involved in the analysis, **constant** has the files defining the mesh and the physical properties in the problem and **system** contains files defining the solving techniques and solving details.

3.1.1 Meshing and pre-processing

Meshing is the partitioning of a computational domain into smaller subdomains. The partitioned domain is called a mesh or a grid, and the resulting subdomains are called elements or cells. Very generally, areas with the largest pressure and velocity gradients require the smallest elements, and the resolution in the boundary layer is particularly important. It is also important to avoid abrupt changes in mesh density because of the way the problem is solved spatially with finite volume methods. Although OpenFOAM has meshing utilities, the commercial software Ansys ICEM CFD 14.5 has been used in the present work because of the high degree of control of the mesh it offer to the user. Meshing in the present study is discussed further in Section 4.3.

3.1.2 Solving

Solving methods

OpenFOAM solves the Navier-Stokes equations in space with finite volume methods. The user can specify schemes for interpolation from cell centers to face centers, schemes for the gradient terms, Laplacian term and so on. Time integration is done by finite difference methods. The user can choose from several methods, e.g. the backwards Euler method. At each time step, the initial solution from time integration is improved with an OpenFOAM solver that uses a looped algorithm to iterate the solution until the Navier-Stokes equations are satisfied within a (user) specified degree. OpenFOAM has a wide range of solvers for incompressible flow, compressible flow, potential flow and so on. The present study is only concerned with incompressible flow.

Courant number

The Courant number is a measure of stability when solving partial differential equations with explicit finite difference methods in time. The 1D Courant number is defined as

$$CFL = \frac{u\,\Delta t}{\Delta x} \leq CFL_{max} \tag{3.1}$$

u is here the velocity in a cell, Δt the time step and Δx the length of the cell in the x-direction. The Courant number must be below a maximum value that differs between methods. Implicit finite difference methods are more stable and the constraints on the Courant number are not as rigid. It should however be kept low as it affects the physics of the solution. A physical interpretation of the Courant number is that if $C > 1$, a fluid particle will travel farther than the length of the cell during the time-step.

3.1.3 Post-processing

OpenFOAM includes a wide range of post-processing utilities and a reading module called ParaView that can be used to visualize the results. ParaView 3.12.0 has been used in the present work for most of the 3D visualizations and contour plots. The 2D plots and some of the contour plots are made in MATLAB R2014a, with data extracted from ParaView.

3.2 Navier-Stokes equations

The Navier-Stokes equations give a complete mathematical description of Newtonian fluids under the continuum hypothesis. They consist of the momentum equation and the continuity equation. The momentum equation is derived from Newton's 2. law, which states that forces applied on a mass changes its momentum. It is a vector equation with one equation for each dimension. The incompressible momentum equation without gravity is:

$$\frac{\partial u_i}{\partial t} + u_j \frac{\partial u_i}{\partial x_j} = -\frac{1}{\rho}\frac{\partial p}{\partial x_i} + \nu \frac{\partial^2 u_i}{\partial x_j^2} \tag{3.2}$$

The continuity equation is a scalar equation expressing conservation of mass. The incompressible continuity equation is:

$$\frac{\partial u_j}{\partial x_j} = 0 \tag{3.3}$$

In this notation $(x, y, z) = (x_1, x_2, x_3)$ and $(u, v, w) = (u_1, u_2, u_3)$. The index i is the dimension (x = 1, y = 2, z = 3), and the terms are summed for j = 1,2,3.

3.3 Turbulence modeling

3.3.1 Turbulence

Turbulent flows are observed in many everyday phenomena, like in a waterfall, the smoke from a chimney or in the wake behind a ship. They are characterized by irregularity, fluctuations and eddies. Turbulence is fundamentally a three-dimensional phenomenon. This section describes some important properties of turbulence and the modeling of it.

Fluctuations

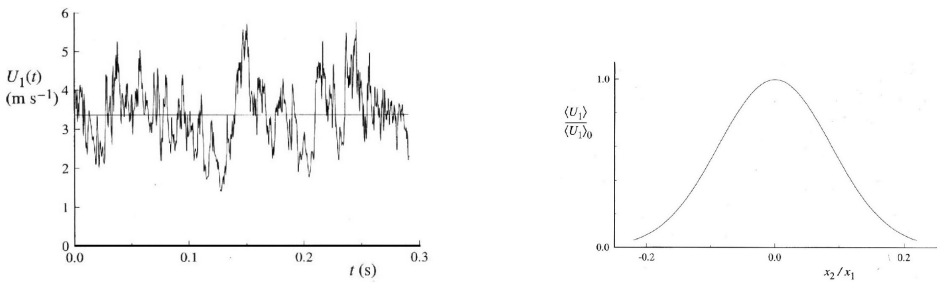

FIGURE 3.1: Velocity measurements in a turbulent jet (Pope, 2000, Chapter 1)

Figure 3.1 shows velocity measurements in a turbulent jet at Re = 95 500. The graph on the left shows the axial velocity at the centerline of the jet plotted against time, and the graph on the right the time-averaged axial velocity as a function of radial distance from the centerline. The axial velocity fluctuates in an irregular manner, but most values are close to the mean value and none differs greatly from it. It is also seen that the time-averaged velocity profile is smooth and similar to that of a laminar jet.

Eddies

Eddies are another characteristic of turbulence. "Turbulent Flows" (Pope, 2000, Chapter 6) writes: "An 'eddy' eludes precise definition, but it is conceived to be a turbulent motion, localized within a region of size l, that is at least moderately coherent over this region. The region occupied by a large eddy can also contain smaller eddies."

Energy cascade

A flow can not contain turbulence before energy is added to it. This is done by forces, typically as a result of the presence of a body in the flow. When energy is added, eddies are formed in the turbulent parts of the flow. They are unstable and will eventually break up and form smaller eddies, transferring their energy to them. This process continues until the eddies are so small that their energy is dissipated by the fluid's viscosity. This is known as the Energy Cascade (Pope, 2000, Chapter 6).

3.3.2 Direct Numerical Simulation (DNS)

Direct Numerical Simulation is the direct solving of the Navier-Stokes equations without any form of turbulence modeling, resolving eddies at all space and time scales. It has the advantage of high accuracy, but the downside of the high computational costs which increases sharply with the Reynolds number. Industrial applications are currently out of reach with DNS.

3.3.3 Large Eddy Simulation (LES)

Large Eddy Simulation is different from DNS in that it uses turbulence modelling for eddies that are smaller than the cell size. This is called subgrid-scale modelling. LES is computationally cheaper than DNS and sufficiently accurate for many industrial applications.

3.3.4 Reynolds-Averaged Navier Stokes (RANS)

Reynolds-Averaged Navier Stokes, abbreviated as RANS, is the most crude of the CFD methods. Everything in the computational domain is time-averaged over each time step. The velocities in a turbulent flow can be written as

$$U_i = u_i + u_i^{'} \tag{3.4}$$

where U_i is the total velocity, u_i is the average velocity over a time step and $u_i^{'}$ the fluctuating velocity component, all in direction i. In RANS it is assumed that the time-average of the fluctuating component over a time-step is zero, namely $\overline{u_i^{'}} = 0$. By inserting Equation 3.4 into the Navier-Stokes equations, the momentum and continuity equations become:

$$\frac{\partial u_i}{\partial t} + u_j \frac{\partial u_i}{\partial x_j} = -\frac{1}{\rho}\frac{\partial p}{\partial x_i} + \nu \frac{\partial^2 u_i}{\partial x_j^2} - \frac{\partial \overline{u_i^{'} u_j^{'}}}{\partial x_j} \tag{3.5}$$

$$\frac{\partial u_j}{\partial x_j} = 0 \tag{3.6}$$

The new term on the right-hand side in the momentum equation is expressed by the Reynolds stress component, $\overline{u_i^{'} u_j^{'}}$, a time average of a product of fluctuating velocities in the time-averaged interval. RANS models use the Boussinesq assumption, or eddy assumption, which states that the momentum transfer caused by turbulent eddies can be modeled as an increase in viscosity, the eddy viscosity. It is expressed as

$$-\overline{u_i^{'} u_j^{'}} = \nu_t \left(\frac{\partial u_i}{\partial x_j} + \frac{\partial u_j}{\partial x_i} \right) - \frac{2}{3}\, k\, \delta_{ij} \tag{3.7}$$

where δ_{ij} is the Kronecker delta, k the turbulent kinetic energy and ν_t the turbulent viscocity. Kronecker delta is defined as:

$$\delta_{ij} = \begin{cases} 0 & \text{if } i \neq j \\ 1 & \text{if } i = j \end{cases}$$

Closure can be obtained with zero-, one- or two-equation models. Well-known RANS models like k-ϵ and k-ω are two-equation models. The Spalart-Allmaras model is an example of a one-equation model.

3.3.5 Detached Eddy Simulation (DES)

DES (and similar methods such as DDES, IDDES etc.) uses RANS near walls and LES elsewhere. DES has a lower computational cost than LES, and performs well in cases with e.g. massive separation where RANS performs poorly. DES and DDES are described in Section 3.4.2. Figure 3.2 illustrates the differences between DNS, LES and RANS in terms of accuracy.

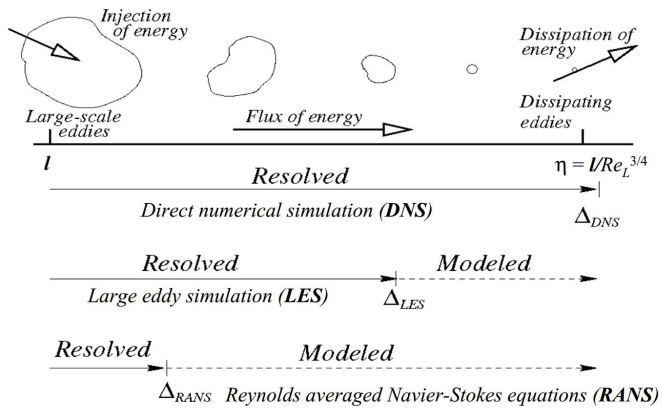

FIGURE 3.2: Comparison of CFD methods in terms of accuracy (Bakker, A.,)

3.4 Spalart-Allmaras Delayed Detached Eddy Simulation (SADDES)

The present study employs Spalart-Allmaras Delayed Detached Eddy Simulation, or SADDES, where the Spalart-Allmaras turbulence model is used both as a RANS model in the RANS regions and as a subgrid scale model in the LES regions.

3.4.1 Spalart-Allmaras turbulence model

The Spalart-Allmaras turbulence model was developed by P. R. Spalart and S. R. Allmaras in 1992 (Spalart and Allmaras, 1992). It models the Reynolds stress in the RANS equations with a one-equation model, making it computationally cheaper than two-equation models like e.g. k-ϵ. The original model is described in the following. The version of it implemented in OpenFOAM is slightly different and will be described thereafter.

Original model

A one-equation approach is possible by neglecting the term $\frac{2}{3}k\delta_{ij}$ in the Boussinesq assumption. This is not a major effect in thin shear flows, i.e. at high Reynolds numbers. The Reynolds stress component is then given by:

$$-\overline{u_i' u_j'} = \nu_t \left(\frac{\partial u_i}{\partial x_j} + \frac{\partial u_j}{\partial x_i} \right) \tag{3.8}$$

The model uses a transport equation for a working variable $\tilde{\nu}$, which is defined by

$$\nu_t = \tilde{\nu} f_{v1} \qquad f_{v1} = \frac{X^3}{X^3 + C_{v1}^3} \qquad X = \frac{\tilde{\nu}}{\nu} \tag{3.9}$$

where the subscript v stands for viscous. The transport equation is:

$$\frac{D\tilde{\nu}}{Dt} = c_{b1}(1-f_{t2})\tilde{S}\tilde{\nu} + \frac{1}{\sigma}\left[\nabla\Big((\nu+\tilde{\nu})\nabla\tilde{\nu}\Big) + c_{b2}(\nabla\tilde{\nu})^2\right] - \left[c_{w1}f_w - \frac{c_{b1}}{\kappa^2}f_{t2}\right]\left(\frac{\tilde{\nu}}{d}\right)^2 + f_{t1}\Delta U^2 \tag{3.10}$$

The left hand side of Equation 3.10 is the Lagrangian or material derivative of $\tilde{\nu}$. $\tilde{S}$ is given by

$$\tilde{S} = S + \frac{\tilde{\nu}}{\kappa^2 d^2} f_{v2} \qquad f_{v2} = 1 - \frac{X}{1 + X f_{v1}}$$

where S is the magnitude of the vorticity and d the distance to the closest wall. The function f_w is defined as

$$f_w = g\left[\frac{1 + c_{w3}^6}{g^6 + c_{w3}^6}\right]^{1/6} \qquad g = r + c_{w2}(r^6 - r) \qquad r = \frac{\tilde{\nu}}{\tilde{S}\kappa^2 d^2}$$

where the subscript w stands for wall. f_{t1} and f_{t2} are called trip functions, and are given by

$$f_{t1} = c_{t1} g_t exp\Big(- c_{t2}\frac{\omega_t^2}{\Delta U^2}\left[d^2 + g_t^2 d_t^2\right]\Big) \qquad f_{t2} = c_{t3} exp(-c_{t4}X^2)$$

A trip point is a transition point in the boundary layer from laminar to turbulent flow. d_t is the distance from the field point to the trip, ω_t the wall vorticity at the trip point and ΔU the velocity difference between the field point and the trip point. $g_t = min(0.1, \Delta U/\omega_t \Delta x)$ where Δx is the grid spacing along the wall at the trip.

The constants in the model are: $c_b = 0.1355$, $\sigma = 2/3$, $c_{b2} = 0.622$, $\kappa = 0.41$, $c_{w1} = \frac{c_{b1}}{\kappa^2} + \frac{1+c_{b2}}{\sigma}$, $c_{w2} = 0.3$, $c_{w3} = 2$, $c_{v1} = 7.1$, $c_{t1} = 1$, $c_{t2} = 2$, $c_{t3} = 1.1$ and $c_{t4} = 2$. The subscript b stands for basic.

OpenFOAM model

The Spalart-Allmaras version implemented in OpenFOAM is called the f_{v3}-implementation. It is meant for fully turbulent flow, and so the trip terms f_{t1} and f_{t2} are neglected. $\tilde{S}$ and f_{v2} are modified to

$$\tilde{S} = f_{v3}S + \frac{\tilde{\nu} f_{v2}}{\kappa^2 d^2} \qquad f_{v2} = \frac{1}{(1+\frac{X}{c_{v2}})^3} \qquad f_{v3} = \frac{(1+Xf_{v1})(1-f_{v2})}{X} \qquad c_{v2} = 5$$

The f_{v3}-implementation is described in (Gainer et al., 2001).

3.4.2 DDES

DDES (where the extra D is for Delayed) is an improved version of DES (Spalart et al., 2006). Both models use a length scale $\tilde{d}$ as a criterion for switching between LES and RANS. In DES, $\tilde{d}$ is defined as

$$\tilde{d}_{DES} = min(d, C_{DES}\Delta) \tag{3.11}$$

where C_{DES} is a constant of order 1 and $\Delta = max(\Delta x, \Delta y, \Delta z)$. If $\tilde{d} = d$ RANS is used, and if $\tilde{d} = C_{DES}\Delta$ the solver switches to LES mode with the Spalart-Allmaras turbulence model as a subgrid-scale model. The same criterion applies to DDES, but $\tilde{d}$ is modified in order to delay the switch from RANS to LES. This is to avoid using LES on content that can not be properly modelled by LES. The new $\tilde{d}$ is defined as

$$\tilde{d}_{DDES} = d - f_d max(0, d - C_{DES}\Delta) \tag{3.12}$$

where $f_d = 1 - tanh([8r_d]^3)$ and $r_d = (v_t + v)/(\tilde{S}\kappa^2 d^2)$. The role of ν is to prevent r_d from going to zero very near walls. The subscript d stands for delayed. An important difference between the DES and DDES formulations is that DES only depends on the computational mesh, while DDES also depends on the solution itself. DDES is shown to perform better than DES in comparisons with experimental data (Spalart et al., 2006).

3.5 Turbulent velocity profiles and wallfunctions

If we study the boundary layer of a turbulent flow over a flat plate, it is found that it has four distinct regions. Innermost is a small sublayer known as the viscous sublayer, where viscous effects dominate and the velocity profile is practically linear. The next sublayer is called the buffer layer, which has significant turbulent effects, but is dominated by viscous effects. Third is the overlap sublayer, or logarithmic layer, where turbulent effects are more significant still, but not dominating. The velocity profile in the overlap sublayer has a logarithmic shape. The last sublayer is the outer or turbulent sublayer, where turbulent effects are dominating (Cengel and Cimbala, 2010, Chapter 8).

The velocity parallel to the wall and the normal distance from the wall in the boundary layer are commonly expressed non-dimensionally as u^+ and y^+, respectively:

$$u^+ = \frac{U}{u_\tau} \tag{3.13}$$

$$y^+ = \frac{u_\tau\, y}{\nu} \tag{3.14}$$

Here $u_\tau = \sqrt{\frac{\tau_w}{\rho}}$ is the friction velocity, y the normal distance from the wall and ν the kinematic viscosity. τ_w is the wall shear stress and ρ the fluid density. The linear relationship in the viscous sublayer can then be expressed as:

$$u^+ = y^+ \tag{3.15}$$

This is known as the law of the wall, and is valid for $y^+ < 5$. The logarithmic shape in the overlap sublayer can be written as:

$$u^+ = \frac{1}{\kappa} ln(Ey^+) \tag{3.16}$$

$\kappa = 0.41$ and $E = 9.8$ in OpenFOAM for smooth walls (OpenFOAM Ltd, 2015). This is known as the logarithmic law, or log-law, and it is valid for $30 < y^+$ up to around $y^+ = 1000$. The logarithmic law is close to accurate in the turbulent sublayer. Neither of these laws fit in the buffer layer, i.e. $5 < y^+ < 30$. Figure 3.3 shows a plot of u^+ as a function of y^+ and the location of the different sublayers.

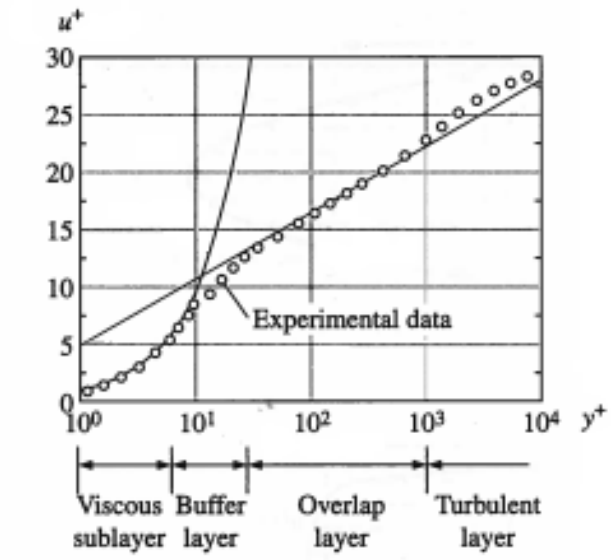

FIGURE 3.3: Sublayers in a turbulent boundary layer (Cengel and Cimbala, 2010, Chapter 8)

The law of the wall and the logarithmic law are based on the assumption of a flat plate without a pressure gradient, but are reasonable approximations in most cases of attached boundary layer flows. This is exploited in many turbulence models through wall functions. The user can set the normal distance from a wall to the first node in the mesh away from the wall at a value corresponding to y^+ slighly over 30, and the solution in the first cell is set by the code by using these relationships. Without wall functions the boundary layer would have to be densely meshed below $y^+ = 30$ which would be more computationally demanding.

Chapter 4

Computational model

The flow around three different bottom-fixed foundations for offshore wind turbines has been modeled in OpenFOAM with Spalart-Allmaras Delayed Detached Eddy Simulation at Reynolds number 4×10^6. The details of the computational model are described in this chapter.

4.1 Geometry

4.1.1 Lillgrund wind farm

Lillgrund Offshore Wind Power Plant is located in the Øresund strait in Sweden. It is 7 km off the coast of Sweden, 9 km of the coast of Denmark and 7 km south of the Øresund bridge. The water depth ranges from 4 to 8 meters at the location of the farm. It consists of 48 wind turbines with a total capacity of 110 MW. The park has been in operation since December 2007 (Jeppsson et al., 2008).

The foundations at Lillgrund have a typical gravity based foundation design, similar to the foundations used at e.g Rødsand I (Nysted), Rødsand II, Middelgrunden and Kårehamn wind farms. Figure 4.1 and 4.2 show the dimensions of the foundation design. The most important information was added to the figures in red. We see that the foundation consists of three main parts: a six-sided bottom slab, a cylindrical shaft and a conical shape at the top for ice protection. The foundations are made of reinforced concrete, and were cast directly on barges in a construction site in Poland which were towed to the wind park location. The foundations were ballasted and placed on a prepared seabed at the site.

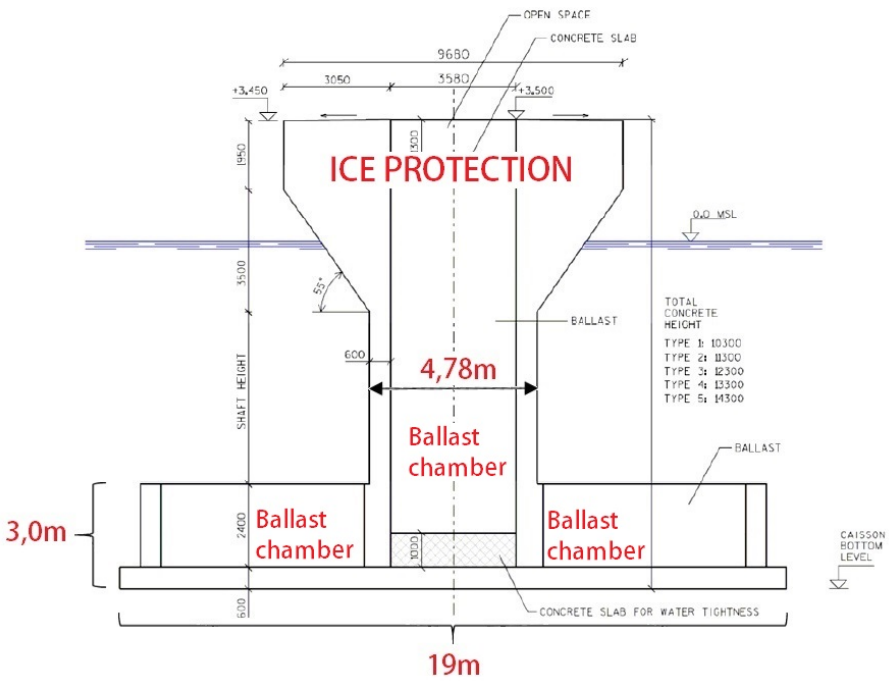

FIGURE 4.1: Section of the Lillgrund wind farm foundation (Jeppsson et al., 2008). The information shown in red was added to the original Figure.

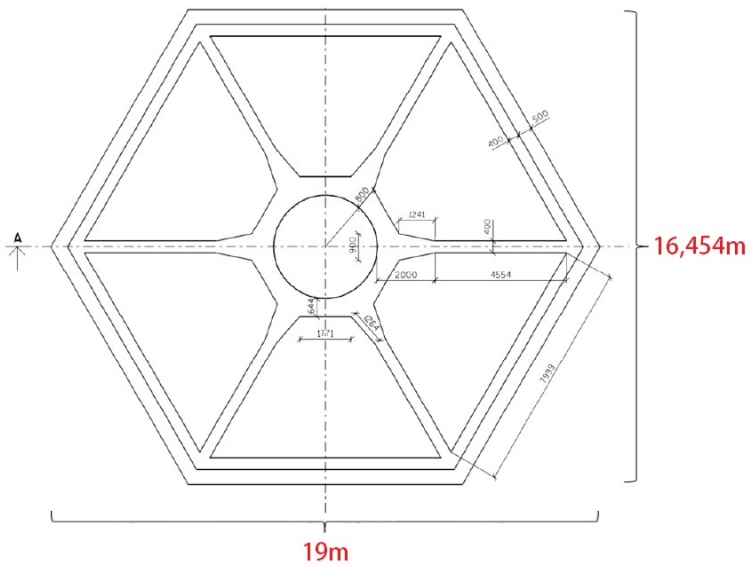

FIGURE 4.2: Bottom slab of the Lillgrund wind farm foundation (Jeppsson et al., 2008). The information shown in red was added to the original Figure.

4.1.2 Geometry in the analyses

Three different geometries are used in the numerical analyses. One is a simplified model of the Lillgrund foundation. It will be referred to as the hexagonal GBF. Another is identical to the hexagonal foundation, except for that the bottom slab has a cicular shape. It will be referred to

as the circular GBF. The third geometry is a monopile foundation, referred to as the monopile or monopile foundation.

All geometries have the same length in the y-direction on the seabed, called D. D is also the diameter of the monopile foundation and of the bottom slab of the circular GBF.

Hexagonal GBF

Figure 4.3 shows the hexagonal GBF. The bottom slab is a equilateral hexagon. Some alterations have been done to the the original geometry of the Lillgrund Foundations. The ice protection is not included and the height of the cylindrical shaft is extended. This is done so that the total height is equal to that of the monopile. The monopile height is set equal to that in the study by (Roulund et al., 2005), $2D$, to make the structure slender. These changes will have a negligable effect on the flow near the seabed and the bottom slab, which is the main focus of the study.

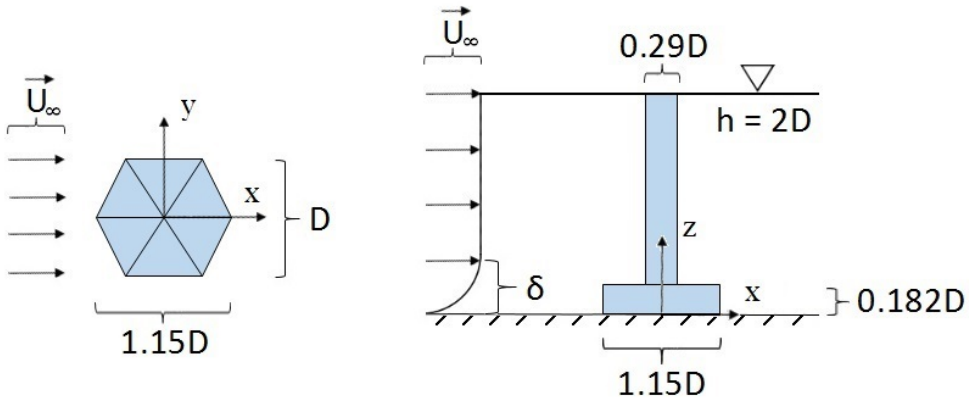

FIGURE 4.3: Geometry of the hexagonal GBF. Sketch by the author.

Circular GBF

Figure 4.4 shows the circular GBF. It is identical to the hexagonal GBF, except that the bottom slab is circular with a diameter D.

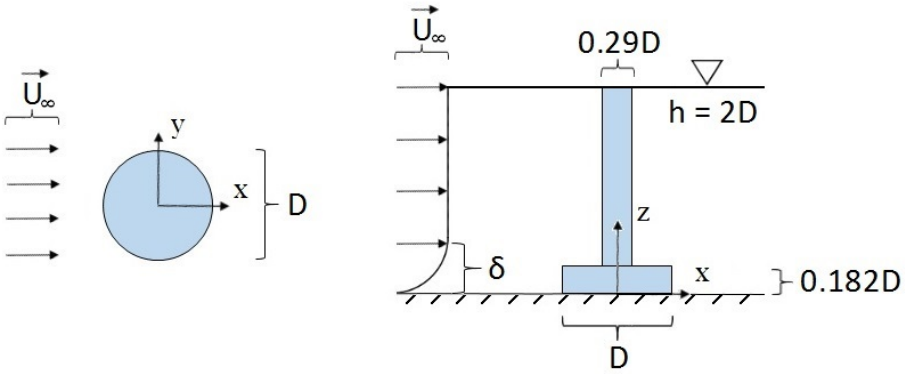

FIGURE 4.4: Geometry of the circular GBF. Sketch by the author.

Monopile

Figure 4.5 shows the monopile foundation. The diameter is D.

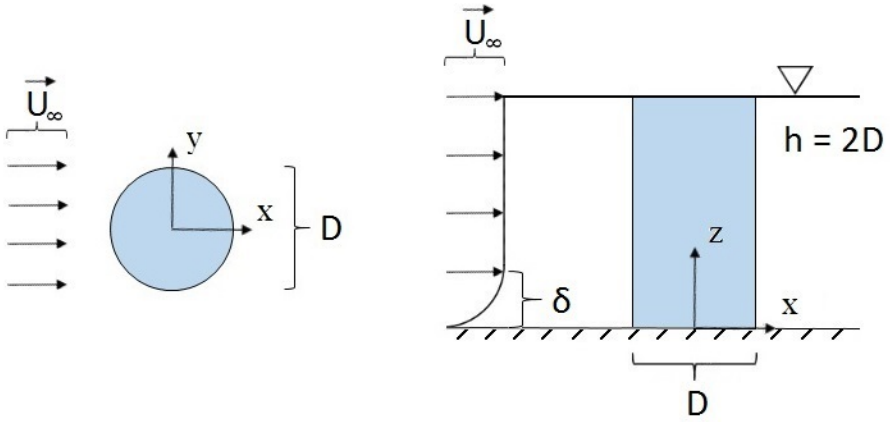

FIGURE 4.5: Geometry of the monopile foundation. Sketch by the author.

3D view

Figure 4.6 shows a 3D view of the three foundations in the meshing software ICEM CFD. The grey lines are added to show the surfaces more clearly and do not represent the mesh.

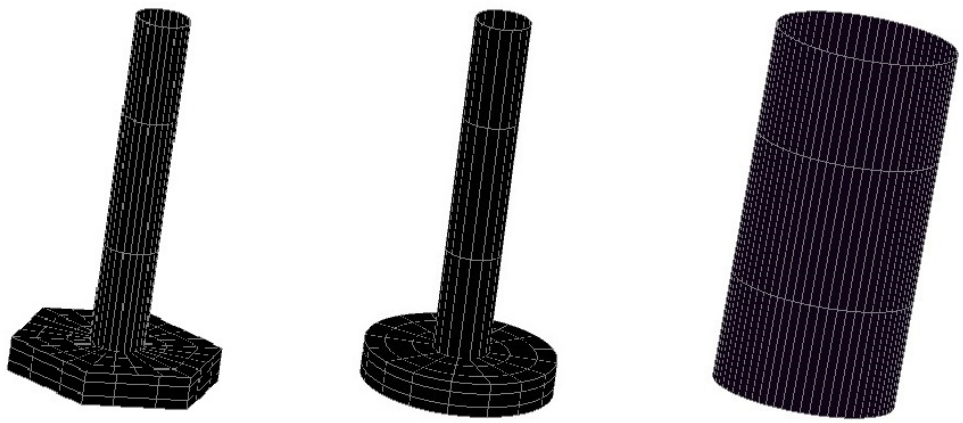

FIGURE 4.6: Three-dimensional view of the three foundation geometries used in the analyses. Left to right: hexagonal GBF, circular GBF and monopile

4.2 Conditions

4.2.1 Reynolds number

The Reynolds number is based on D, the free stream velocity U_∞ and the kinematic viscosity ν. The Reynolds number is set to 4×10^6 in all the analyses. Similarity in Re based on D is used so that the same level of turbulence near the bottom of the foundations is obtained. One can easily argue that a Reynolds number as high as 4×10^6 based on free stream velocity is realistic. With $D = 16.454$ (Lillgrund) and $\nu = 10^{-6}$, this corresponds to a free stream velocity of 0.24 m/s, which is not particularly high.

4.2.2 Boundary layer

Roulund et al. shows that for $Re = 2 \times 10^5$, based on the free stream velocity and with a smooth bed, that the boundary layer thickness has a significant effect on the horseshoe vortex size and bed shear stress up to $\delta/D = 1$, but virtually no effect when $\delta/D > 1$ (Roulund et al., 2005). The horseshoe vortex size is in this context the distance from the center of the monopile to the separation point in front of the pile along the line $y/D = 0$, $z/D = 0$, and the bed shear stress the maximum bed shear stress along this line.

$\delta/D = 1$ in the present study. The published data used for comparison with the present work uses various values of δ/D larger than 1. Based on the argument above, the difference in δ/D is assumed to have no effect on the results for the horseshoe vortex size and bed shear stress as

measured by Roulund et al. (but differences in the Reynolds number, bed roughness etc. will have an effect of its own).

4.2.3 Boundary conditions

Figure 4.7 shows the computational domain used for the analyses. It measures $20D \times 20D \times 2D$, which is the same domain as in the study by (Roulund et al., 2005).

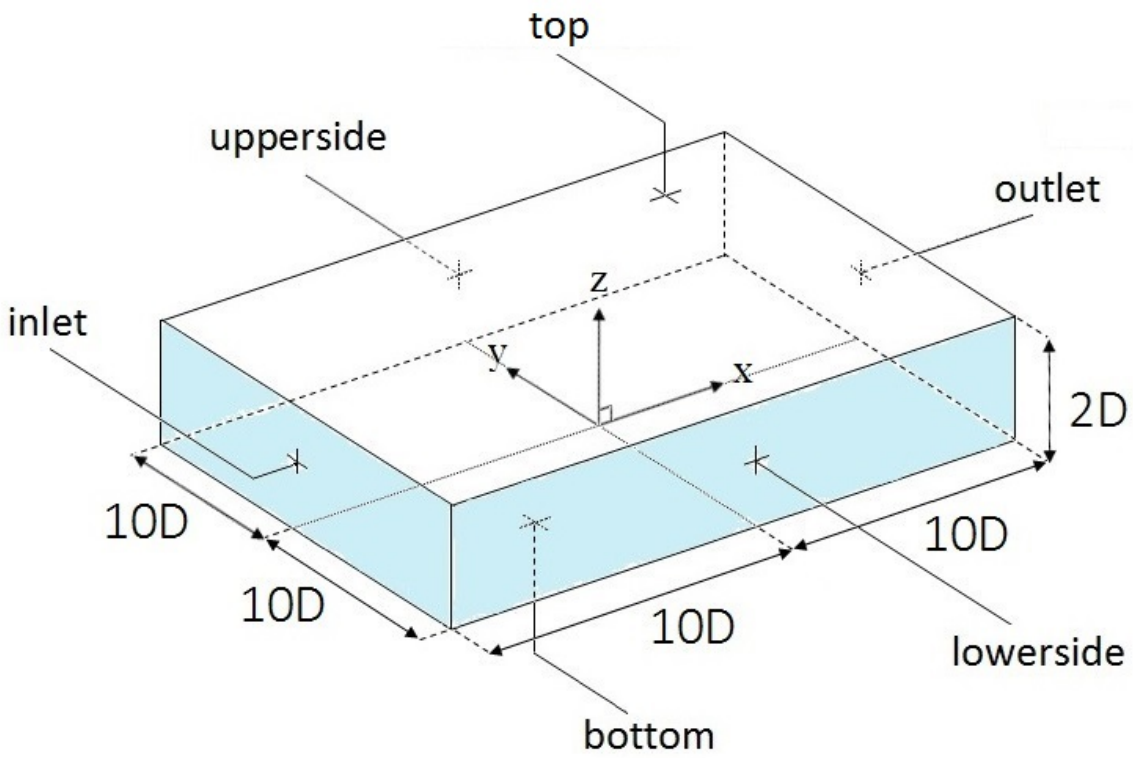

FIGURE 4.7: Computational domain. Sketch by the author.

The Spalart-Allmaras DDES model in OpenFOAM requires boundary conditions for U, p, ν_t and $\tilde{\nu}$. U is the three-dimensional velocity vector, i.e. $U = (u, v, w)$, p is the pressure, ν_t the turbulent viscosity and $\tilde{\nu}$ the working variable in the Spalart-Allmaras transport equation. ν_t is the turbulent viscosity when the RANS mode is used and the turbulent viscocity for the subgrid-scale when the LES mode is used.

Inlet

The inlet profile can be obtained in different ways. (Roulund et al., 2005) used equilibrium profiles obtained from a separate uniform-channel flow calculation. This is a reasonable approach,

but it is time consuming. Using experimental data is another method, but experimental data does not exist the relevant range of Reynolds numbers and quantities such as ν_t are not easily available from experimental studies in general. The inlet values for u, v, w and ν_t are taken or derived from (Ong et al., 2010), who used a boundary layer velocity profile as an inlet condition in a study of two-dimensional flow around a circular cylinder close to a flat seabed. The study was performed at $10^4 < Re < 1.36 \times 10^4$ using RANS with a k-ϵ model for closure.

The inlet velocity profile is given as

$$u = min\left\{\frac{u_\tau}{\kappa} ln\left(\frac{z}{z_w}\right), U_\infty\right\} \tag{4.1}$$

where the friction velocity is defined as $u_\tau = \frac{\kappa U_\infty}{ln(\delta/z_w)}$. z_w is the seabed roughness, set to a very small value of 1×10^{-6}. The roughness z_w is added to the seabed and the foundations. The small roughness has an insignificantly effect on the results compared to that of a smooth wall, but enhances the numerical stability of the simulations (Ong et al., 2010). v and w are set to zero at the inlet. The ν_t distribution at the inlet is found by using the definition of turbulent viscosity in the k-ϵ model, so that

$$\nu_t = \frac{C_\mu k^2}{\epsilon} \tag{4.2}$$

The turbulent kinetic energy k and rate of dissipation of turbulent kinetic ϵ energy are given by

$$k = \begin{cases} max\left\{C_\mu^{-\frac{1}{2}}\left(1 - \frac{z}{\delta}\right)^2 u_\tau^2, 0.0001U_\infty^2\right\} & \text{if z} \leq \delta \\ 0.0001U_\infty^2 & \text{if z} > \delta \end{cases}$$

$$\epsilon = \frac{C_\mu^{3/4} k^{3/2}}{l}$$

respectively, where the turbulent length scale l is

$$l = min\left\{\kappa z\left(1 + 3.5\frac{z}{\delta}\right)^{-1}, C_\mu \delta\right\} \tag{4.3}$$

The constant C_μ is 0.09. The OpenFOAM condition zeroGradient is used for the pressure at the inlet. A zeroGradient condition means that the gradient of the specified quantity is zero in the direction normal to the boundary.

$\tilde{\nu}$ is set equal to ν_t on the inlet boundary in the present study. (Kalitzin et al., 2005) argues that for the flow over a flat plate with a zero-gradient (the conditions where the law of the wall is valid), $\nu_t = \tilde{\nu}$ in the logarithmic sublayer when the Spalart-Allmaras turbulence model is used. This is not true in the viscous sublayer and the intermediate layer, but the discrepancy in the areas closer to the wall will quickly be corrected downstream of the inlet because of the use of wall functions.

Walls: Bottom and foundation

A nutUSpalding wall function is used for ν_t on the bottom and foundation boundaries. (Ong et al., 2009) studied the two-dimensional flow around a smooth circular cylinder at $Re = 1 \times 10^6, 2 \times 10^6$ and 3.6×10^6 using a k-ϵ model with wall functions. The results of the study were concluded to be satisfactory for engineering design purposes in the supercritical and upper-transitional flow regimes, i.e. $Re > 10^6$. A wall function approach in the present study is therefore assumed to be reasonable.

The no-slip condition, $U = (u, v, w) = (0, 0, 0)$ is enforced on the walls. The pressure is set to a zeroGradient condition. ν_t at the first node away from walls is found from the standard near-wall conditions for k and ϵ:

$$k = \frac{u_\tau^2}{\sqrt{C_\mu}} \qquad \epsilon = C_\mu^{3/4} \frac{k^{3/2}}{\kappa h_p}$$

h_p is the normal distance to the node closest to the wall. Using $\nu_t = \frac{C_\mu k^2}{\epsilon}$ and $y^+ = \frac{u_\tau h_p}{\nu}$, we get a near wall condition for ν_t:

$$\nu_t = \nu \kappa y^+ \tag{4.4}$$

y^+ is here the average y^+ obtained from the analyses. The mesh is constructed (by adjusting h_p) so that the average y^+ is approximately 30 at both the seabed and the foundation. $\tilde{\nu}$ does not need a wall function, as it is coupled with ν_t by Equation 3.10. It is set to zero on the walls.

Outlet, top, upperside and lowerside

The pressure is set to zero at the outlet. All the other quantities are set to zeroGradient on these boundaries.

The input files used in the **0** folder in OpenFOAM are found in Appendix A.1. ν_t is here called "nuSgs" (subgrid-scale) and $\tilde{\nu}$ called "nuTilda". A file "nut" also exists, which only has the role of adding the small roughness to the bottom and foundation boundaries.

4.3 Computational mesh

All computational meshes in the present study are of the type **structured mesh**. The computational mesh is finest where the changes in pressure and velocities are highest, which is near surfaces and corners. As a rule of thumb, the mesh should not be too coarse in the wake area from the foundation surface out to around $3 \times D$ downstream. For example, between 90 and 94 % of the cells in the monopile meshes are located within a radius of $5 \times D$ measured from the center of the pile. The meshes for the gravity-based foundations are created in the same way.

The computational domain has been divided into blocks for better control of the cell distribution. The number of partitionings (into cells) and type of density distribution can be set at the edges of the blocks in ICEM CFD. The domain of the hexagonal GBF, circular GBF and monopile are divided into 66, 44 and 24 blocks, respectively. Figure 4.8 shows how the domain for the hexagonal GBF is divided into blocks.

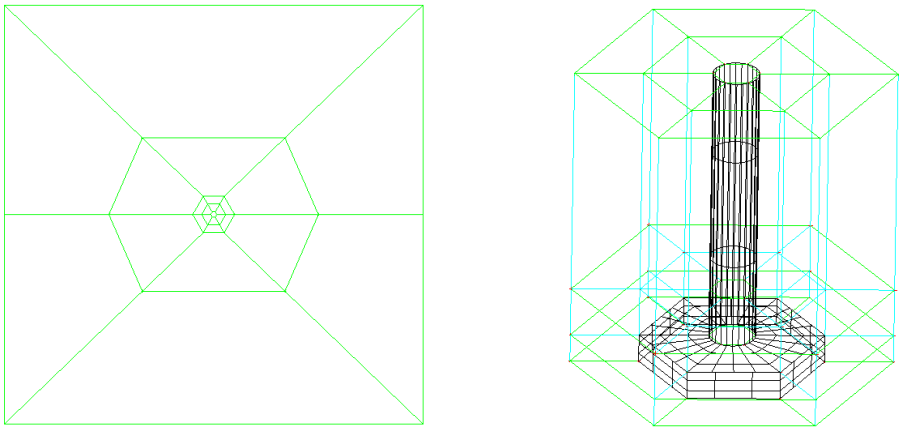

FIGURE 4.8: Blocks in the mesh for the hexagonal gravity-based foundation. Birds view (left) and close to the foundation (right)

3 meshes with a different number of cells have been created for each of the foundations. The number of cells ranges from 2.96 million to 5.032 million. Areas close to the seabed (bottom boundary) and the foundation are meshed for use of RANS and wall functions with $h_p = 0.0005D$ and exponential cell growth out from the walls. The growth ratios at the foundation are in the range of 4.78 - 6.06 % for the monopile, 8.02 - 53.7 % for the circular GBF and 7.51 - 74.4 % for the hexagonal GBF. The highest growth ratios are only found in the coarsest meshes, and

most growth ratios are well below 30 %. The growth ratios at the seabed are 15.1 % for the monopile and 76.2 - 87.3 % for both the circular and the hexagonal GBF. It must be mentioned that a decrease in cell growth ratio from the seabed for the GBF meshes would give a very rapid increase in total number of cells (and computational time). Figure 4.9 illustrates how the mesh for the gravity-based foundations have a different structure than the mesh for the monopile foundations, which will give a higher number of cells if the resolution is the same close to walls.

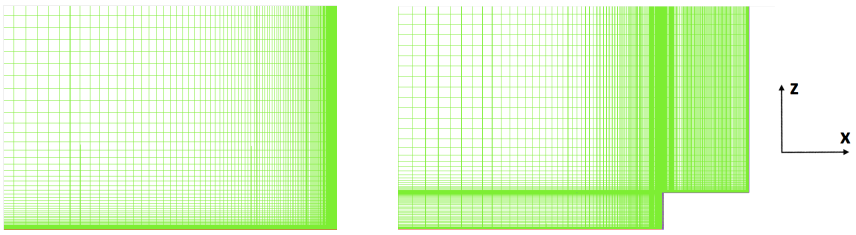

FIGURE 4.9: monopile foundation (left) and gravity-based foundation (right) mesh, shown in the y = 0 plane.

Figure 4.10 shows a two-dimensional view of a monopile mesh, as a whole and in a close-up view. A 3D view of the mesh on the surface of the three foundations is shown in Figure 4.11.

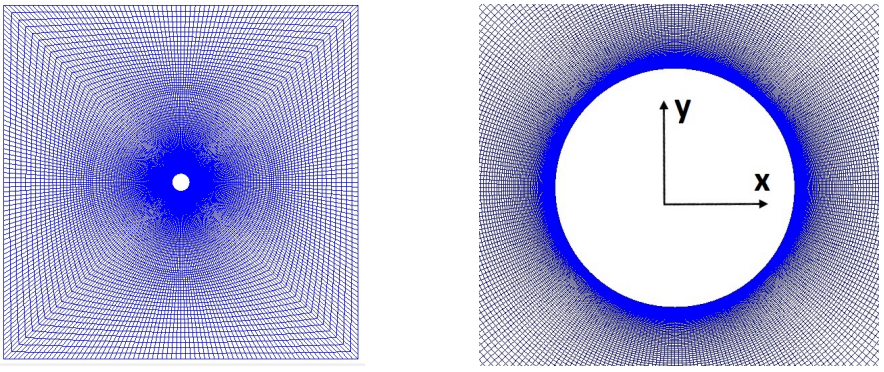

FIGURE 4.10: Computational mesh for the monopile foundation. Full mesh (left) and close up view (right).

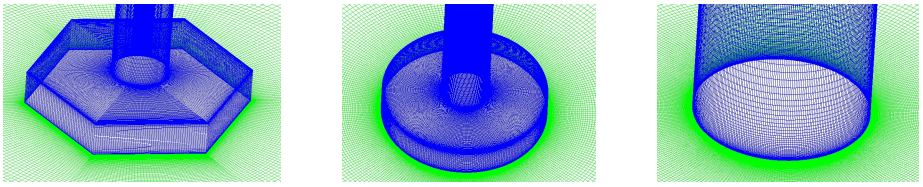

FIGURE 4.11: Close up of the mesh on the surface of the foundations

4.4 OpenFOAM and High Performance Computing setup

OpenFOAM

A linear Gaussian finite volume integration is used in the present study. A second order backwards (implicit) Euler method is used for the time integration. The transient solver for incompressible flow pisoFoam (Pressure Implicit with Splitting of Operators) is used. The case files that specify the details for finite volume integration, finite difference methods and error tolerance, fvSchemes and fvSolution, are found in Appendix A.2.

The function library swak4Foam (SWiss Army Knife for OpenFOAM) has been used to enforce the inlet boundary conditions as mathematical expressions. Wall shear stresses, vortical structures, vorticity, Courants number and y^+ were found using the OpenFOAM post processing utilities wallShearStressLES, Q, vorticity, Co and yPlusLES.

High Performance Computing

The high performance computer Vilje at NTNU was used for the analyses. It uses a Linux environment. It has a total of 1404 nodes, each with 2 processors and 32 GB memory. Each processor has 8 cores and a processor speed of 2.6 GHz. The majority of analyses were run on 6 nodes, with parallel computing where the domain was partitioned into 96 subdomains. Around 300 000 (three hundred thousand) core hours have been used in total.

4.5 Effects not included in the model

Gravity is neglected from the analysis, as in the published numerical data used for comparison in the thesis. Neglecting gravity will not have an effect on the flow as the weight of the water particles would be in equilibrium with the static pressure. Static pressure would not have an effect on the cross flow and drag force coefficients that are of interest.

The model does not have a free surface facility. In an experiement the flow would cause an elevation of the water surface in front of the foundation and a drop on the back side. Roulund et al. argues that if F_n based on water depth is smaller than $O(0.2)$, this difference in surface elevation would be so small that it will have no significant effect on the flow (Roulund et al., 2005). The results of the presents study are taken to be valid if $F_n = \frac{U}{\sqrt{gh}} < O(0.2)$. In the example of the Lillgrund wind farm, $F_n = 0.0134$.

Chapter 5

Results and discussion

The results of the analyses are presented in this section. The results are based on the computational meshes Monopile3, Hexagonal3 and Circular2 for the monopile, hexagonal GBF and circular GBF foundations, respectively. Results for pressures and velocities are time averaged over a time span $T = 50\frac{D}{U_\infty}$ with the fieldAverage function in OpenFOAM, which calculates the average based on all the time-steps in the chosen time span. Quantities such as wall shear stress and vorticity can not be time averaged with this function as they are found by post processing utilities. They are presented in instantaneous time frames or as time averages calculated from discrete time frames in a time span of $T = 50\frac{D}{U_\infty}$.

5.1 Convergence and quality of results

Two quantities are checked for mesh convergence, the average drag coefficient $\overline{C_x}$ and the root mean square of the cross flow force coefficient $C_{y,rms}$. Using the definition of force coefficients in Equation 2.4 and 2.5, F_x and F_y are the net forces in the x and y-direction on the total wetted surface of the foundations. The projected area A_{proj} is set to $D \times Height = D \times 2D = 2D^2$ for all the cases. CFD calculations are performed with three different computational meshes for each of the three foundations. The monopile meshes are called Monopile1, Monopile2, Monopile3, the meshes for the hexagonal GBF are called Hexagonal1, Hexagonal2, Hexagonal3 and the meshes for the circular GBF are called Circular1, Circular2 and Circular3. Figure 5.1 shows an example of a time plot of C_x and C_y, in this case for the Monopile2 mesh.

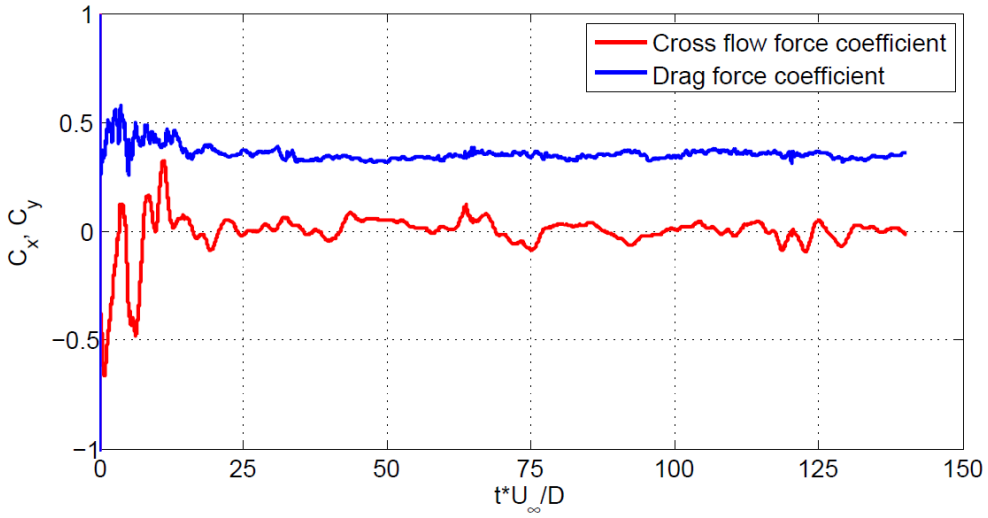

FIGURE 5.1: Time series of drag force and cross flow force coefficients for the Monopile2 computational mesh

A simple sine-like function is not expected for C_x and C_y because of the 3D effects involved, this will be discussed briefly in Section 5.2.1. They are however stable from around $t = 75D/U_\infty$, meaning that the difference in $\overline{C_x}$ and $C_{y,rms}$ calculated from the time spans $t = 75D/U_\infty - 115D/U_\infty$, $t = 85D/U_\infty - 125D/U_\infty$ and so on is negligible.

The long computational time of the analyses, coupled with the fact that the process of running analyses with different meshes is to a large degree iterative, has been a serious constraint on the the number of cells in the meshes. One non-dimensional second of simulation ($\bar{t} = t\frac{U_\infty}{D}$) has taken between 0.75 and 3 hours to calculate, depending on the case. At the most, $100D/U_\infty$ was needed before the solution was considered converged.

The computational time can be decreased if the time step is increased, but this will increase the Courant number. Although the Courant number is not a concern regarding the stability of the solution (considering that the present work uses implicit time integration), it is a concern regarding the physics of the solution. The average Courant number is kept low, in the range $0.0035 - 0.007$ in all the analyses, but the hexagonal GBF and circular GBF cases have maximum values up to 3 and 3.2, respectively, and this is the reason for not increasing the time step. These maximum values of the Courant number are very localized in time and space. Figure 5.2 illustrates this by showing a Courant number distribution scaled in three different ways, from $0.1 - 0.5$, $0.5 - 1$ and $1 - 2.16$. The last value is the maximum value in this particular case, which is the distribution of the Courant number on the top, bottom and foundation patches of the Circular2 mesh at an instantaneous $t = 133D/U_\infty$. All values equal to or below the minimum value on the axis are shown in blue and all values equal to or above the maximum value are

shown in red. The figure shows that few cells have Co above 0.5.

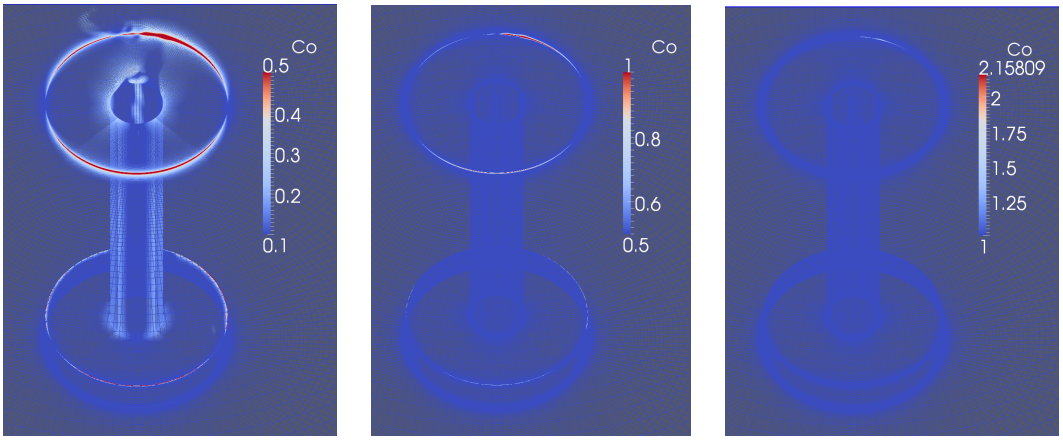

FIGURE 5.2: Courant number distribution on the top, bottom and foundation patches of the Circular2 mesh at $t = 133D/U_\infty$.

The y^+ values on the wall patches (bottom and foundations) are found to be reasonable. The range of average y^+ values (average on each patch separately) is found to be $28 < \overline{y^+} < 34$ for the monopile meshes, $26 < \overline{y^+} < 33$ for the hexagonal GBF meshes and $31 < \overline{y^+} < 38$ for the circular GBF meshes. In all analyses, 66 to 67 % of the volume in the computational domain is LES content, i.e. the Navier-Stokes equations are solved by the LES part of the SADDES model.

Monopile

$\overline{C_x}$ and $C_{y,rms}$ for the meshes Monopile1, Monopile2 and Monopile3 are calculated from time intervals of length $50\frac{D}{U_\infty}$, $65\frac{D}{U_\infty}$ and $80\frac{D}{U_\infty}$, respectively. Figure 5.3 shows $\overline{C_x}$ and $C_{y,rms}$ plotted against the number of cells.

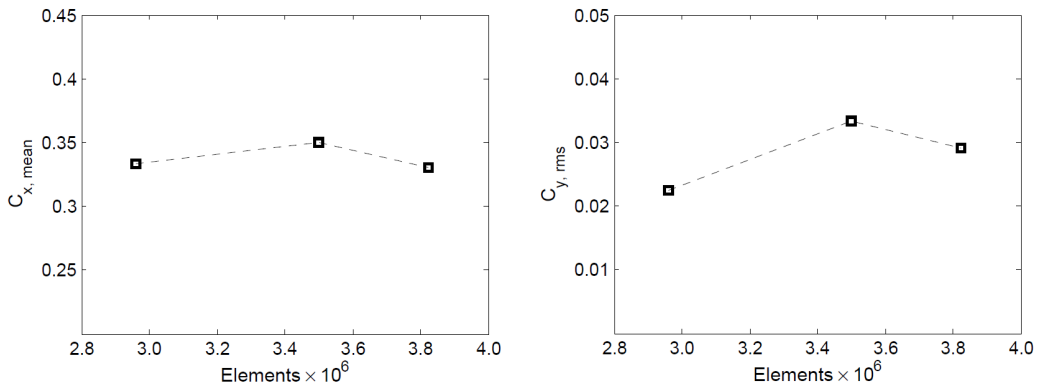

FIGURE 5.3: $C_{x,mean}$ and $C_{y,rms}$ for the monopile foundation plotted against number of cells.

Details of the monopile analyses are elaborated further in Table 5.1. $\overline{C_x}$ increases by 5 % when the number of cells are increased from 2.96 million to 3.5 million, and then decreases by 5.6 % from 3.5 million to 3.824 million cells. A similar behaviour is observed for $C_{y,rms}$ which increases by 48.7 % and then decreases by 12.6 % when the number of cells is increased from 2.96 million to 3.5 million cells and then 3.5 million to 3.824 million cells. Monopile1 and Monopile3 are constructed slightly different from Monopile2, with the cell density centred more towards the symmetryplane ($y/D = 0$) in order to capture the wake better. It seems likely that this is the reason for the shape of the curves in Figure 5.3. The cross flow force is more dependent than the drag force coefficient on vortex shedding, which is not a main focus in the present work. The cross flow force coefficient is also typically more unstable, meaning that a more thorough convergence analysis than that in the present work is needed before it is expected to converge properly.

TABLE 5.1: Mesh convergence study, monopile foundation

Case/Mesh	*Elements* $\times 10^6$	*Timestep* $\times D/U_\infty$	$\overline{C_x}$	$C_{y,rms}$	$\overline{C_y}/C_{y,rms}$
Monopile1	2.96	0.0008	0.333	0.0224	-0.1619
Monopile2	3.5	0.0008	0.3498	0.0333	-0.0379
Monopile3	3.824	0.0008	0.3301	0.0291	-0.1536

Figure 5.4 shows a normalized frequency spectrum for each of the monopile meshes based on the cross flow force coefficient. These are obtained by fourier analysis. The code for this analysis is found in Appendix B. The peak of the spectrum is located at a low Strouhal number in all three cases, 0.038 for Monopile1 and Monopile2 and 0.0095 for Monopile3. Most of the energy of the spectrum is consentrated below a Strouhal number 0.35 in all cases.

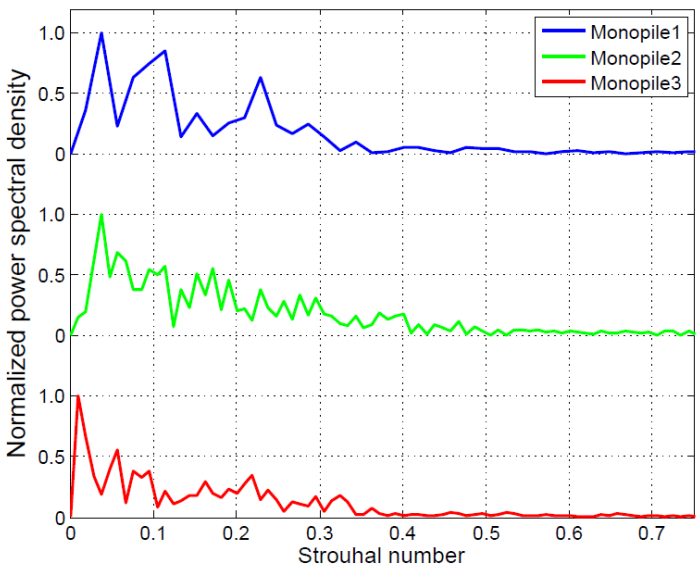

FIGURE 5.4: Normalized power density spectrum for the three monopile meshes

The low peak values of these spectra do not respesent the vortex shedding frequency. Figure 5.5 shows an excerpt of the drag force coefficient plotted against time for Monopile2. The shape of the curve shows that lower frequencies are present in addition to the frequency due to vortex shedding, or else the peaks marked in red would be along a horizontal line. With 24 peaks in a time interval of $20D/U_\infty$, the vortex shedding frequency should correspond to a Strouhal number around 0.6 (the frequency shown in the drag force coefficient plot is twice the vortex shedding frequency). This value is not captured well by the spectra in Figure 5.4, and this was also the case in a Fourier analysis with the drag force coefficient used instead of the cross flow force coefficient. Both analyses captured the lower frequencies in a similar manner. This topic will not be pursued further as the vortex shedding frequency is not a main concern in the present work.

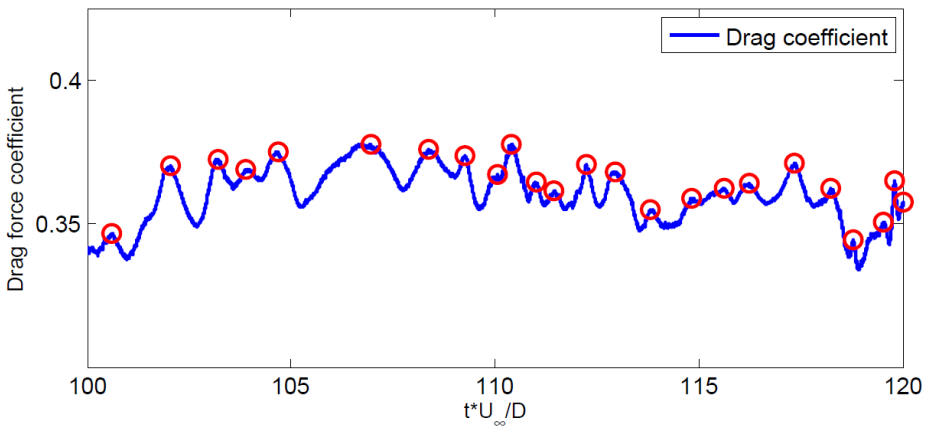

FIGURE 5.5: Time series of the drag force coefficient for the Monopile2 analysis

Hexagonal GBF

$\overline{C_x}$ and $C_{y,rms}$ are calculated on the basis of time spans of $50\frac{D}{U_\infty}$. Figure 5.6 and Table 5.2 show that $\overline{C_x}$ increases by 3.8 % from 3.1 millions cells to 4.123 million cells, and decreases by 2.3 % from 4.123 million cells to 4.996 million cells. $C_{y,rms}$ increases by 12 % and then decreases by 4.3 % for the same changes in cell number.

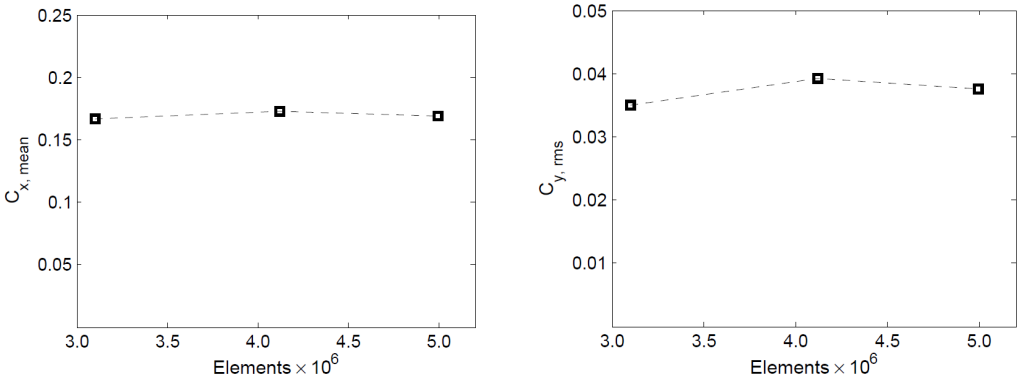

FIGURE 5.6: $C_{x,mean}$ and $C_{y,rms}$ for the hexagonal GBF plotted against number of cells.

TABLE 5.2: Mesh convergence study, hexagonal GBF

Case/Mesh	*Elements* $\times 10^6$	*Timestep* $\times D/U_\infty$	$\overline{C_x}$	$C_{y,rms}$	$\overline{C_y}/C_{y,rms}$
Hexagonal1	3.1	0.0006	0.1664	0.035	0.024
Hexagonal2	4.123	0.0006	0.1727	0.0392	0.0243
Hexagonal3	4.996	0.0006	0.1688	0.0375	-0.0683

A wide range of frequencies is present in the cross flow force, as shown in Figure 5.7. Most of the energy in the spectrum is located below St = 1.5 in all cases. Hexagonal1 has its peak at St = 0.636, Hexagonal2 at St = 0.852 and Hexagonal3 at St = 0.966, but all cases have energy peaks close to each others maximum values.

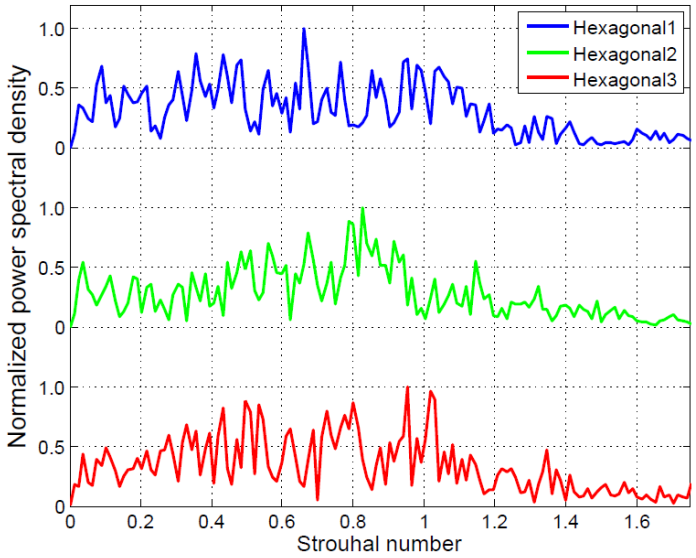

FIGURE 5.7: Normalized power density spectrum for the three hexagonal GBF meshes

Circular GBF

$\overline{C_x}$ and $C_{y,rms}$ are calculated on the basis of time spans of $50\frac{D}{U_\infty}$. Figure 5.8 and Table 5.3 show the details of the analysis with the three different computational meshes for the circular GBF. $\overline{C_x}$ increases by 3.9 % and then 5.0 % from Circular1 to Circular2 and Circular2 to Circular3. The same changes in cell number yields an increase of 14.6 % and 16.2 % in $C_{y,rms}$.

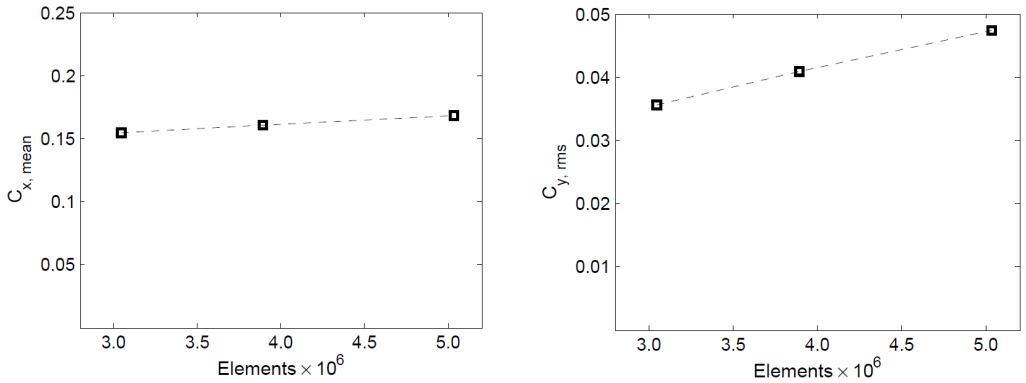

FIGURE 5.8: $C_{x,mean}$ and $C_{y,rms}$ for the circular GBF plotted against number of cells.

Case/Mesh	$Elements$ $\times 10^6$	$Timestep$ $\times D/U_\infty$	$\overline{C_x}$	$C_{y,rms}$	$\overline{C_y}/C_{y,rms}$
Circular1	3.044	0.0006	0.1542	0.0356	0.4822
Circular2	3.892	0.0006	0.1602	0.0408	-0.5445
Circular3	5.032	0.0006	0.1682	0.0474	0.5209

TABLE 5.3: Mesh convergence study, circular GBF

The $\overline{C_y}$ to $C_{y,rms}$ ratio is worth commenting on, as it reaches 48.2 %, -54.5 % and 52.1 % in case Circular1, Circular2 and Circular3, respectively. Although the wake behaves in a typical manner for flows with vortex shedding, it is shifted slightly to one of the sides resulting in a non-zero $\overline{C_y}$. Figures 5.9, 5.10 and 5.11 show the time-averaged pressure coefficient in the xy plane at $z/D = 0.1$ and $z/D = 0.5$ for the three different foundations. The pressure coefficient for the circular GBF at $z/D = 0.1$ stands out from the other figures by showing an asymmetry which is more severe in the wake (marked by an arrow) than upstream. This explains the non-zero $\overline{C_y}$. This issue is revisited in Section 5.5.2 as it affects seabed shear stresses.

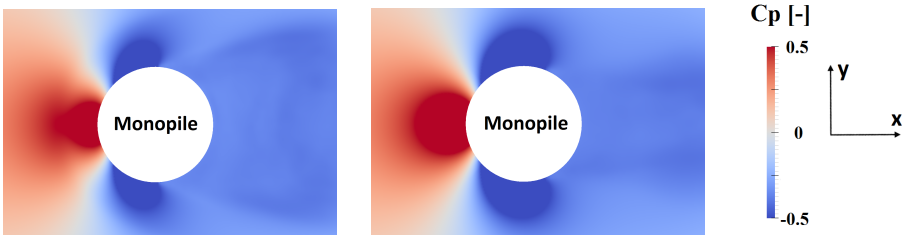

FIGURE 5.9: Time-averaged pressure coefficient in the xy plane at $z/D = 0.1$ (left) and $z/D = 0.5$ (right) for the monopile foundation

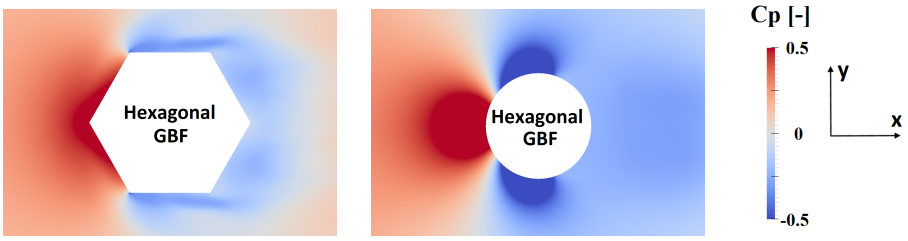

FIGURE 5.10: Time-averaged pressure coefficient in the xy plane at $z/D = 0.1$ (left) and $z/D = 0.5$ (right) for the hexagonal GBF

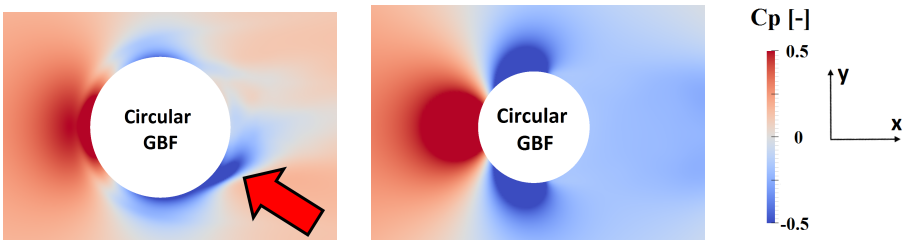

FIGURE 5.11: Time-averaged pressure coefficient in the xy plane at $z/D = 0.1$ (left) and $z/D = 0.5$ (right) for the circular GBF

Figure 5.12 shows the frequency spectrum based on a Fourier analysis of the cross flow force coefficient of the analyses of the circular gravity-based foundation. The energy of the spectra is concentrated below St = 1.5 in all cases. Maxima are found at St = 0.661, St = 0.827 and St = 0.954 for Circular1, Circular2 and Circular3, respectively. All cases have high energy peaks close to each others peak values. On a general note, it can be said that longer time series for the Fourier analyses would give more accurate energy spectra.

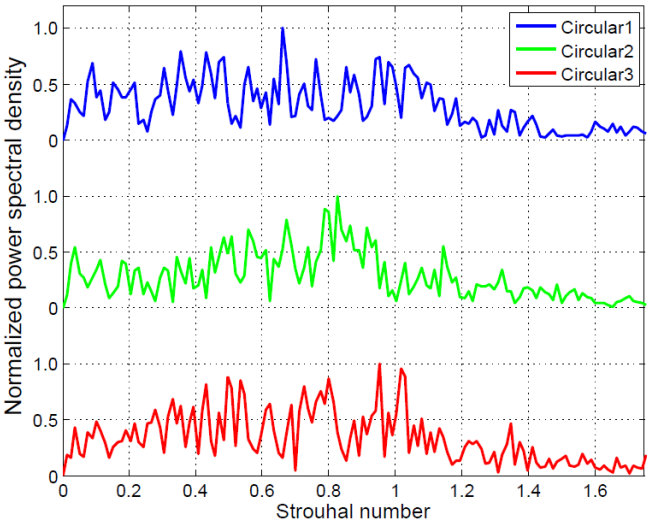

FIGURE 5.12: Normalized power density spectrum for the three circular GBF meshes

5.2 Vorticity

The structure of the flow is explored by 3D visualizations with the Q-criterion and by comparing components of vorticity in a plane close to the seabed at $z/D = 0.025$. These quantities are shown in instantaneous time frames.

5.2.1 Vortical structures, Q-criterion

The Q-criterion is a method of identifying coherent vortical structures (Jeong and Hussain, 1995). $Q = 5s^{-2}$ is used in all the figures.

Monopile

Figure 5.13 and 5.14 show the vortical structures of the flow around the monopile foundation three-dimensionally and from below (positive z-direction), respectively. A horseshoe vortex is seen clearly in front of the pile, which is mainly not in contact with the lee-wake vortices. This is because they are created by two different mechanisms, namely the separation on the seabed in front of the pile and the separation on the side of the foundation. The three-dimensionality of the flow can be seen by that many individual "packets" of vorticity exists up along the foundation. Figure 5.14 shows that the lee-wake vortices grow as they get farther downstream.

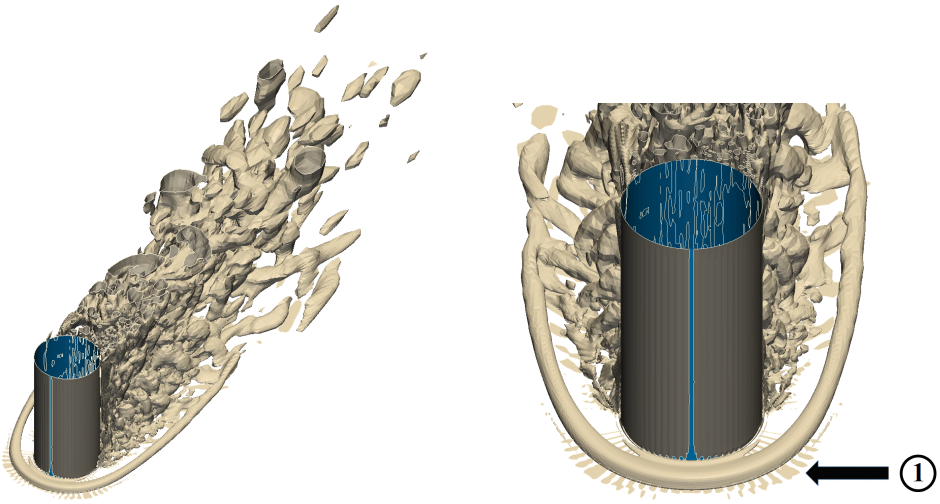

FIGURE 5.13: 3D view of instantaneous vortical structures around the monopile foundation at $t = 187.2\frac{D}{U_\infty}$

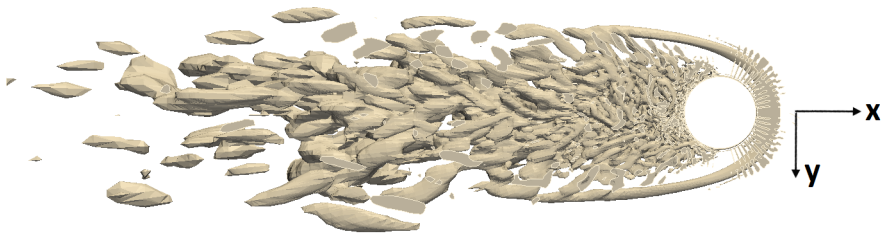

FIGURE 5.14: 2D view of instantaneous vortical structures around the monopile foundation at $t = 187.2\frac{D}{U_\infty}$, seen in the positive z-direction

Figure 5.14 also reveals small lines running out from the foundation, marked by (1), on the seabed on the front side. This is probably due to the mesh quality and not physical. They are however very small and do assumably not have any effect on the rest of the flow field.

Hexagonal GBF

Figure 5.15 and 5.16 show that the vortical structures around the hexagonal foundation are similar to those in the monopile case. However, the horseshoe vortex is broken into two parts, one over the seabed and one on the top of the bottom slab of the foundation, marked by (1) and (2) in Figure 5.15. This will be discussed further in Section 5.3. On the bottom slab, the separation point is located on the foremost edges of the foundation on the sides, as shown by (3) in Figure 5.16. The sharp edge in the front of foundation makes the size of the horseshoe small smaller in the symmetryplane ($y/D = 0$).

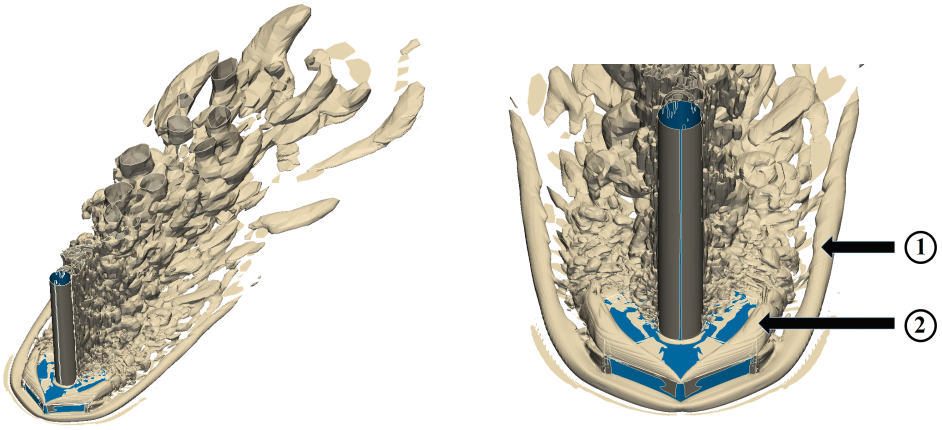

FIGURE 5.15: 3D view of instantaneous vortical structures around the hexagonal GBF at $t = 117.1\frac{D}{U_\infty}$

FIGURE 5.16: 2D view of instantaneous vortical structures around the hexagonal GBF at $t = 117.1\frac{D}{U_\infty}$, seen in the positive z-direction

Circular GBF

Figure 5.17 and 5.18 show that the horseshoe vortex is broken into three parts in the circular GBF case. One is on the top of the bottom slab (3), and two over the seabed (1 and 2) where vortex closest to the foundation (1) is the stronger one. This is observed for all the circular GBF meshes for all time steps after convergence. No physical explanation has been found for this behaviour. It is also seen that the bottom part of the vortical structures in the wake is shiftet slightly towards the y-direction, as discussed in Section 5.1.

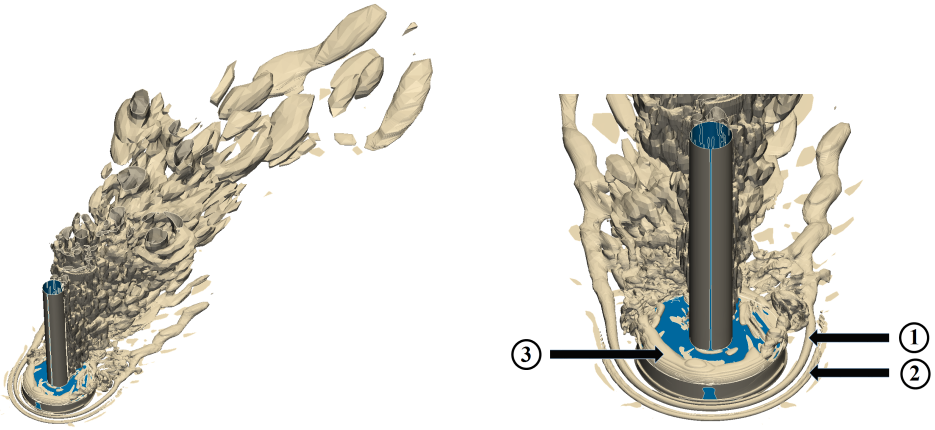

FIGURE 5.17: 3D view of instantaneous vortical structures around the circular GBF at $t = 109.8\frac{D}{U_\infty}$

FIGURE 5.18: 2D view of instantaneous vortical structures around the circular GBF at $t = 109.8\frac{D}{U_\infty}$, seen in the positive z-direction

5.2.2 Vorticity strength and components

The vorticity of the flow is calculated as the curl of the velocity field, namely

$$\vec{\omega} = \nabla \times \vec{U} \tag{5.1}$$

The curl has three components. A positive component of curl about an axis means that the rotation of the flow is clock-wise when looking in the positive axis direction. The vorticity is investigated in the $z/D = 0.025$ plane, looking in the negative z-direction. The x, y and z-components of vorticity are shown in figure 5.19, 5.20 and 5.21, respectively. The results for the three foundations are shown in each of the figures.

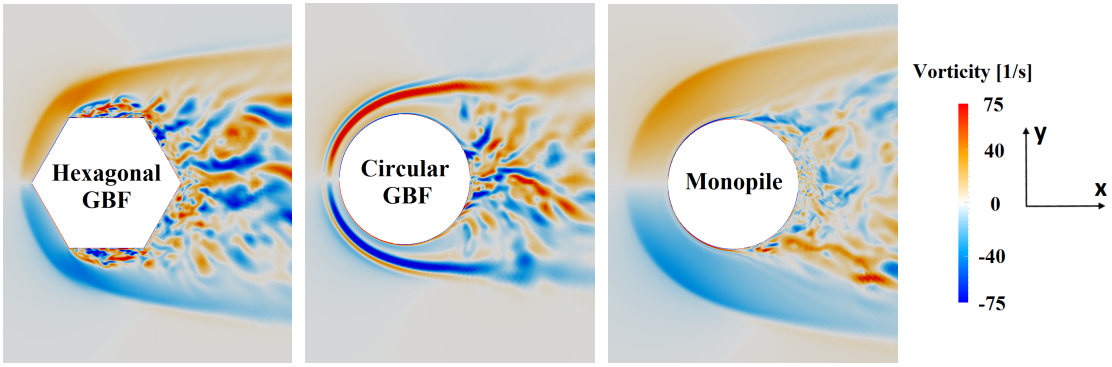

FIGURE 5.19: X-component of vorticity at $z/D = 0.025$. Left to right: hexagonal GBF ($t = 117.1\frac{D}{U_\infty}$), circular GBF ($t = 73.2\frac{D}{U_\infty}$), monopile ($t = 187.2\frac{D}{U_\infty}$)

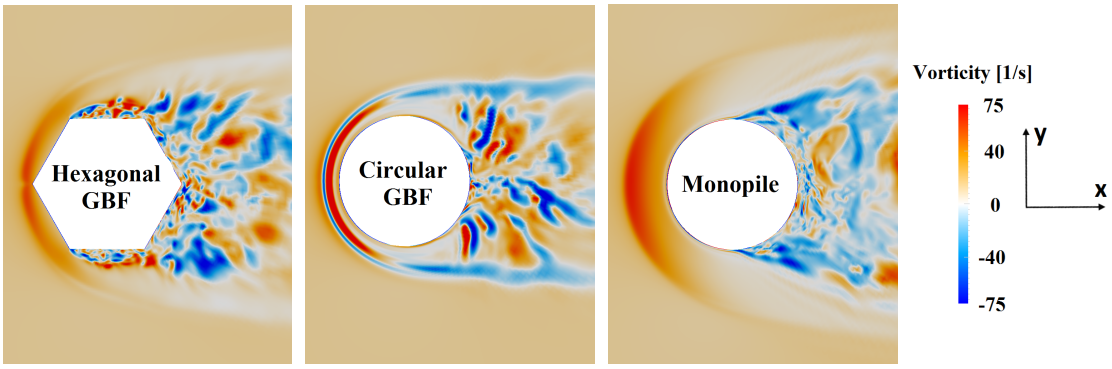

FIGURE 5.20: Y-component of vorticity at $z/D = 0.025$. Left to right: hexagonal GBF ($t = 117.1\frac{D}{U_\infty}$), circular GBF ($t = 73.2\frac{D}{U_\infty}$), monopile ($t = 187.2\frac{D}{U_\infty}$)

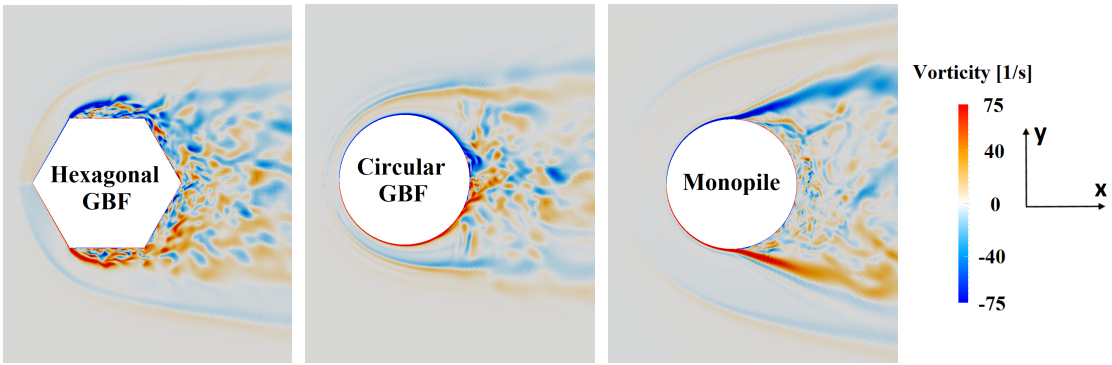

FIGURE 5.21: Z-component of vorticity at $z/D = 0.025$. Left to right: hexagonal GBF ($t = 117.1\frac{D}{U_\infty}$), circular GBF ($t = 73.2\frac{D}{U_\infty}$), monopile ($t = 187.2\frac{D}{U_\infty}$)

It is seen that the largest contribution to vorticity in front of the foundation is the y-component, while over and under it is the x-component (45 to 90 or -45 to -90 degrees from the separation point, measured from the negative x-axis). This indicates that the vortices are formed in front of the foundation and travel downstream along a horseshoe shaped trajectory. The z-component contributes little to the horseshoe vortex.

5.3 Velocities

Velocities are shown in the xz plane at $y/D = 0$ and as velocity profiles along $y/D = 0$ in the following section to show the effect of the foundation geometries on the velocity field.

5.3.1 Downflow and backflow

Downflow refers to negative vertical velocity and backflow to negative horizontal velocity. The z and x components of velocity, w and u, are shown in the xz plane at $y/D = 0$ in Figure 5.22 and 5.23. Figure 5.22 reveals that significant downflow is present in the flow field in front of all the foundations. The downflow in front of the monopile, marked by (1), covers an area all the way down to the seabed, with a maximum value at 30 % of the inflow velocity close to the intersection of the seabed and the foundation. In the case of the gravity-based foundations, the downflow that developes in front of the cylindrical shaft, marked by (2), is stopped from reaching the seabed by the top of the bottom slab. Areas of downflow develop near the seabed in front of bottom slab of both the gravity-based foundation, as marked by (3). Large downflow velocities exist in these areas (29 % and 50 % of the inflow velocity for hexagonal and circular GBF, respectively), but they are highly local.

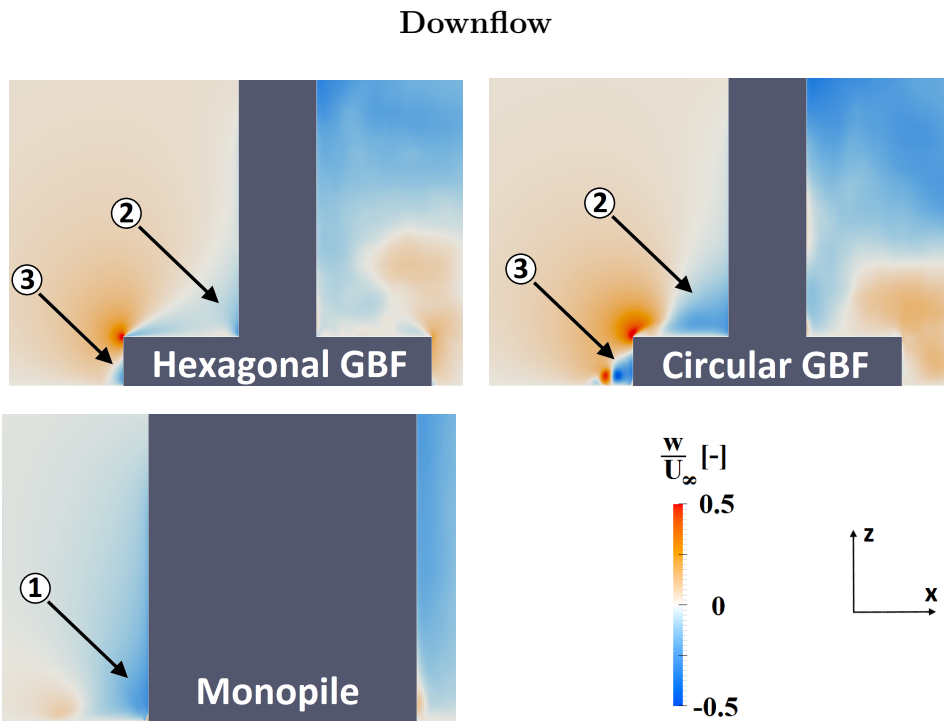

FIGURE 5.22: Vertical velocity w in the $y/D = 0$ plane. Left to right: hexagonal GBF, circular GBF, monopile. Velocities are time-averaged.

The downflow in front of the foundations will cause a backflow over the bottom slab and the seabed due to conservation of mass. It is seen in Figure 5.23 that the monopile foundation, which has a significant area of downflow in front of it, has a significant area of backflow near the seabed. The gravity-based foundations have smaller areas of backflow near the seabed. The maximum backflow values are 42 %, 58 % and 73 % for the monopile, hexagonal GBF and circular GBF, respectively. As with the downflow the large backflow velocities for the gravity-based foundations are highly local. It can be said that the geometries of the gravity-based foundations limit the downflow and backflow near the seabed.

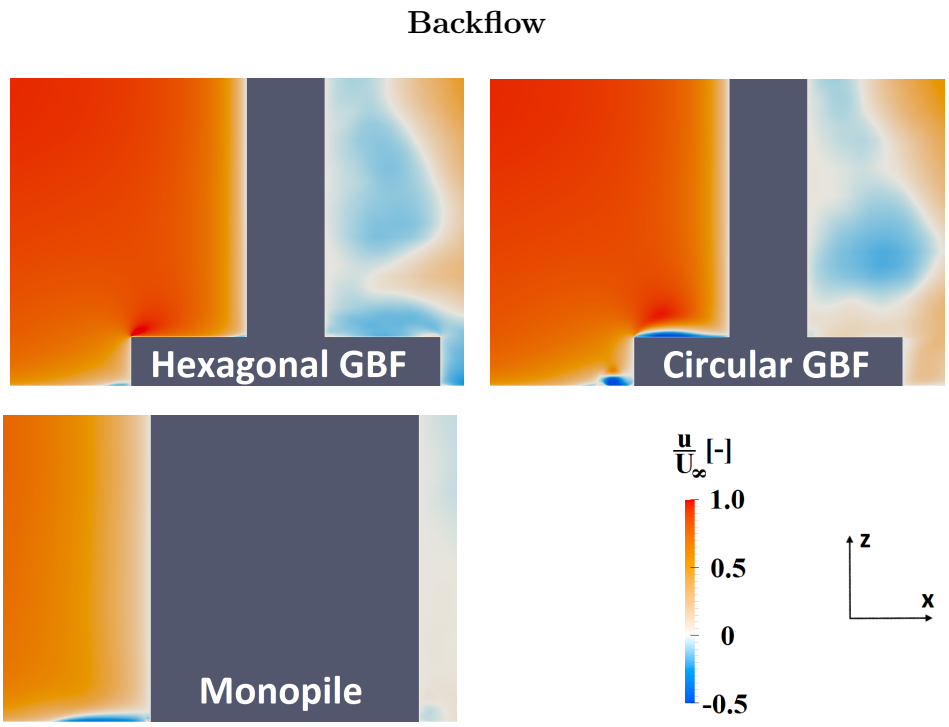

FIGURE 5.23: Horizontal velocity u in the $y/D = 0$ plane. Left to right: hexagonal GBF, circular GBF, monopile. Velocities are time-averaged.

5.3.2 Velocity profiles

Profiles of horisontal velocity are shown at six values of x/D along the line $y/D = 0$ in Figure 5.24, 5.25 and 5.26 for the three foundations. For all the cases, the profiles at $x/D = -9.0, -7.0$ and -5.0 are almost identical, except for very near the seabed. This will be discussed further in Section 5.5 as it is relevant for the discussion on bed shear stress.

As x/D gets larger, i.e. the profile is obtained closer to the foundation, the fluid is slowed down because of the pressure gradient imposed by the geometry. Taking the profiles at $x/D = -0.6$, it is seen that the slowing down effect is much stronger in the monopile case than in the others,

with an average horisontal velocity of 33 % of the free stream velocity. The corresponding velocity is 83 % for both of the gravity-based foundations. This is because of the larger volume of the monopile foundation.

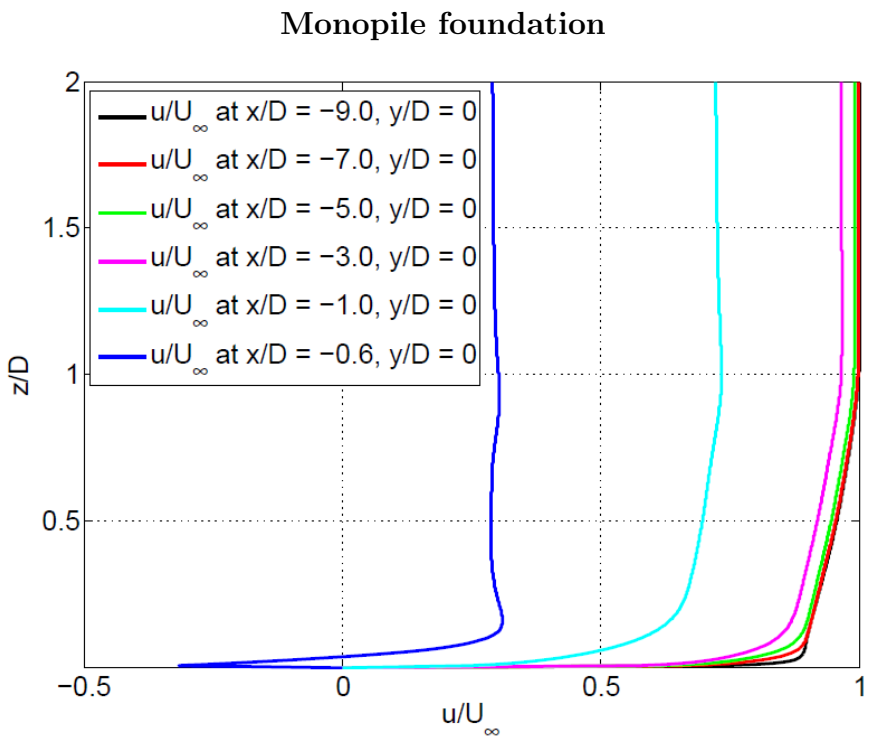

FIGURE 5.24: Profiles of velocity in the x-direction for the monopile foundation. Velocities are time-averaged.

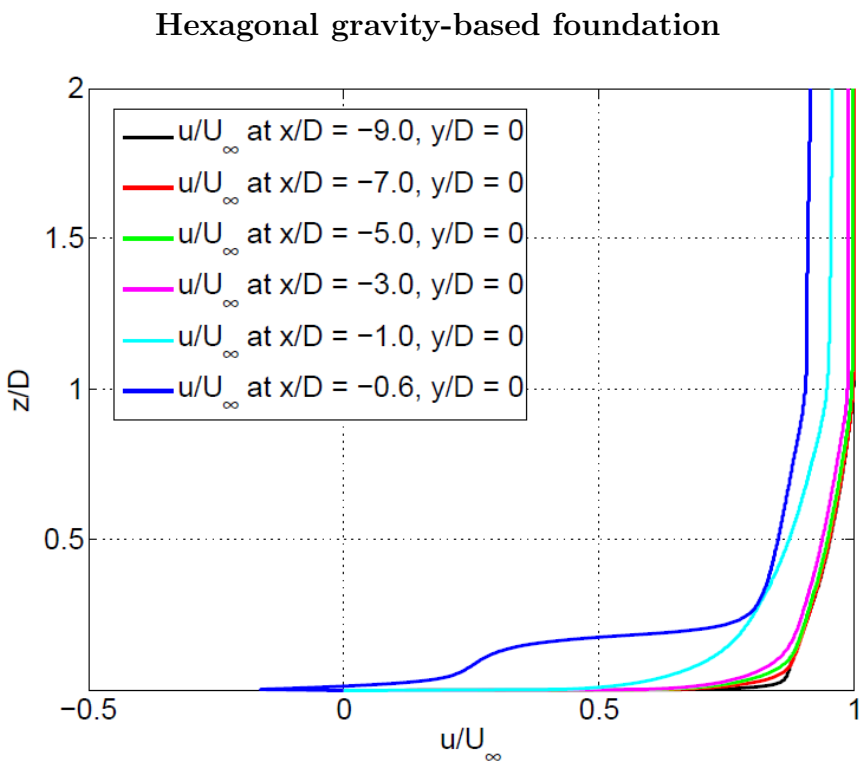

FIGURE 5.25: Profiles of velocity in the x-direction for the hexagonal GBF. Velocities are time-averaged.

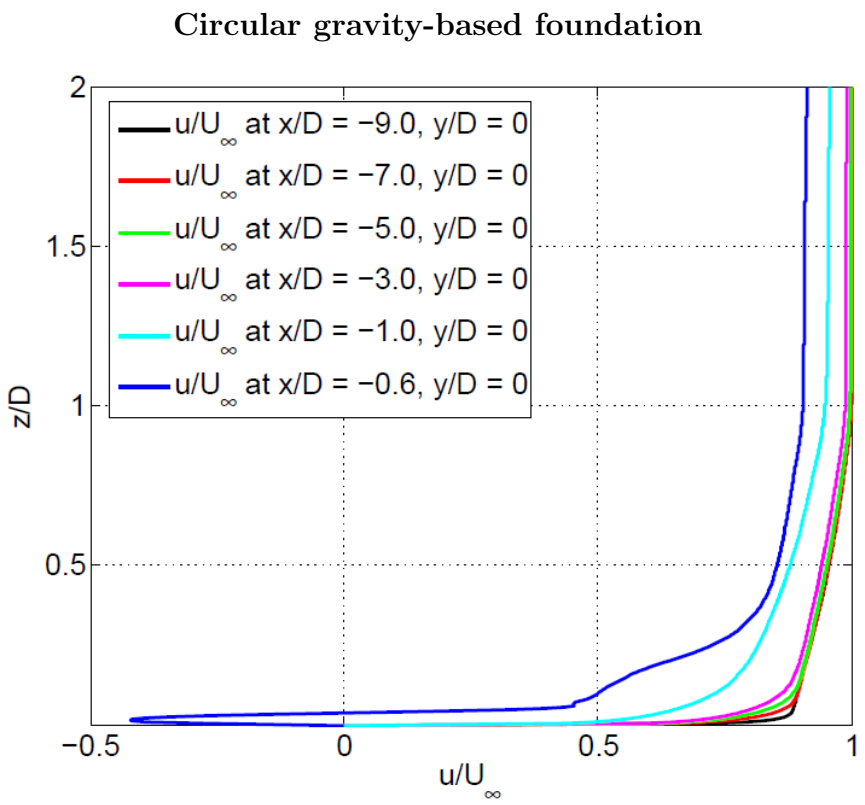

FIGURE 5.26: Profiles of velocity in the x-direction for the circular GBF. Velocities are time-averaged.

5.4 Pressure

In this section the pressure distributions in the present study are explored by isolines and isosurfaces. Comparisons with published data are made for the monopile foundation. The pressure is expressed by pressure coefficients throughout the section.

5.4.1 Isolines and isosurfaces

The isolines of the time-averaged pressure coefficient in the xz plane at $y/D = 0$ are shown in Figure 5.27, 5.28 and 5.29. Following the innermost isolines on the front side of the foundations from the top and downwards, it is seen that their main feature is that they curve inwards on to the foundations. The effect is stronger for the monopile foundation than for the other foundations. This effect is due to the retardation of flow in front of the foundations. As the deacceleration is larger higher up where the initial velocity in the velocity profile is higher, a positive vertical pressure gradient is present. More specifically, $\frac{dp}{dz} > 0$ close to the foundation surface in front of the foundations. This causes the downflow discussed in Section 5.3.1.

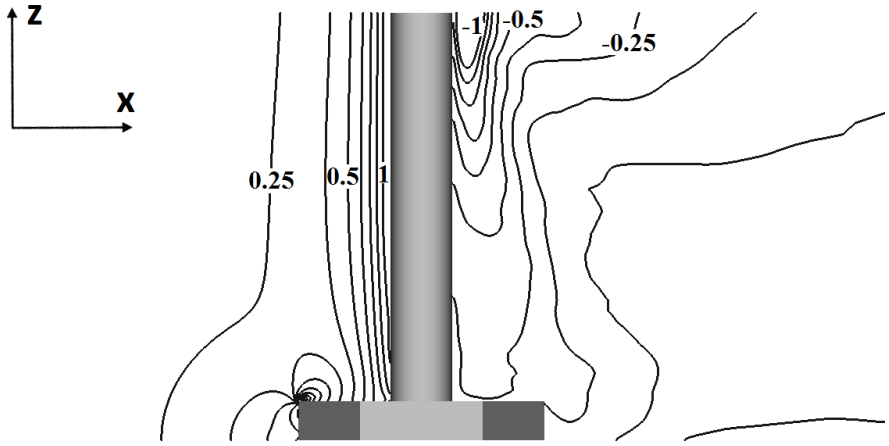

FIGURE 5.27: Pressure coefficient isolines in the xz plane at $y/D = 0$ for the hexagonal GBF. The pressure is time-averaged

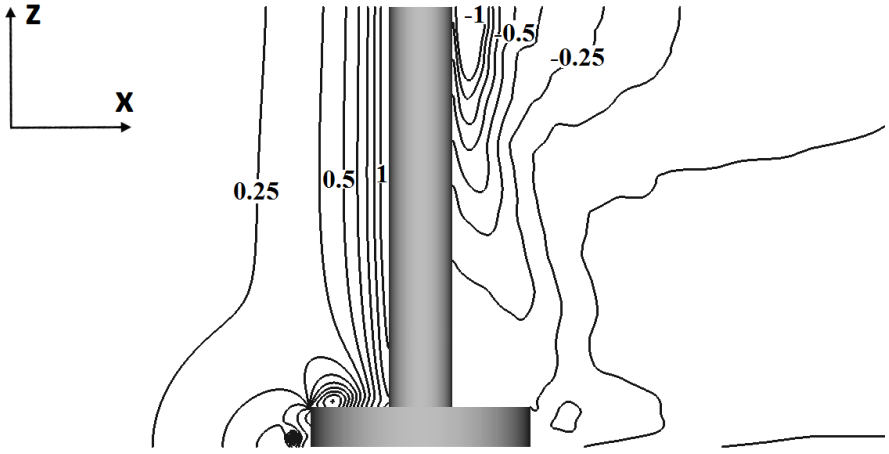

FIGURE 5.28: Pressure coefficient isolines in the xz plane at $y/D = 0$ for the circular GBF. The pressure is time-averaged

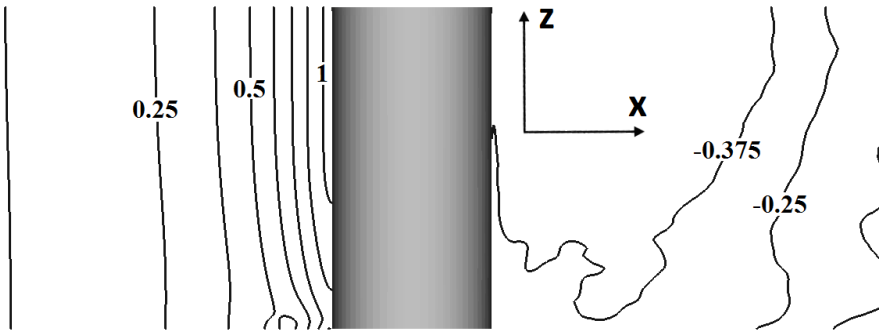

FIGURE 5.29: Pressure coefficient isolines in the xz plane at $y/D = 0$ for the monopile foundation. The pressure is time-averaged

Time-averaged pressure is shown as isosurfaces of C_p in Figure 5.30, 5.31 and 5.32. 4 isosurfaces are shown, $C_p = 0.25$, $C_p = 0.5$, $C_p = 0.75$ and $C_p = 1$. The left figure shows $C_p = 0.25$ as the outermost surface, in blue. The next show 3 surfaces, with $C_p = 0.5$ as the outermost shown in light blue. The vertical pressure gradient in front of the foundations can be seen from the shape of the isosurface for $C_p = 0.5$. It is seen that the isosurfaces encloses larger volumes in front of the monopile foundation than in front of the gravity-based foundations. This is due to its geometry and fits well with the discussion on velocity profiles in Section 5.3.2.

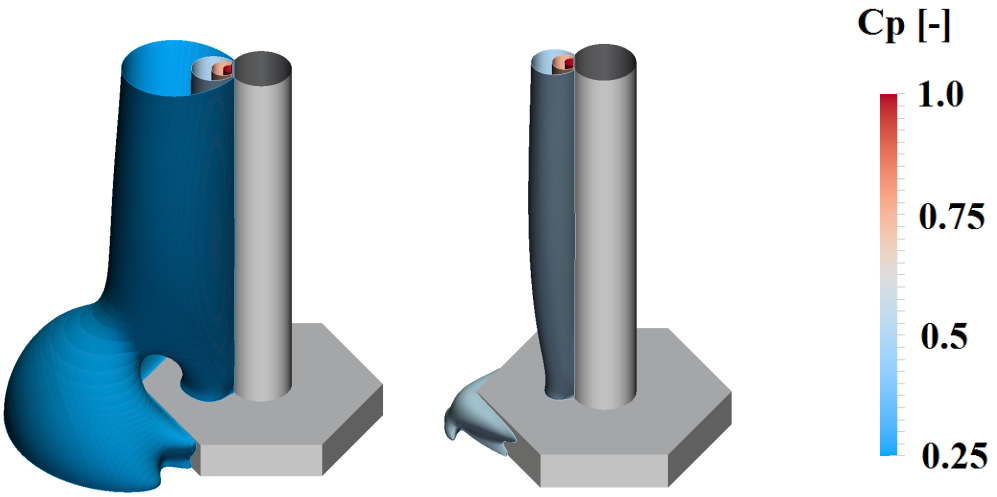

FIGURE 5.30: Pressure coefficient isosurfaces for the hexagonal GBF. The pressure is time-averaged

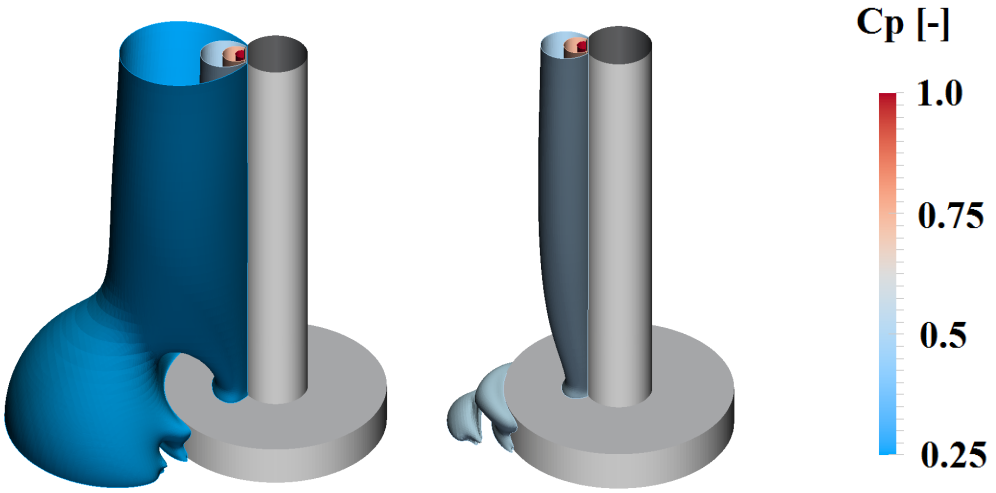

FIGURE 5.31: Pressure coefficient isosurfaces for the circular GBF. The pressure is time-averaged

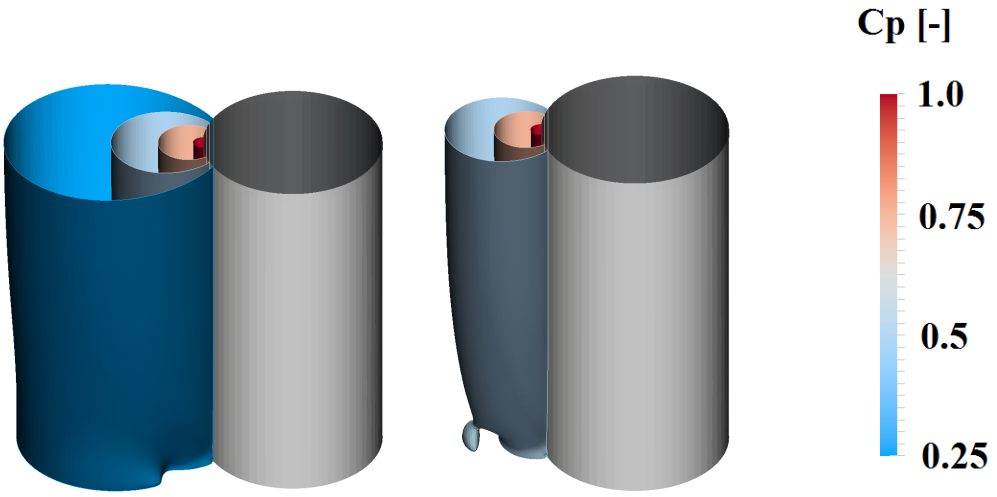

FIGURE 5.32: Pressure coefficient isosurfaces for the monopile foundation. The pressure is time-averaged

5.4.2 Comparisons with published data

The pressure coefficient on the seabed along the line $y/D = 0$, $z/D = 0$, and on the monopile surface along $x/D = -0.5$, $y/D = 0$ is compared to published data by Roulund et al. and Dargahi. The numerical study by Roulund et al. uses $Re = 1.5 \times 10^4$ and $\delta/D = 4$, and the experiemental by Dargahi uses $Re = 3.9 * 10^4$ with $\delta/D = 4/3$. Both cases has a smooth, rigid bed and a Reynolds number based on the mean flow velocity. The results are normalized. The results from the present study compare well with the pressure coefficient shown in Figure 5.33. The local maximum of the present study where $C_p = 0.6$ marks the separation point. It is slightly delayed and more pronounced in the present study.

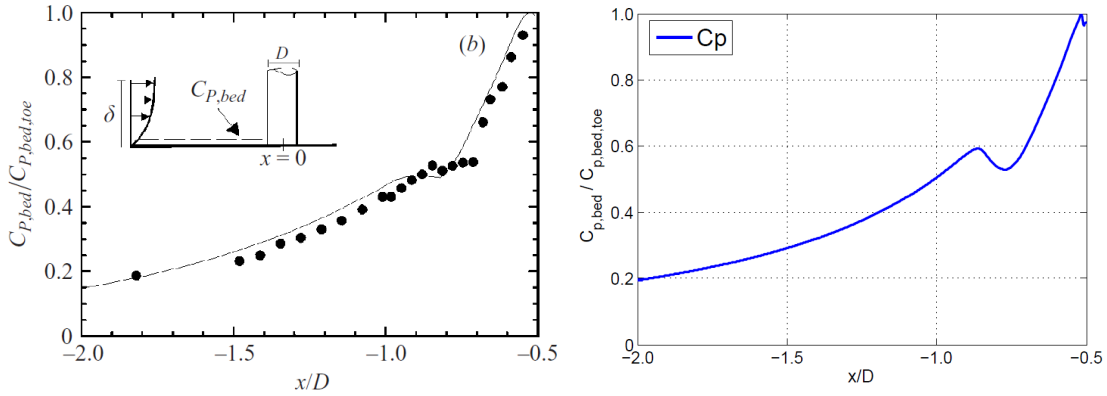

FIGURE 5.33: Normalized pressure coefficient along $y/D = 0, z/D = 0$. Left: Experimental data by (Dargahi, 1989) • and numerical data by (Roulund et al., 2005) — . Right: Present study

The pressure coefficient along the pile surface shows a similar behaviour as the published data, as shown in Figure 5.34. It must be commented that while C_p is equal to the published data at $x/D = -0.5, y/D = 0, z/D = 0$ in Figure 5.33, it is not in Figure 5.34 in the exact same point. This is due to the way the results are normalized so that the maximum value is 1 in all figures. Figure 5.34 reveals that the pressure coefficient in the present study is larger that the published data at this point. This is expected because of the larger Reynolds number, which will give a smaller horseshoe vortex that will be reflected in a smaller vertical pressure gradient near the seabed in front of the pile. The pressure coefficient in the present work has a small local minimum very close to the seabed, unlike the published data. This is consistent with the lines of vorticity described in Section 5.2.1. This behaviour is not physical.

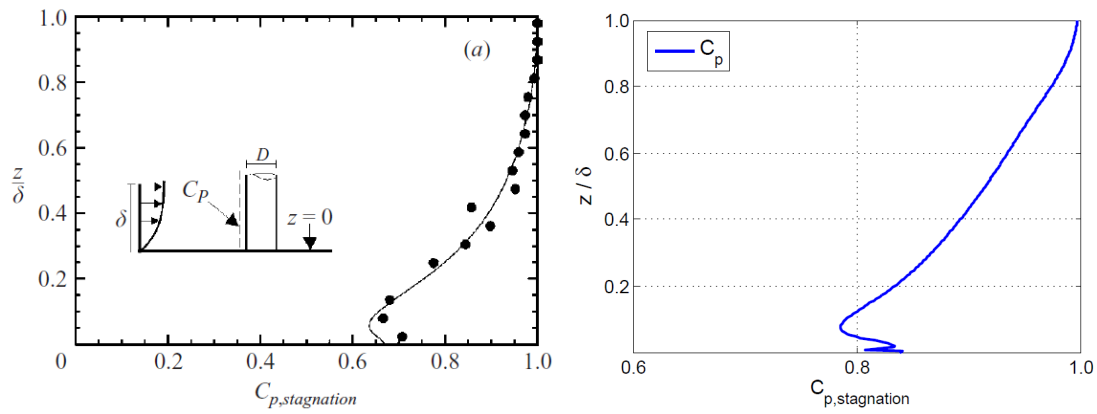

FIGURE 5.34: Normalized pressure coefficient along $x/D = -0.5, y/D = 0$. Left: Experimental data by (Dargahi, 1989) • and numerical data by (Roulund et al., 2005) — . Right: Present study

5.5 Bed shear stress

Bed shear stresses are found with the wallShearStressLES post processing utility in OpenFOAM. The bed shear stress is expressed by a shear stress amplification factor or a shear stress coefficient throughout the section.

5.5.1 Normalization and time variation

The velocity profile used as a boundary condition at the inlet is an approximation. Figure 5.35 shows the x-component of the shear stress coefficient for each foundation along the line $y/D = 9, z/D = 0$, where the bed shear stress is undisturbed by the presence of the foundations (the y and z-components are zero in an undisturbed flow). The shear stress decreases quickly away from the inlet before it becomes more stable from around $x/D = -5$. The minimum value of the shear stress coefficient along this line in the circular GBF case, 0.00198, is assumed to be the best approximation of the undisturbed shear stress as this geometry changes the flow field the least out to the sides. It is noted that the shear stress coefficient for the monopile foundation decreases throughout the range $-10 < x/D < 10$, but it remains close to 0.00198 from around $x/D = -5$.

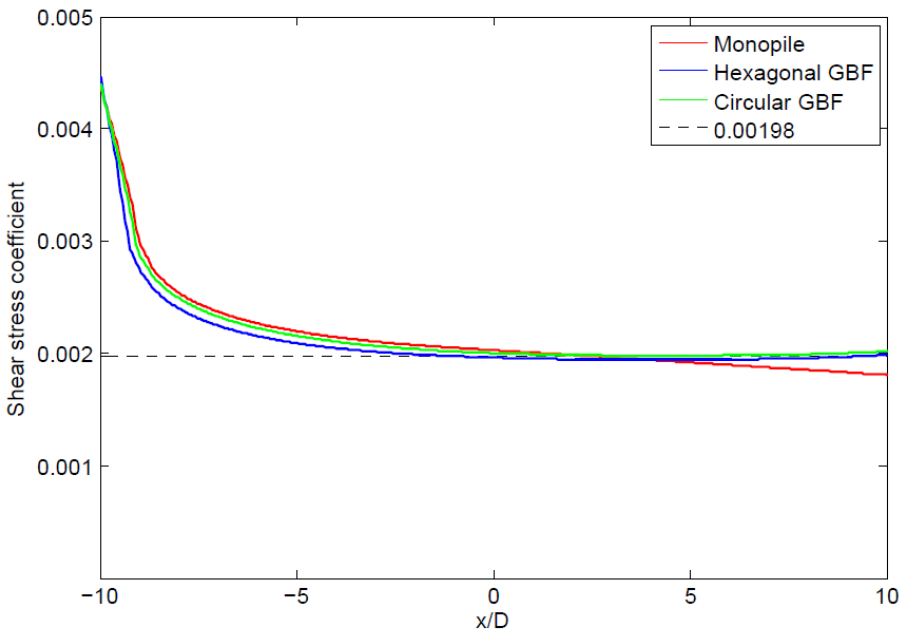

FIGURE 5.35: Bed shear stresses along the line $y/D = 9$, $z/D = 0$

Turning to Figure 5.36, we see the x-component of the shear stress coefficient along $y/D = 0$, $z/D = 0$ in the range $-10 < x/D < -0.5$, i.e. upstream. It is seen that the undisturbed shear stress value is reached at around $x/D = -6$. In Section 5.3.2 it was concluded that the velocity

profiles do not change from $x/D = -9$ to $x/D = -5$ except for near the seabed. This means that the velocity gradient at the seabed, thus the bed shear stress, is adjusted to the undisturbed bed shear stress before the presence of the foundation has any significant effect on the flow. Based on these arguments it is reasonable to use 0.00198 as the undisturbed shear stress coefficient which is used to calculate the bed shear stress amplification factor.

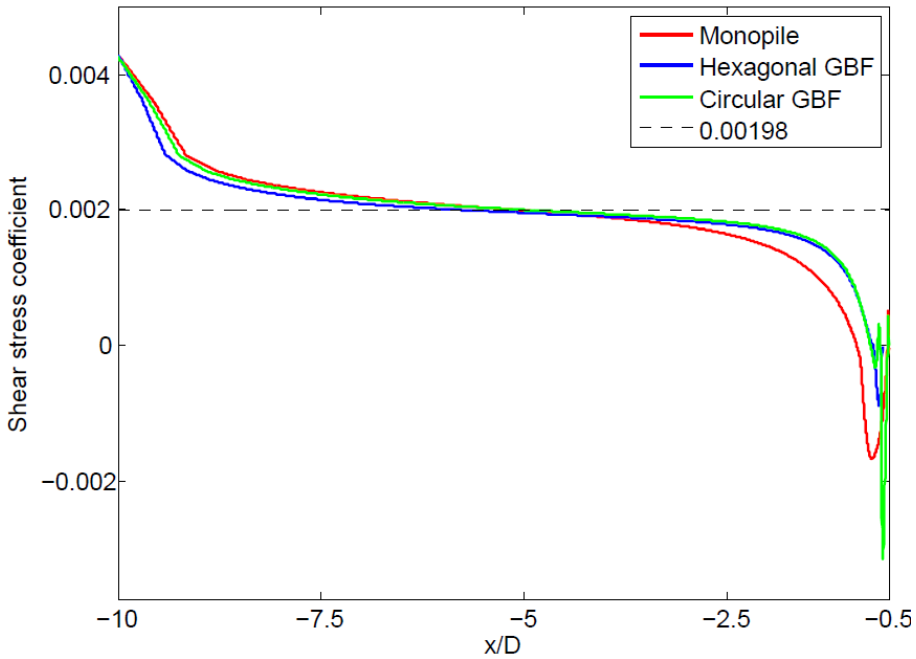

FIGURE 5.36: Bed shear stresses along the symmetryline, y = 0, z = 0

Time averages are calculated based on 20 evenly distributed time steps in the time span $T = 50\frac{D}{U_\infty}$. This is considered sufficient for obtaining accurate average results, as the shear stresses in the areas outside the wake show very little time variation. The shear stresses on the seabed in the wake region show more time variation, but these stresses are not as interesting as they are of around the same magnitude as τ_∞, the shear stress far away from the foundation. The time variation is illustrated by Figure 5.37 which shows three different time frames of the shear stress coefficient (its magnitude) for the monopile foundation. The bed shear stress changes the most in the wake area, as seen by the changing patterns. The maximum amplification factor in these time frames is around 5, which is larger than the time averaged maximum of 4.89.

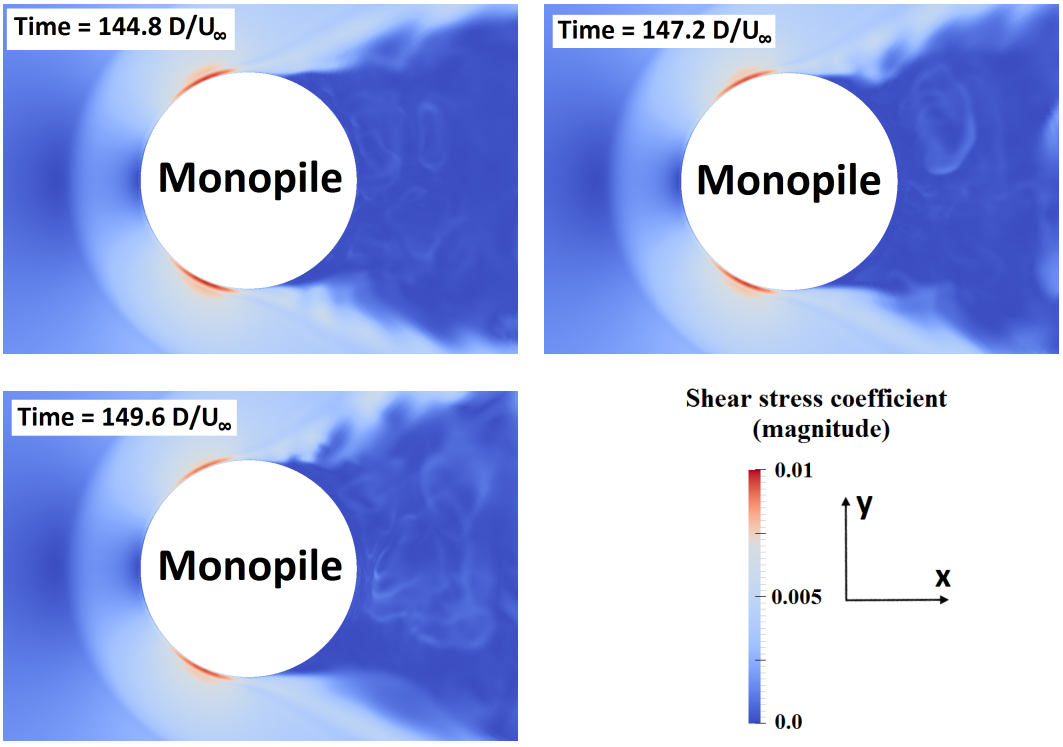

FIGURE 5.37: Instantaneous time frames of the shear stress coefficient distribution on the seabed around the monopile foundation

5.5.2 Results and comparisons with published data

Shear stress along the symmetryline

The line in the x-direction at $y/D = 0$, $z/D = 0$ will be referred to as the symmetryline throughout this section. The results obtained numerically and experimentally by Roulund et al. are used as a comparison to the present work and are shown in Figure 5.38. The numerical analysis used $Re = 1.5 \times 10^4$, $\delta/D = 4$ and a smooth, rigid bed. The experiental results were obtained for $Re = 1.7 \times 10^5$, $\delta/D = 1$ and a smooth, rigid bed. The Reynolds number is in both cases based on the mean flow velocity of a logarithmic velocity profile. Based on the arguments in Section 4.2.2, these results are comparable to the present work in terms of the boundary layer size.

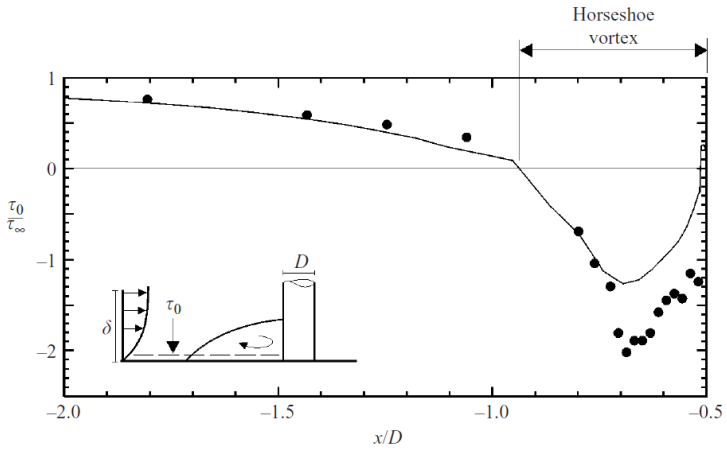

FIGURE 5.38: Bed shear stress amplification factor along $y/D = 0$, $z/D = 0$ (Roulund et al., 2005). • Experiment, — Numerical model

The bed shear stress amplification is based on the x-component of shear stress, the other components are negligable in this region. Since the shear stress depends on the velocity gradient on the seabed, the separation point along the symmetryline is where the shear stress is zero. This occurs at approximately $x/D = -0.95$. The negative values beyond this point are due to backflow. The numerical model underpredicts the shear stress in the range $-0.75 < x/D < -0.5$ (Roulund et al., 2005).

Figure 5.39 and 5.40 show the influence of the Reynolds number, based on the free stream velocity, on the separation point and the maximum shear stress amplification under the horseshoe vortex along the upstream symmetryline from the study by Roulund et al. The results are presented here because they are relevant to the discussion on bed shear stresses. Note that the Reynolds number based the mean velocity in Figure 5.38 corresponds to a larger Reynolds number based on free stream velocity. It is seen that an increase in the Reynolds number decreases the maximum shear stress amplification at $Re > 500$. It has a similar effect on the separation distance, before it stabilizes at slightly less than 1 from $Re = 10^5$.

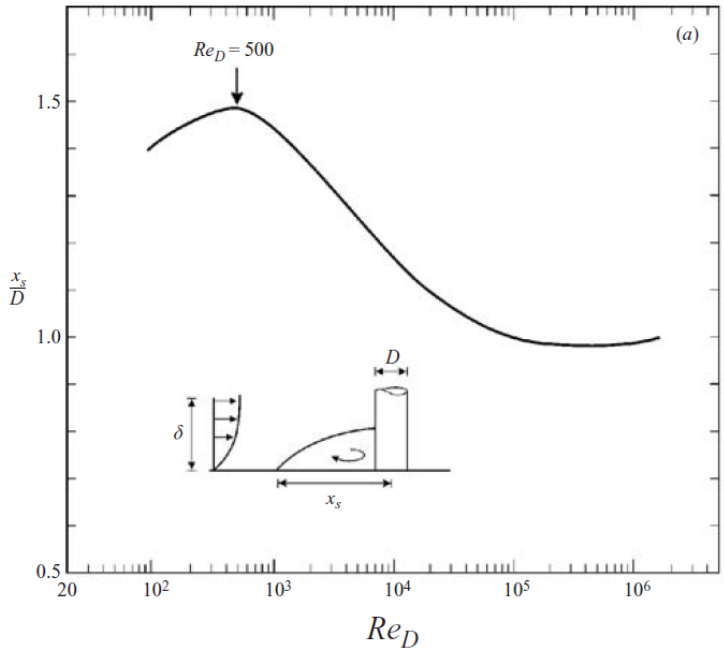

FIGURE 5.39: Influence of the Reynolds number on the separation distance x_s/D. $\delta/D = 8$, smooth, rigid bed. Re is based on the free stream velocity (Roulund et al., 2005).

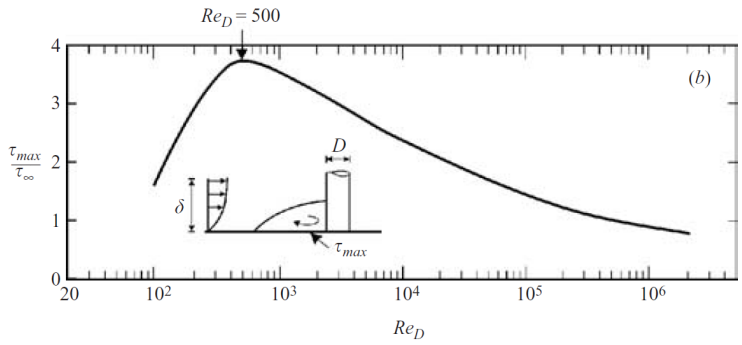

FIGURE 5.40: Influence of the Reynolds number on the maximum shear stress amplification under the horseshoe vortex along the upstream symmetryline. $\delta/D = 8$, smooth, rigid bed. Re is based on the free stream velocity (Roulund et al., 2005).

Figures 5.41, 5.42 and 5.43 show the results obtained in the present study. A delayed separation and a smaller horseshoe vortex strength ($\frac{\tau}{\tau_\infty}min$ is larger) is expected as the Reynolds number is larger than in the results in Figure 5.38. It can not be ruled out that the decrease in horseshoe vortex strength is partly due to underprediction by the numerical model. This is not a big issue as the main focus of the present study is comparisons between the different foundations.

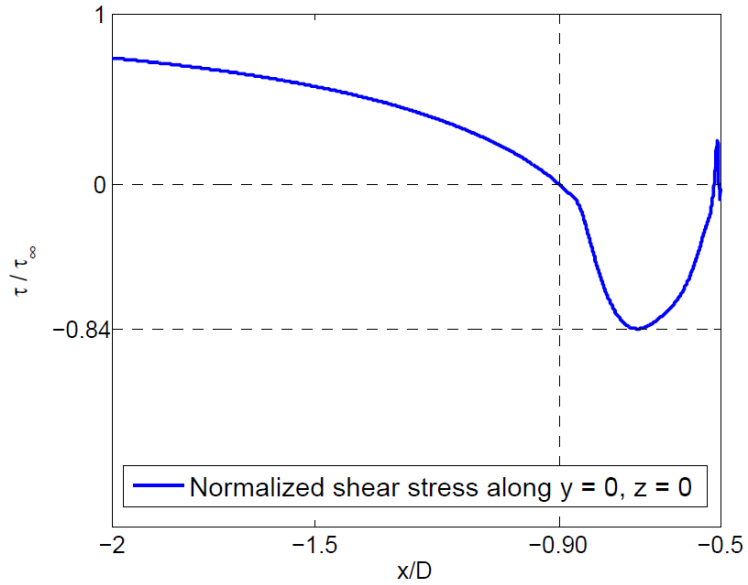

FIGURE 5.41: Shear stress amplification along the symmetryline, monopile foundation

The results for the hexagonal GBF (Figure 5.42) show a significantly delayed separation point and reduction in horseshoe vortex strength. It must be noted the sharp front edge on this foundation, which reduces the horseshoe vortex strength, is located on the symmetryline. It is also worth noting that the largest amplification factors in the bed shear stress distributions around the foundations are not found along the symmetryline.

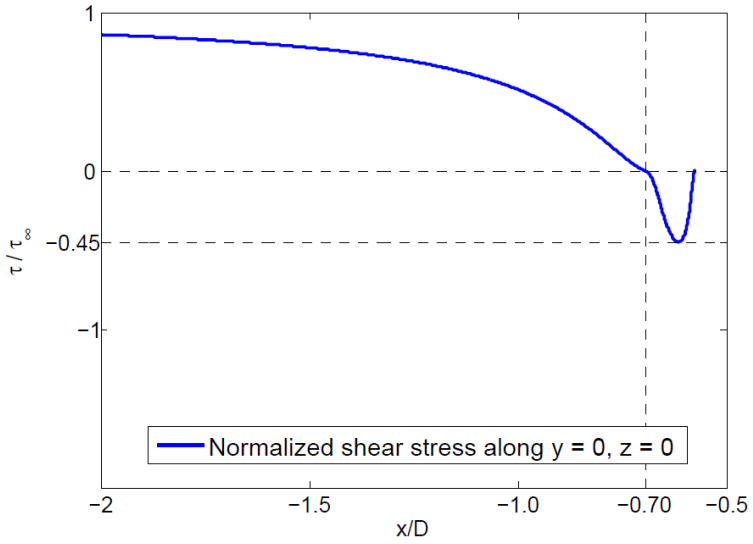

FIGURE 5.42: Shear stress amplification along the symmetryline, hexagonal GBF

Figure 5.43 is consistent with the vortical structures around the circular GBF in Section 5.2.1, which shows that the horseshoe vortex is broken up into two part on the seabed in front of the foundation. The figure shows that the innermost vortex is much stronger than the outer. No explanation has been found for this behaviour.

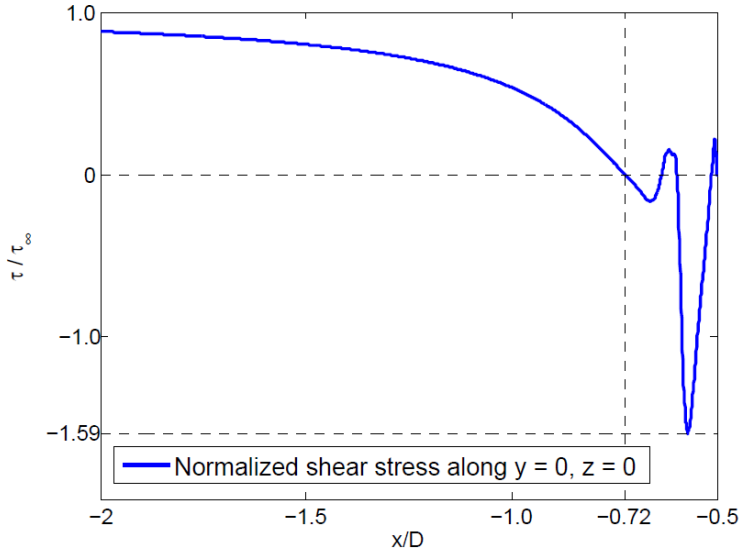

FIGURE 5.43: Shear stress amplification along the symmetryline, circular GBF

TABLE 5.4: Comparison of shear stress amplification, separation distance and horseshoe vortex size between the different foundations

Foundation	$\tau/\tau_\infty min$	x_s/D	HSV size / D
Monopile	-0.84	-0.90	0.40
Hexagonal GBF	-0.45	-0.70	0.125
Circular GBF	-1.59	-0.72	0.22

Table 5.4 summarizes the results for $\tau/\tau_\infty min$, x_s/D and $HSVsize/D$ (The front edge of the hexagonal foundation is located at $x/D = -0.575$, while the front of the two other foundations starts at $x/D = -0.5$).

Shear stress distribution on seabed

Roulund et al. studied the bed shear stress distribution around a monopile at several Reynolds numbers (based on mean flow velocity) by using steady-state simulations (Roulund et al., 2005). The results are presented here because they are relevant to the discussion on bed shear stress distributions. The results of these analyses are expressed by the shear stress magnitude normalized by the far field shear stress τ_∞ in Figure 5.44, 5.45, 5.46 and 5.47. The size and strength of the horseshoe vortex and the maximum amplification factor does not change significantly when the Reynolds number is increased from 200 to 2000. When it is increased further these quantities decrease. It is worth commenting that although the maximum amplification factor decreases when the Reynolds number is increased, the actual shear stress value measured in Pascal will increase. The large amplification at $45 < \phi < 70$, where ϕ is the angle measured from the negative x-axis, is due to the combination of the presence of the horseshoe vortex and the contraction of the flow (Roulund et al., 2005). The distributions are expressed by isolines.

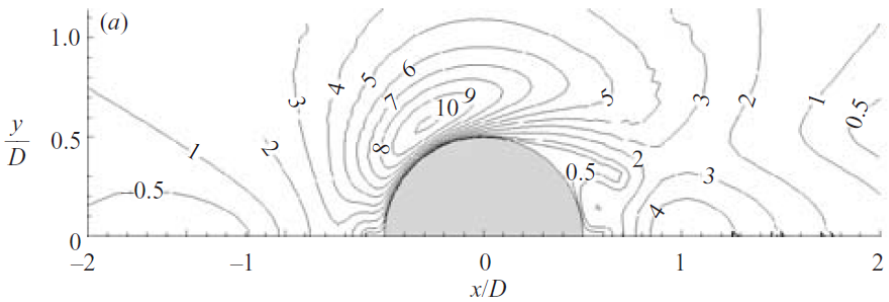

FIGURE 5.44: Bed shear stress distribution at Re = 200 (Roulund et al., 2005). Numerical results with delta/D = 8 and a smooth, rigid bed. Shear stress is expressed by the amplification factor

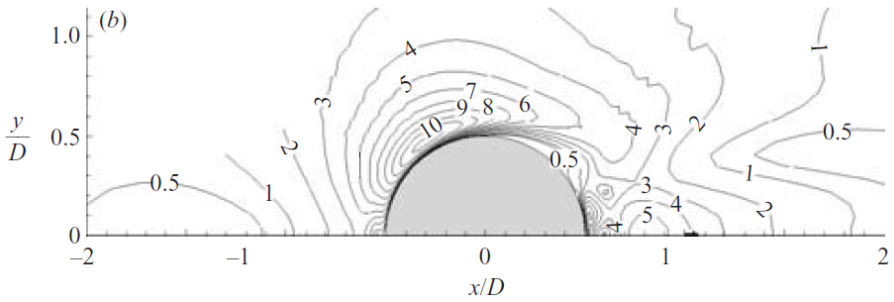

FIGURE 5.45: Bed shear stress distribution at Re = 2000 (Roulund et al., 2005). Numerical results with delta/D = 8 and a smooth, rigid bed. Shear stress is expressed by the amplification factor

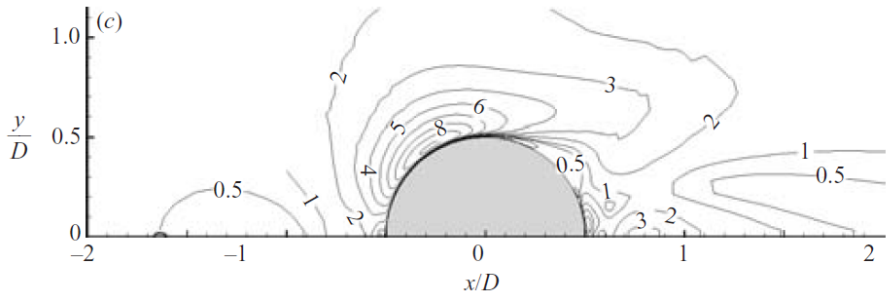

FIGURE 5.46: Bed shear stress distribution at Re = 20000 (Roulund et al., 2005). Numerical results with delta/D = 8 and a smooth, rigid bed. Shear stress is expressed by the amplification factor

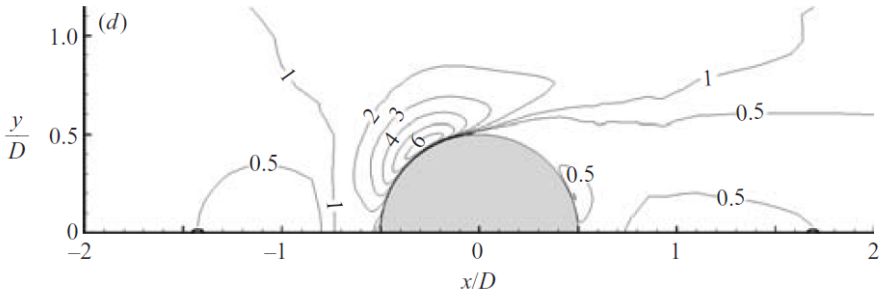

FIGURE 5.47: Bed shear stress distribution at Re = 200000 (Roulund et al., 2005). Numerical results with delta/D = 8 and a smooth, rigid bed. Shear stress is expressed by the amplification factor

The results for the monopile and hexagonal foundations from the present study are shown in Figures 5.48 and 5.49, respectively. The trend of a decreased horseshoe vortex size and maximum amplification factor from the study by Roulund et al. is continued, as expected because of the larger Reynolds number. The results are based on a time-average of the magnitude of bed shear stress. The maximum value in the monopile distribution is 4.89, which is found close to the foundation surface at $\phi = \pm 66.5$ degrees, where ϕ is measured from the negative x-axis. A large area with large amplification factors exists around this point. The maximum value in the hexagonal GBF distribution is 2.86, found at $\phi = \pm 60.1$ degrees. The higher values are concentrated in a small area near the first edge of the foundation. This finding confirmes the observation by (O'Riordan and Clare, 1990), that the areas around the corners of gravity-based foundations are most vulnerable to scour. The figures show that the shear stress amplification is low in the wake, in some areas below 1. Although these areas have large values of vorticity close to the seabed (As shown in Section 5.2.2), the vorticity contributes little to bed shear stress because the velocities are small.

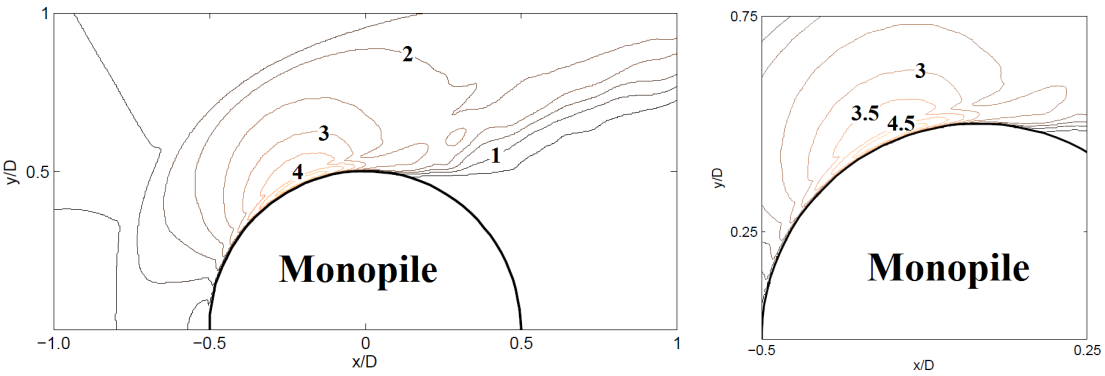

FIGURE 5.48: Bed shear stress amplification, monopile, present study. Results are time-averaged.

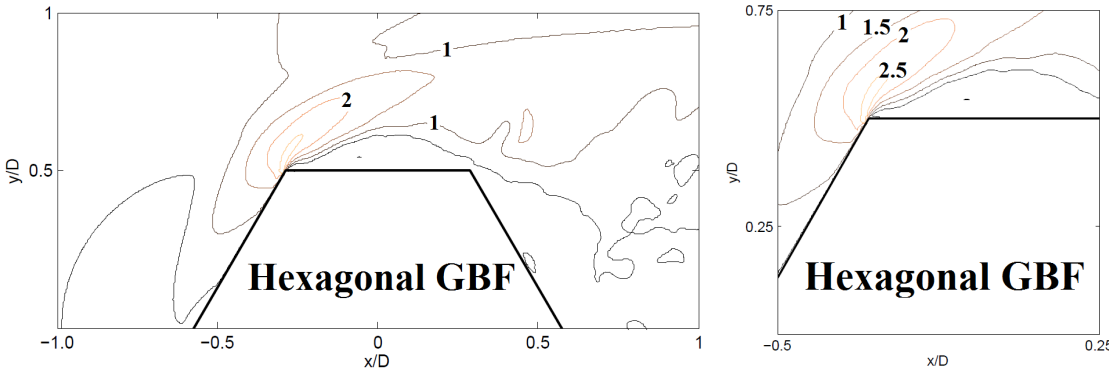

FIGURE 5.49: Bed shear stress amplification, hexagonal GBF, present study. Results are time-averaged.

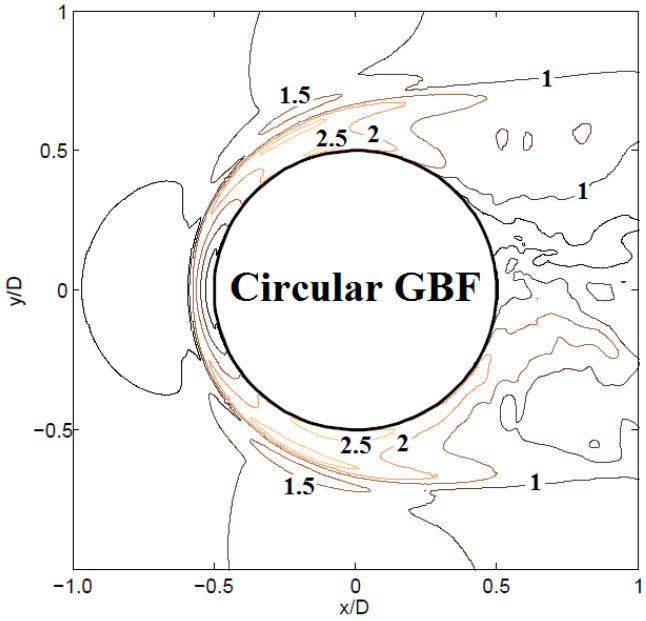

FIGURE 5.50: Bed shear stress amplification, circular GBF, present study. Results are time-averaged.

The bed shear stress distribution for the circular GBF was found to be slightly asymmetric. It should be symmetric, but the asymmetry is not severe. This is seen in Figure 5.50 which shows the full distribution (top and bottom) around the foundation. The maximum value at the upper side is 2.59 at $\phi = 68.9$ degrees, and at the lower side 2.72 at $\phi = -85.4$ degrees. These values are lower than the peak value for the hexagonal foundation, but large areas with values close to the peak values are found around the front side of the foundation.

Figure 5.51 shows the shear stress distribution (magnitude of shear stress as shear stress coefficient) on the seabed and on the foundation surfaces for each of the foundations. The axes are scaled so that everything equal to or larger than 0.01 is shown in red. It is seen that large

areas of high shear stresses exist on the foundations. The gravity-based foundations take up large shear stress values where the top of the bottom slab and the cylindrical shaft intersect. The hexagonal GBF also take up high stresses on the first edge on the side of the bottom slab (marked by arrow).

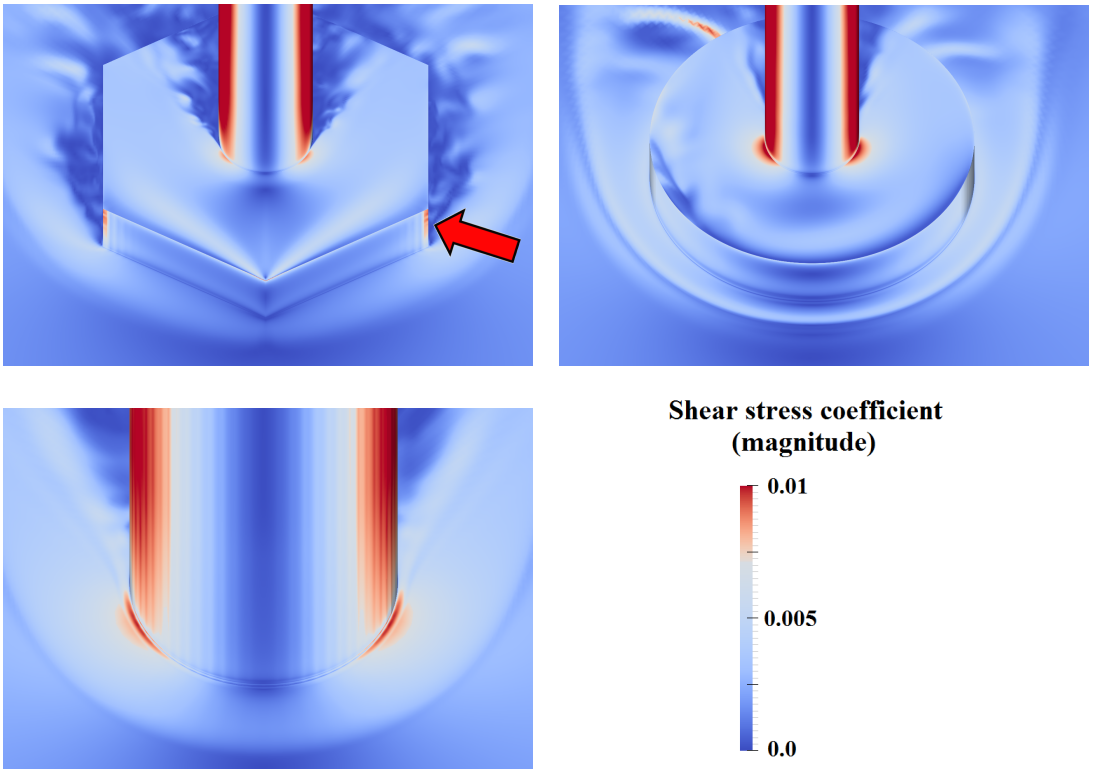

FIGURE 5.51: Shear stress distributions on the seabed and the foundation surfaces, present study

Chapter 6

Conclusion

The boundary layer flow around three different bottom-fixed wind turbine foundation designs has been investigated numerically. Two of the foundations are gravity-based, one with a hexagonal and one with a circular bottom slab, and the last is a monopile foundation. Three-dimensional analyses have been performed with Spalart-Allmaras Delayed Detached Eddy Simulation at $Re = 4 \times 10^6$, $\delta/D = 1$ and a very small roughness $z_w/D = 10^{-6}$ on the seabed and foundations.

Computational meshes with three different number of elements were used for each of the foundations in order to study of the dependence of the results on the mesh resolution. Results for velocities, pressure and bed shear stress were time averaged over a period of 50 D/U_∞. Comparisons with published data by (Dargahi, 1989) and (Roulund et al., 2005) were performed. The results were found to be reasonably accurate.

The vortical structures of the flow were explored with the Q-criterion (Jeong and Hussain, 1995). The results show a distinct horseshoe vortex in front of the monopile foundation, in accordance with (Sumer and Fredsøe, 2002). Vortex shedding is present on the lee-wake side of all the foundation designs. Two smaller horseshoe vorticies are found in front of the hexagonal gravity-based foundation, were one is on top of the bottom slab and one near the seabed in front of the bottom slab. Three horseshoe vortices are found in front of the circular gravity-based foundation. One is on top of the bottom slab and two near the seabed in front of the bottom slab, where the innermost is the larger. A physical explanation has not been found for the latter.

The downflow and backflow in front of the foundations was studied. A large area of downflow exists in front of the monopile, reaching all the way down to the seabed. This causes a backflow

in front of the foundation near the seabed due to conservation of mass. The maximum downflow and backflow values in front of the monopile foundation in the xz plane at $y/D = 0$ were found to be 30 % and 42 % of the free stream velocity, respectively. The bottom slabs of the gravity-based foundations are found to limit the downflow near the seabed.

Pressure distributions around the foundations were studied as three-dimensional isosurfaces and isolines in the xz plane at $y/D = 0$. A positive vertical pressure gradient, $dp/dz > 0$, was present in front of the monopile foundation. It was also present in front of the cylindrical shaft and the vertical part of the bottom slab on the gravity-based foundations. A larger volume of increased pressure exists in front of the monopile foundation than in front of the gravity-based foundations.

The x-component of bed shear stress along the line $y/D = 0$, $z/D = 0$ was investigated. Results were expressed as an amplification factor, i.e. normalized by the bed shear stress far away from the foundation. The horseshoe vortex size, measured as the distance from the separation point to the foundation surface along $y/D = 0$, $z/D = 0$, was found to be 0.40D for the monopile foundation, 0.125D for the hexagonal GBF and 0.22D for the circular GBF. The horseshoe vortex strength, taken as the minimum value of the amplification factor along the same line was found to be reduced (in absolute value) from -0.84 to -0.45 for the hexagonal GBF in comparison with the monopile foundation. The results for the circular GBF was -1.59, but this value is highly local.

Bed shear stress distributions near the foundations were obtained. The magnitude of the bed shear stress, normalized by the far field bed shear stress, was used. A maximum value of 4.89 was found near the surface of the monopile foundation at $\phi = \pm 66.5$ degrees, where ϕ is the angle measured from the negative x-axis. Similarly, 2.86 at $\phi = \pm 60.1$ was found for the hexagonal GBF. The larger values of bed shear stress were consentrated around the front corner of the hexagonal GBF, in accordance with findings by (O'Riordan and Clare, 1990) that show that areas around corners are most vulnerable to scour. The shear stress distribution for the circular GBF was found to be slightly asymmetric. It should be symmetric, but the asymmetry is not severe. A maximum value 2.59 at $\phi = 68.9$ degrees in the upper distribution (for positive ϕ) and 2.72 at $\phi = -85.4$ degrees on the lower distribution (for negative ϕ) was found. Although the circular GBF has a lower maximum values than the hexagonal GBF, it has large areas with an amplification factor larger than 1 in the viscinity of the structure. On a very general note, it can be said based on these observations that the gravity-based foundation with a hexagonal bottom slab is the best design with respect to scour.

6.1 Further work

Flows around bottom-fixed structures at $Re > 10^6$ are generally under-researched. Many possibilities exist for further work.

The present work could be built on in several ways. A physical explanation has not been found for the breaking up of the horseshoe vortex into two parts near the seabed in front of the circular gravity-based foundation (three parts with the vortex on top of the bottom slab). This effect could be confirmed or shown to be non-physical by using a finer computational mesh, different turbulence model or similar measures. The time averaged shear stress distribution around this foundation should be symmetric, and the asymmetric result in the present study is another reason for further investigation. A hybrid between a structured and an unstructured computational mesh might be favourable to a stricty structured mesh as the mesh density can be concentrated at specific parts of the domain more easily. This is not used in the present study as it is not easily implemented in OpenFOAM.

Shear stress distributions on a flat seabed around bottom-fixed structures are insightful, but not sufficient to predict the scour process. The author would like to see a numerical study of flow around gravity-based foundations coupled with a morphologic model for sediment transport. This has so far only been performed on monopiles.

Bibliography

Bakker, A. (2006), *Lecture 10 - Turbulence Models, Applied Computational Fluid Dynamics*, accessed 10 June 2015, http://www.bakker.org/dartmouth06/engs150/10-rans.pdf

Cengel, Y. A. and Cimbala, J. M. (2010). *Fluid Mechanics, Fundamentals and Applications, Second Edition*, McGraw-Hill.

Dargahi, B. (1989), 'The turbulent flow field around a circular cylinder', *Experiments in Fluids*, 8:1–12.

DHI Group (2012), *Predicting scour in offshore wind turbines - now a breeze*, accessed 10 June 2015, http://worldwide.dhigroup.com/

European Commission (2015), *2030 framework for climate and energy policies*, accessed 10 June 2015, `http://ec.europa.eu/clima/policies/2030/index_en.htm`

European Wind Energy Association (2015a), *The European offshore wind industry - key trends and statistics 2014*, accessed 10 June 2015, http://www.ewea.org/fileadmin/files/library/publications/statistics/EWEA-European-Offshore-Statistics-2014.pdf

European Wind Energy Association (2015b), *Wind in power - 2014 European statistics*, accessed 10 June 2015, http://www.ewea.org/fileadmin/files/library/publications/statistics/EWEA-Annual-Statistics-2014.pdf

Fraunhofer Institut for Solar Energy Systems ISE (2013), *Levelized cost of electricity, renewable energy technologies*, accessed 10 June 2015, http://www.ise.fraunhofer.de/en/publications/veroeffentlichungen-pdf-dateien-en/studien-und-konzeptpapiere/study-levelized-cost-of-electricity-renewable-energies.pdf

Gainer, T. G., Morrison, J. H., Rivers, S. M., Mysko, S. J., and Witkowski, D. P. (2001), 'Cfd sensitivity analysis of a modern civil transport near buffet-onset conditions', http://ntrs.nasa.gov/archive/nasa/casi.ntrs.nasa.gov/20020015798.pdf

Global Wind Energy Council (2015), *Global Wind Energy Council homepage*, accessed 10 June 2015, http://www.gwec.net/global-figures/graphs/

Jeong, J. and Hussain, F. (1995), 'On the identification of a vortex', *Journal of fluid mechanics*, 285:69–94.

Jeppsson, J., Larsen, P. E., and Larsson, . (2008), 'Technical description lillgrund wind power plant', *Lillgrund Pilot Project. Vattenfall Vindkraft AB.*

Kalitzin, G., Medic, G., Iaccarino, G., and Durbin, P. (2005), 'Near-wall behaviour of rans turbulence models and implications for wall functions', *Journal of Computational Physics*, 204:265–291.

Karimirad, M. (2014), *Offshore Energy Structures*, Springer.

Lorc, Knowledge (2011), *Lorc-webpage*, accessed 10 June 2015, http://www.lorc.dk/offshore-wind-farms-map/list

Ong, M. C., Utnes, T., Holmedal, L. E., Myrhaug, D., and B., P. (2010), 'Numerical simulation of flow around a circular cylinder close to a flat seabed at high reynolds numbers using a k-ϵ model', *Coastal Engineering*, 57:931–947.

Ong, M. C., Utnes, T., Holmedal, L. E., Myrhaug, D., and Pettersen, B. (2009), 'Numerical simulation of flow around a smooth circular cylinder at very high reynolds numbers', *Marine Structures*, 22:142–153.

OpenFOAM Foundation (2015), *OpenFOAM webpage*, accessed 10 June 2015, http://www.openfoam.org/

OpenFOAM Ltd (2015), *OpenFOAM User Guide*, accessed 10 June 2015, http://cfd.direct/openfoam/user-guide/

O'Riordan, N. J. and Clare, D. G. (1990). 'Geotechnical considerations for the installation of gravity base structures, paper otc 6381', In *22nd Offshore Technology Conference, May 7-10, Houston*, pages 309–316.

Pope, S. B. (2000), *Turbulent Flows*, Cambridge University Press.

Roulund, A., Sumer, B. M., Fredsøe, J., and Michelsen, J. (2005), 'Numerical and experimental investigation of flow and scour around a circular pile', *Journal of Fluid Mechanics*, 534:351–401.

Shirole, A. M. and Holt, R. C. (1991), 'Planning for comprehensive bridge safety assurance program', *Transportation Research Record*, 1290.

Spalart, P. R. and Allmaras, S. R. (1992), 'A one-equation turbulence model for aerodynamic flows', In *30th Aerospace Sciences Meeting and Exhibit, January 6-9, Reno, NV, USA.*

Spalart, P. R., Deck, S., Shur, M. L., Squires, K. D., Strelets, M. K., and Travin, A. (2006), 'A new version of detached-eddy simulation, resistant to ambiguous grid densities', *Theoretical and computational fluid dynamics*, 20(3):181–195.

Sumer, B. M. and Fredsøe, J. (1997), *Hydrodynamics Around Cylindrical Structures*, World Scientific.

Sumer, B. M. and Fredsøe, J. (2002), *The Mechanics of Scour in the Marine Environment*, World Scientific.

Appendix A

OpenFOAM case files

A.1 0-folder

U

```
/*---------------------------------*- C++ -*----------------------------------*\
| =========                 |                                                 |
| \\      /  F ield         | OpenFOAM: The Open Source CFD Toolbox           |
|  \\    /   O peration     | Version:  2.2.0                                 |
|   \\  /    A nd           | Web:      www.OpenFOAM.org                      |
|    \\/     M anipulation  |                                                 |
\*---------------------------------------------------------------------------*/
FoamFile
{
version     2.0;
format      ascii;
class       volVectorField;
location    "0";
object      U;
}
// * * * * * * * * * * * * * * * * * * * * * * * * * * * * * * * * * * * * * //

dimensions      [ 0 1 -1 0 0 0 0 ];

internalField   uniform ( 4 0 0 );

boundaryField
```

```
{
INLET
{
type            groovyBC;
variables       "Uinf=4;dlta=1;z0=0.000001;K=0.41;uf=(K*Uinf)/log(dlta/z0);
val=(uf/K)*log(z/z0)*vector(1,0,0);uz=((mag(val))<Uinf)?(mag(val)):Uinf;";
valueExpression "vector(uz, 0, 0)";
value           uniform (4 0 0);
}
OUTLET
{
type            zeroGradient;
}
FOUNDATION
{
type            fixedValue;
value           uniform ( 0 0 0 );
}
UPPERSIDE
{
type            zeroGradient;
}
LOWERSIDE
{
type           zeroGradient;
}
WATERSURFACE
{
type            zeroGradient;
}
BOTTOM
{
type            fixedValue;
value           uniform ( 0 0 0 );
}
}


// ************************************************************************* //
```

p

```
/*---------------------------------*- C++ -*----------------------------------*\
| =========                 |                                                 |
| \\      /  F ield         | OpenFOAM: The Open Source CFD Toolbox           |
|  \\    /   O peration     | Version:  2.2.0                                 |
|   \\  /    A nd           | Web:      www.OpenFOAM.org                      |
|    \\/     M anipulation  |                                                 |
\*---------------------------------------------------------------------------*/
FoamFile
{
version     2.0;
format      ascii;
class       volScalarField;
location    "0";
object      p;
}
// * * * * * * * * * * * * * * * * * * * * * * * * * * * * * * * * * * * * * //

dimensions      [ 0 2 -2 0 0 0 0 ];

internalField   uniform 0;

boundaryField
{
INLET
{
type            zeroGradient;
}
OUTLET
{
type            fixedValue;
value           uniform 0;
}
UPPERSIDE
{
type            zeroGradient;
}
LOWERSIDE
{
type            zeroGradient;
}
```

```
FOUNDATION
{
type            zeroGradient;
}
WATERSURFACE
{
type            zeroGradient;
}
BOTTOM
{
type            zeroGradient;
}
}


// ************************************************************************* //
```

nuSgs

```
/*---------------------------------*- C++ -*----------------------------------*\
| =========                 |                                                 |
| \\      /  F ield         | OpenFOAM: The Open Source CFD Toolbox           |
|  \\    /   O peration     | Version:  2.2.0                                 |
|   \\  /    A nd           | Web:      www.OpenFOAM.org                      |
|    \\/     M anipulation  |                                                 |
\*---------------------------------------------------------------------------*/
FoamFile
{
version     2.0;
format      ascii;
class       volScalarField;
object      nuSgs;
}
// * * * * * * * * * * * * * * * * * * * * * * * * * * * * * * * * * * * * * //

dimensions      [0 2 -1 0 0 0 0];

internalField   uniform 0.0544766;

boundaryField
```

```
{
INLET
{
type            groovyBC;
variables       "Uinf=4;dlta=1;Cmu=0.09;K=0.41;z0=0.000001;uf=(K*Uinf)/log(dlta/z0);
k1=pow(Cmu,-0.5)*(1-(z/dlta))*(mag(1-(z/dlta)))*pow(uf,2);k2=0.0001*pow(Uinf,2);
k=(k1>k2)?k1:k2;l1=(K*z)/(1+3.5*(z/dlta));l2=Cmu*dlta;l=(l1<l2)?l1:l2;
epsilon=(1/l)*pow(Cmu,0.75)*pow(k,1.5);ntilda=(Cmu/epsilon)*pow(k,2);";
valueExpression "ntilda";
value           uniform 0;
}

OUTLET
{
type            zeroGradient;
}

LOWERSIDE
{
type           zeroGradient;
}

UPPERSIDE
{
type           zeroGradient;
}

BOTTOM
{
type            nutUSpaldingWallFunction;
value           uniform 0.0000123;                        // Near-wall
}

WATERSURFACE
{
type           zeroGradient;
}

FOUNDATION
{
type            nutUSpaldingWallFunction;
```

```
value           uniform 0.0000123;                      // Near-wall
}
}

// ************************************************************************* //
```

nuTilda

```
/*--------------------------------*- C++ -*----------------------------------*\
| =========                 |                                                 |
| \\      /  F ield         | OpenFOAM: The Open Source CFD Toolbox           |
|  \\    /   O peration     | Version:  2.2.0                                 |
|   \\  /    A nd           | Web:      www.OpenFOAM.org                      |
|    \\/     M anipulation  |                                                 |
\*---------------------------------------------------------------------------*/
FoamFile
{
version     2.0;
format      ascii;
class       volScalarField;
location    "0";
object      nuTilda;
}
// * * * * * * * * * * * * * * * * * * * * * * * * * * * * * * * * * * * * * //

dimensions      [ 0 2 -1 0 0 0 0 ];

internalField   uniform 0.0016;

boundaryField
{
INLET
{
type            groovyBC;
variables       "Uinf=4;dlta=1;Cmu=0.09;K=0.41;z0=0.000001;uf=(K*Uinf)/log(dlta/z0);
k1=pow(Cmu,-0.5)*(1-(z/dlta))*(mag(1-(z/dlta)))*pow(uf,2);k2=0.0001*pow(Uinf,2);
k=(k1>k2)?k1:k2;l1=(K*z)/(1+3.5*(z/dlta));l2=Cmu*dlta;l=(l1<l2)?l1:l2;
epsilon=(1/l)*pow(Cmu,0.75)*pow(k,1.5);ntilda=(Cmu/epsilon)*pow(k,2);";
valueExpression "ntilda";
value           uniform 0;
```

```
}
OUTLET
{
type            zeroGradient;
}
FOUNDATION
{
type            fixedValue;
value           uniform 0;
}
UPPERSIDE
{
type            zeroGradient;
}
LOWERSIDE
{
type            zeroGradient;
}
WATERSURFACE
{
type            zeroGradient;
}
BOTTOM
{
type            fixedValue;
value           uniform 0;
}
}


// ************************************************************************* //
```

nut

```
/*---------------------------------*- C++ -*----------------------------------*\
| =========                 |                                                 |
| \\      /  F ield         | OpenFOAM: The Open Source CFD Toolbox           |
|  \\    /   O peration     | Version:  2.2.0                                 |
|   \\  /    A nd           | Web:      www.OpenFOAM.org                      |
|    \\/     M anipulation  |                                                 |
```

```
\*---------------------------------------------------------------------------*/
FoamFile
{
version     2.0;
format      ascii;
class       volScalarField;
location    "0";
object      nut;
}
// * * * * * * * * * * * * * * * * * * * * * * * * * * * * * * * * * * * * * //

dimensions      [ 0 2 -1 0 0 0 0 ];

internalField   uniform 0;

boundaryField
{
WATERSURFACE
{
type            zeroGradient;
}

BOTTOM
{
type            nutkRoughWallFunction;
Ks              uniform 3E-5;
Cs              uniform 1;
value           uniform 0.0000123; //Near-wall
}

INLET
{
type            groovyBC;
variables       "Uinf=4;dlta=1;Cmu=0.09;K=0.41;z0=0.000001;uf=(K*Uinf)/log(dlta/z0);
k1=pow(Cmu,-0.5)*pow((1-(z/dlta)),2)*pow(uf,2);k2=0.0001*pow(Uinf,2);
k=(k1>k2)?k1:k2;l1=(K*z)/(1+3.5*(z/dlta));l2=Cmu*dlta;l=(l1<l2)?l1:l2;
epsilon=(1/l)*pow(Cmu,0.75)*pow(k,1.5);nt=(Cmu/epsilon)*pow(k,2);";
valueExpression "nt";
value           uniform 0;
}
OUTLET
```

```
{
type            zeroGradient;
}

LOWERSIDE
{
type            zeroGradient;
}

UPPERSIDE
{
type            zeroGradient;
}

FOUNDATION
{
type            nutkRoughWallFunction;
Ks              uniform 3E-5;
Cs              uniform 1;
value           uniform 0.0000123; //Near-wall
}
}


// ************************************************************************* //
```

A.2 system-folder

Kommenter: nut brukes kun til å sette ruhet

fvSchemes

```
/*---------------------------------*- C++ -*----------------------------------*\
| =========                 |                                                 |
| \\      /  F ield         | OpenFOAM: The Open Source CFD Toolbox           |
|  \\    /   O peration     | Version:  2.2.0                                 |
|   \\  /    A nd           | Web:      www.OpenFOAM.org                      |
|    \\/     M anipulation  |                                                 |
```

```
\*---------------------------------------------------------------------------*/
FoamFile
{
version     2.0;
format      ascii;
class       dictionary;
object      fvSchemes;
}
// * * * * * * * * * * * * * * * * * * * * * * * * * * * * * * * * * * * * * //

ddtSchemes
{
default backward;
}

d2dt2Schemes
{
}

gradSchemes
{
default         Gauss linear;

grad(nuTilda)   cellLimited Gauss linear 1;
grad(U)         cellLimited Gauss linear 1;
}

divSchemes
{
default         none;

div(phi,U)      Gauss LUST unlimitedGrad(U);
//div(phi,U)      Gauss linearUpwind unlimitedGrad(U);
div(phi,k)      Gauss limitedLinear 1;
div(phi,nuTilda) Gauss limitedLinear 1;

div((nuEff*dev(T(grad(U))))) Gauss linear;
}

laplacianSchemes
{
```

```
default         Gauss linear limited corrected 0.33;
}

interpolationSchemes
{
default         linear;
}

snGradSchemes
{
default         limited corrected 0.33;
}

fluxRequired
{
default         no;
p;
}

// ************************************************************************* //
```

fvSolution

```
/*---------------------------------*- C++ -*----------------------------------*\
| =========                 |                                                 |
| \\      /  F ield         | OpenFOAM: The Open Source CFD Toolbox           |
|  \\    /   O peration     | Version:  2.2.0                                 |
|   \\  /    A nd           | Web:      www.OpenFOAM.org                      |
|    \\/     M anipulation  |                                                 |
\*---------------------------------------------------------------------------*/
FoamFile
{
version     2.0;
format      ascii;
class       dictionary;
object      fvSolution;
}
// * * * * * * * * * * * * * * * * * * * * * * * * * * * * * * * * * * * * * //

solvers
```

```
{
p
{
solver           GAMG;
tolerance        1e-6;
relTol           0.1;

smoother         GaussSeidel;
nPreSweeps       0;
nPostSweeps      2;

cacheAgglomeration true;

nCellsInCoarsestLevel 50;//10;
agglomerator     faceAreaPair;
mergeLevels      1;
};

pFinal
{
solver           GAMG;
tolerance        1e-6;
relTol           0;

smoother         GaussSeidel;
nPreSweeps       0;
nPostSweeps      2;

cacheAgglomeration true;

nCellsInCoarsestLevel 50;//10;
agglomerator     faceAreaPair;
mergeLevels      1;
};

U
{
solver           PBiCG;
preconditioner   DILU;
tolerance        1e-08;
relTol           0;
```

```
};

UFinal
{
solver           PBiCG;
preconditioner   DILU;
tolerance        1e-08;
relTol           0;
};

k
{
solver           PBiCG;
preconditioner   DILU;
tolerance        1e-07;
relTol           0;
};

B
{
solver           PBiCG;
preconditioner   DILU;
tolerance        1e-07;
relTol           0;
};

nuTilda
{
solver           PBiCG;
preconditioner   DILU;
tolerance        1e-07;
relTol           0;
};
}

PISO
{
nCorrectors     2;
nNonOrthogonalCorrectors 1;
}
```

```
PIMPLE
{
nCorrectors     2;
nNonOrthogonalCorrectors 1;
}

relaxationFactors
{
"U.*"               1;
"nuTilda.*"         1;
}


// ************************************************************************ //
```

Appendix B

MATLAB Codes

Fourier analysis

```
% The script uses vectors t (time) and Cl (Cross flow force coefficient)
D = 1;    % Characteristic size of the foundations, diameter of the monopile
U = 4;    % Inflow velocity

t_int = transpose(t);
Fs = 1/(t_int(2)-t_int(1));
y_intLift = interp1(t,Cl,t_int,'spline');
L=length(t_int);
y_intLift2=y_intLift-mean(y_intLift);
NFFT = 2^nextpow2(L); % Next power of 2 from length of y
Ylift = fft(y_intLift2,NFFT)/L;
flift = Fs/2*linspace(0,1,NFFT/2+1);

freq=flift;
ampLift=Ylift;
pxx = 2*abs(ampLift(1,1:NFFT/2+1));
St = freq*D/U;

St = transpose(St);    % Strouhal number
pxx = transpose(pxx);
pxx = pxx/max(pxx);    % Normalized spectrum

figure
plot(St,pxx)
```